UNIVERSITY OF MANCHESTER

Broadband Printed Graphene Metamaterial Absorbers

A thesis submitted to The University of Manchester for the degree of Doctor of Philosophy in the Faculty of Science and Engineering

Yixian Fang

2021

School of Electrical and Electronic Engineering

Table of Contents

Word Count: 39540

Figure List

Table List

Abstract

The rapid development of wireless communication, space-based radar systems and active military radars in the past decades gives rise to the necessary of information security and electromagnetic waves pollution, which arouse the requirement of perfect electromagnetic absorbers in both military and civil areas. Since the isolation of graphene and the first experimental demonstration of so-called perfect metamaterial absorber carried out in the early 21st century, a large amount of research has been directed at graphene based metamaterial absorbers. This thesis delivers pioneering developments on the design of printed graphene metamaterial absorbers on electromagnetic ranges including radio frequency, microwave frequency, and THz bands.

This thesis focuses on the design and optimization of broadband metamaterial absorbers for civil and military applications and aims to provide novel ideas and combed design approaches for further development of the metamaterial absorbers with outstanding properties

This thesis presents several broadband printed graphene metamaterial absorbers with competitive properties. For example, the two multilayer structure metamaterial absorbers in chapter 3 provide ultra-wide operation bandwidth covering from C band to Ka band, and from S band to Ku band, respectively; the ultra-thin metamaterial absorber in chapter 4 achieves a relative absorption bandwidth of 178% with a thickness of merely 0.3 mm; the novel printed graphene AMC based radar absorber has pioneering advances compared with conventional metallic AMC based absorbers; the genetic algorithm optimized absorber indicates potentials of coding metamaterial absorbers. For the first time, the printed graphene AMC based radar absorber is experimentally demonstrated. Furthermore, the printed graphene metamaterial absorbers presented in this thesis are angle-insensitive and polarization-independent, and possess good flexibility thanks to the printed graphene patterns and flexible dielectric substrates.

This work significantly provides novel approaches and more design flexibility to metamaterial absorbers, and expands the applications of printed graphene in the design and fabrication of metamaterial absorbers.

Declaration

No portion of the work referred to in the dissertation has been submitted in support of an application for another degree or qualification of this or any other university or other institute of learning.

Copyright Statement

Acknowledgement

All of this work in the thesis would not be possible without the guidance and help from my supervisor Professor Zhirun Hu, who offers me the opportunity to start my PhD study and guides me with so much patience and tolerance.

Next, I would like to thank Dr. Xianjun Huang, who firstly led me to the field of metamaterial absorbers and helped me with simulations at the very start of my PhD course.

I'm also grateful to Professor Habiba H. Ouslimani and Professor Kostya S. Novoselov for their constructive comments for my paper.

At last I would like to thank my dear family, friends and my lovely roommates, who back me up all the time. I can never come this far without you. Thank you for your support and company.

List of Abbreviations

2D	Two dimensional
3D	Three dimensional
5G	Fifth generation
AFM	Atomic force microscopy
AMC	Artificial magnetic conductor
COM	Component object model
CVD	Chemical vapor deposition
DC	Direct current
DNA	Deoxyribonucleic acid
EM	Electromagnetic
FSS	Frequency selective surface
GHz	Gigahertz
ITO	Indium Tin Oxide
ISM	Industrial, scientific and medical
MW	Microwave
MWS	Microwave studio
NEMS	Nanoelectromechanical systems
NMP	N-Methyl-2-pyrrolidone
OLE	Object linking and embedding
PCMs	Phase change materials
PEC	Perfect electric conductor
PMMA	Polymethylmethacrylate
RCS	Radar cross section
RLC	Resistor inductor capacitor
RF	Radio frequency
SEM	Scanning electron microscope

TE	Transverse electric
THz	Terahertz
TM	Transverse magnetic
VBA	Visual basic for applications
VO_2	Vanadium di Oxide
WAIM	Wide-angle impedance matching

List of Symbols

A	Reflection magnitude
$A(\omega)$	Absorption
B	Effective susceptance
C	Capacitance
C_f	Finite-size correction factor
G_0	Wave conductance of free space
I	Electric current
L	Inductance
P	Reflection phase
R	Resistance
R_s	Sheet resistance
$R(\omega)$	Reflection
$T(\omega)$	Transmission
V	Electric voltage
Z	Impedance
Z_0	Free space impedance
Z_{in}	Input impedance
Γ	Reflection coefficient
e	Electron charge
f	Frequency
k	Wavenumber
k_B	Boltzmann's constant
k_c	Dielectric constant
n	Refractive index
v_F	Fermi velocity
β	Phase constant

ε	Electric permittivity
ζ	Energy
θ	Incident angle
λ	Wavelength
μ	Magnetic permeability
μ_c	Chemical potential
ρ	Bulk resistivity
σ	Conductivity
τ	Carrier relaxation time
ω	Angular frequency
$\hbar$	Reduced Planck's constant

Chapter 1: Introduction

1.1 Background

The electromagnetic (EM) absorber refers to structures that can absorb an incident EM wave. The study of electromagnetic absorbers can be traced back to the study of wave absorbers for the 2-GHz band carried out in the mid of 1930s at the Naamlooze Vennootschap Machinerieen in the Netherlands [1]. The research on radar absorbers for military use was aroused during World War II and was carried out mainly by the German Schornsteinfeger Project [2] and the MIT Radiation Laboratory in the United States [3]. After the war, various types of EM-wave absorbers were proposed in the following several decades, mostly were composed of carbon-based materials and were developed for anechoic chamber applications [4].

With the development of the cross-disciplinary field of metamaterials in the late 20th century, many applications of metamaterials were proposed and experimentally demonstrated. Among various metamaterial applications, metamaterial absorber is a major breakthrough for electromagnetic research. The word “metamaterial” comes from the Greek word μετά *meta*, meaning "beyond" and the Latin word *materia*, meaning "matter" or "material". As the literal meaning, metamaterial is any material engineered to have a property that is not found in naturally occurring materials [5]. Metamaterials derive their properties not from the properties of the base materials, but from their newly designed structures. Electromagnetic metamaterials are arrays of structured subwavelength elements which may be described as effective materials via the electric permittivity and magnetic permeability [6]. Their newly designed structures, such as shape, size, and arrangement, give them outstanding properties capable of manipulating electromagnetic waves by enhancing, blocking, or absorbing [6]. The design flexibility of metamaterials makes them excellent candidates for electromagnetic wave absorbers.

Metamaterials were first introduced to the design of absorbers in 2002 [7]. The first experimentally demonstrated metamaterial absorber was proposed in 2008 [8]. After the first experimental demonstration, different kinds of metamaterial absorbers were carried out in recent

years. In general, the ideal metamaterial absorber is supposed to absorb all incident electromagnetic waves without causing any reflection waves, regardless of the incident wave direction, polarization, and frequency [9]. However, this kind of ideal wave absorber does not exist in the real world. Therefore, the performance of metamaterial absorber characteristics is defined by the effective absorption with over 90% absorptivity, corresponding to the reflection coefficient of −10 dB or less. There are different types of metamaterial absorbers distinguished by their operation frequency bands. The narrow band absorbers provide effective absorption at a specific frequency point with a narrow bandwidth. Multi-band absorbers operate at several separated frequency points with narrow or wide bandwidths. The broadband absorbers have broadband effective absorption bandwidths covering wide frequency bands. In this thesis, the design and fabrication approaches are focused on the broadband metamaterial absorbers. Desired properties required for a good broadband metamaterial absorber are angle-insensitive and polarization-independent property, small unit cell and thickness, mechanical flexibility, and of course the broad effective absorption bandwidth.

Due to the rapid growing research on printed conductive inks for electronic applications, various types of conductive inks, such as copper nanoparticle inks, carbon black and carbon nanotubes, and silver nanoparticle inks, have been used to design and fabricate metamaterial absorbers. The study of graphene ink has attracted a large amount of interest since the isolation of graphene in 2004 [10]. Comparing with other conductive inks, the high conductivity, stable thermal and chemical properties, and flexibility make graphene ink a standout candidate for metamaterial absorbers. Besides, the tunability of carrier density under a modulating electrical field makes graphene appropriate for designing switchable and tunable metamaterial absorbers. The tunable property of graphene can be realized by simply applying external electric field, such as an external DC voltage. With these unique properties, graphene is chosen to be utilized to design and fabricate the metamaterial absorbers introduced in this thesis.

Genetic algorithms were first proposed in 1950 by Alan Turing [11], while the technique was first carried out in practice by Nils Aall Barricelli four years later [12]. Genetic algorithm is

inspired by the biological concept of evolution which explains the biological development of species with mating selection and survival of the fittest. The genetic algorithms are stochastic search algorithms which are often used in machine learning applications. As a type of algorithm which is utilized to solve optimization problems and find optimal solutions, genetic algorithm can be applied in many fields, such as math, natural science, and engineering. Thus, it is no surprise that genetic algorithm can be introduced to the design of metamaterial absorbers. However, there are a few drawbacks to this technique. For example, the program might take a lot of time to evolve and find optimal solutions due to the repetitive nature of the algorithm. Besides, it might miss the less optimal designs which have the possibility to provide greater global optimum because the algorithm cannot backtrack. Additionally, the mutation process could make the designs mutate in bad direction, inducing worthless designs to the population, which lead to a prohibitively long time required for the convergence. Therefore, when use the genetic algorithm to code metamaterial absorbers, special attentions should be paid to the fitness function and the diversity in the population in order to avoid these drawbacks.

1.2 Motivation and Key Contributions

In the past decade, the achievement of wireless technology has induced the growing use of radiofrequencies (RFs) and microwaves (MWs) emitted by the radio stations and wireless home devices [13]. Electromagnetic fields produce non-ionizing radiation, which gives rise to the so-called electromagnetic waves pollution. Electronic devices such as microwave ovens, radio, smartphones, and Bluetooth earphones emit low intensity electromagnetic radiation at frequencies from 300 MHz to 300 GHz in our everyday life [14]. It is possible that these devices can work near to natural biological frequencies, interfering with sophisticated electric circuits that are present in the human body [15]–[17]. Some in vitro experiments showed that RF-MWs can be carcinogens and can induce DNA damage [18]–[20]. Except for the electromagnetic waves pollution, the rise of interference issues among different electronic devices is also need to be solved. For example, the global rollout of 5G cellular networks at around 3.5 GHz has already proven to cause interference with legacy satellite downlinks [21]. With the trend of the wireless

technology development and the growth of electronic applications and devices, it can be anticipated that problems like electromagnetic waves pollution and interference issues will emerge in endlessly and influence our daily life. Therefore, the requirement of broadband metamaterial absorbers with outstanding properties will also increase for reducing the electromagnetic waves pollution and solving interference issues. Broadband metamaterial absorbers are quite important for civil and military stuffs.

The first experimentally demonstrated metamaterial absorber in 2008 was a narrow band absorber with a peak absorption located at 11.48GHz [8]. To extend the operation bandwidth of metamaterial absorbers, several approaches have been developed in recent years, including lump loaded method, multilayer structures, anti-phase reflection cancellation with artificial magnetic conductor (AMC), and introduction of multiple resonances through adding more resonators with different shaped patterns on a single plane. Besides, there are several methodologies, such as equivalent medium theory, interference theory and equivalent circuit model method, which can be used to analyze the absorption mechanism of metamaterial absorbers and provide guidelines on designing metamaterial absorbers. Although various design approaches and analysis methodologies have been proposed during the development of metamaterial absorbers in the past decades, the design of metamaterial absorbers is still a very complicated subject. Unlike the antenna design field, in which there could be software tools like Antenna Magus which can accelerate the design and modelling process, there is no such kind of tools or any "recipe" which can be used for metamaterial absorber design.

Currently, the previously proposed artificial magnetic conductor (AMC) designs use metallic patterns on rigid substrates. The metallic patterns in conventional AMC structures provide nearly zero absorptivity, which means the absorption of these AMC-based absorbers can only count on the cancellation of reflections between different AMCs, hindering the operation bandwidth and wide-angle performance. Besides, the metallic patterns and rigid dielectric substrates in conventional AMC designs lead to poor mechanical flexibility. Furthermore, the phase difference

of reflections between different AMCs is mainly achieved through different types of shape or size of the AMC patterns, which limits the design flexibility.

At present, there have been several papers introducing coding metamaterial absorbers, but very few. No detailed analysis or investigations about the algorithms could be found in those papers. However, the attempt of introducing concepts, such as coding, machine learning, or algorithms into the design of metamaterial absorbers is invaluable for the further development of metamaterial absorbers.

The motivation for the study is to provide novel ideas and combed design approaches for further development of the metamaterial absorbers with outstanding properties.

The main contributions of the thesis are listed as follows:

1. The design approaches and analysis methodologies mentioned in this thesis are systematically sorted out. Several broadband metamaterial absorbers with competitive properties have been designed and investigated to demonstrate the novel ideas and approaches. On the other hand, the thesis is organized according to different design approaches. For example, Chapter 3 contains two broadband metamaterial absorbers with their operation bandwidth covering various frequency bands, and both of them are designed through multilayer structures and analyzed with equivalent circuit model method.

2. The eddy current approach introduced in Chapter 4 is a novel approach for designing metamaterial absorbers. The main sandwich-like structure in the design is composed of an ultra-thin dielectric substrate with two layers of graphene printed resistive sheets patterned on its front and back surfaces, respectively. As the thickness of the dielectric substrate becomes thin enough to be omitted, the anti-parallel surface currents in the front and back surfaces constitute current loops like eddy currents flowing in closed loops within conductors, and lead to strong magnetic resonances and energy loss in the material. With the novel approach, the traditional limitation is broken and the absorbers with smaller thickness can achieve broader absorption bandwidth.

3. The broadband printable and flexible artificial magnetic conductor (AMC) based metamaterial absorber is designed and fabricated with fully screen printed graphene AMCs. Different from conventional metallic AMC patterns, the screen printed graphene AMC patterns have exactly the same shape and size. The desired anti-phase reflection cancellation is achieved by controlling the sheet resistance of the printed graphene AMC patterns. Since the printed graphene AMCs on their own can absorb the incident electromagnetic waves partially, the printable and flexible metamaterial absorber not only redirect but also absorb the incident waves so to provide a broader operation bandwidth and better wide angle performances compared with conventional AMC based absorbers. Due to the unique property of the printed graphene AMCs, a new guideline of the required phase different range is presented for effective absorption. Comparing with the conventional guideline of required phase difference for metallic AMCs, which is around $180° \pm 37°$, the new guideline of the phase difference range is enlarged to be $180° \pm 78°$. Besides, according to the experimental measurement results of the fabricated printed graphene AMC based absorber under different bending conditions, this absorber has reasonably good mechanical flexibility and can still provide greater than 70% absorption within most parts of its operation frequency band. This is the first time the printed graphene AMCs are proposed and experimentally demonstrated, this novel approach could have a wider application as it provides more degree of freedom in metamaterial absorber designs.

4. Genetic Algorithm is introduced to the metamaterial absorber design and is used to optimize the printed graphene AMC based absorber to achieve broader effective absorption bandwidth. The Genetic Algorithm program is realized through MATLAB controlling CST Microwave Studio and is investigated in detail for further improvement of the code. Parameter settings (population size, evolution generations, and fitness function) of crucial importance in relation to the convergence of the program are analyzed. The drawbacks of the program are also discussed for further improvement. The program successfully provides a better solution (different arrangement of dual printed graphene AMC elementary unit cells)

which achieves a broader effective absorption bandwidth within limited evolution generations, indicating an invaluable potential for future development of coding metamaterial absorbers.

5. A new approach to design tunable broadband THz metamaterial absorber with single layer graphene patterns is verified through numerical simulation with CST. The introduction of multiple resonances through adding more resonators with different shaped patterns on a single plane sometimes can lead to a larger unit cell, which is not a desired property for the metamaterial absorbers. Therefore, the new approach solves this problem in reverse through introducing multiple resonances by engraving the original patterns. The conventional approach starts from a completely empty or in another word, a blank plane and put different types of patterns on it, while the novel approach in reverse starts from a plane covered entirely by monolayer graphene and add engraved gaps on that. A tunable broadband THz metamaterial absorber with two gaps on the single layer of graphene is designed through this approach and demonstrates the feasibility of this design approach.

1.3 Publication

Journal Publications:

1. **Y. Fang**, K. Pan, T. Leng, H. H. Ouslimani, K. S. Novoselov, and Z. Hu, "Controlling Graphene Sheet Resistance for Broadband Printable and Flexible Artificial Magnetic Conductor Based Microwave Radar Absorber Applications," *IEEE Trans. Antenna Propag*., pp.1, July 2021.

Conferences Publications:

1. **Y. Fang**, T. Leng, H. H. Ouslimani, and Z. Hu, "Printed Graphene Broadband and Flexible Artificial Magnetic Conductor Metasurface Microwave Radar Absorbers," *in Proc. IEEE International Conference on Antenna Measurements and Applications (CAMA),* Antibes Juan-les-Pins, France, 2021 (Special sessions).
2. **Y. Fang**, and Z. Hu, "Broadband and Wide-angle Microwave Metamaterial Absorber with Effective EM Wave Absorption in the S-, C-, X- and Ku-band," *15th European Conference on Antennas and Propagation (EuCAP)*, Düsseldorf, Germany, 2021, pp.1–4.

3. **Y. Fang**, and Z. Hu, "Ultra-wideband polarization-insensitive thin microwave absorber composed of triple-layer resistive surfaces," *14th European Conference on Antennas and Propagation (EuCAP)*, Copenhagen, Denmark, 2020, pp.1–4.
4. **Y. Fang**, Y. Jiang, K. Pan and Z. Hu, "On the design of metamaterial radar absorber applying AMC by controlling surface resistance," *IEEE International Symposium on Antennas and Propagation and USNC-URSI Radio Science Meeting*, Atlanta, GA, USA, 2019, pp. 1327–1328.
5. Y. Jiang, T. Leng, **Y. Fang**, L. Xu, K. Pan and Z. Hu, "A Novel e-textile Integrated Wideband Monopole Antenna for Body-worn Energy Harvesting Systems," *2019 IEEE MTT-S International Microwave Symposium (IMS)*, Boston, MA, USA, 2019, pp. 1057–1059.
6. Y. Jiang, T. Leng, **Y. Fang**, Z. Hu and L. Xu, "Machine Embroidered Wearable e-textile Wideband UHF RFID Tag Antenna," 2019 *IEEE International Symposium on Antennas and Propagation and USNC-URSI Radio Science Meeting*, Atlanta, GA, USA, 2019, pp. 643–644.
7. K. Pan, T. Leng, Y. Jiang, **Y. Fang**, X. Zhou et al., "Graphene Printed UWB Monopole Antenna for Wireless communication applications," *2019 IEEE International Symposium on Antennas and Propagation and USNC-URSI Radio Science Meeting*, Atlanta, GA, USA, 2019, pp. 1739–1740.

1.4 Thesis Organization

Following this first introductory chapter, Chapter 2 deals with an overview of metamaterial absorbers and graphene, as well as the introductions of several important concepts and basic theory used later in followed chapters, and along with the principle of anti-phase reflection cancellation with AMCs and the abbreviated introduction of genetic algorithm. The overview mainly includes a review of the development of electromagnetic absorbers and graphene, together with previously proposed papers and works that covered these topics. A particular focus is given to the attempts to obtain broad effective absorption bandwidth, along with the metamaterial absorbers designed or fabricated with graphene.

Chapter 3 concerns the multilayer structure approach and equivalent circuit model method. Two multilayer broadband metamaterial absorbers operating in microwave frequency bands are

designed through this approach with printed graphene patterns and analyzed through equivalent circuit model method. For the second absorber in section 3.2, a wide-angle impedance matching layer is added on top of the structure to guarantee the absorption performance of this absorber at relatively lower microwave frequencies.

Chapter 4 focuses on the ohmic contact excited eddy current approach. An ultra-thin metamaterial absorber with an ultra-wide relative absorption bandwidth of 178% is designed with printed graphene resistive sheets to demonstrate the outstanding efficacy of the eddy current approach. The surface currents distribution and the power loss density of the absorber are investigated and analyzed to verify the influence of eddy currents on the effective absorption performance.

Chapter 5 demonstrates the anti-phase reflection cancellation approach realized through printed graphene AMCs. A broadband printable and flexible AMC based radar absorber is carried out numerically and experimentally. The new guideline of required reflection phase difference is investigated. The fabrication process and experimental measurement process are introduced in detail.

In Chapter 6, genetic algorithm is utilized to optimize the printed graphene AMC based absorber. Functional unit cells with different size are optimized in succession. The data derived from the program is analyzed to discuss about the convergence and drawbacks of the program for further improvement.

Chapter 7 concerns the tunable THz metamaterial absorber composed of monolayer graphene pattern designed through pattern engraving approach. Modelling of graphene in THz regime with CST Microwave Studio is introduced first, followed by the detailed unit cell design and investigations of different parameters.

The last chapter summaries the study in this thesis and concerns itself with a discussion of future plans for related work.

Chapter 2: Literature Reviews and Background Theory

2.1 Metamaterial Absorbers

2.1.1 Conventional radar absorbers

The theoretical and experimental work with electromagnetic wave absorbers started in the mid 1930's. The first patented absorber in 1936 was a quarter-wave resonant type for the 2-GHz region, which was designed to cover the rear of an antenna to improve the front-to-back ratio [4].

As radar became more and more important during World War II, the practical useful radar absorbers began to attract increasing attentions. Both Germany and the United States built up projects which carried a few absorber ideas from research. The Germans mainly focused on absorbers for radar camouflage, while the United States focused on using absorbers to improve radar performance through reducing interfering reflections from nearby objects [4]. From the projects came two well-known absorbers. One was the so-called Salisbury screen absorber [22], which was one of the first concepts in radar absorbers. Fig. 2.1 (a) shows the original schematic diagram draft of Salisbury screen. Through locating a resistive sheet with 377 Ω/sq resistance at a quarter-wavelength distance away from the metal reflecting surface, a resonant absorber could be achieved. With the quarter-wavelength thick spacer, the electric and magnetic field from screen 11 would be 180 °out of phase with the electric and magnetic field of the radiation reflected from the surface 10 and could cancel it entirely or greatly reduce it [22]. The other was known as the Jaumann absorber, which was a 3-in thick rigid broadband material composed of alternate layers of rigid plastic and resistive sheets with resistance decreasing at a near exponential rate toward the back surface to provide a gradual transition from a low loss to a high loss medium [4].

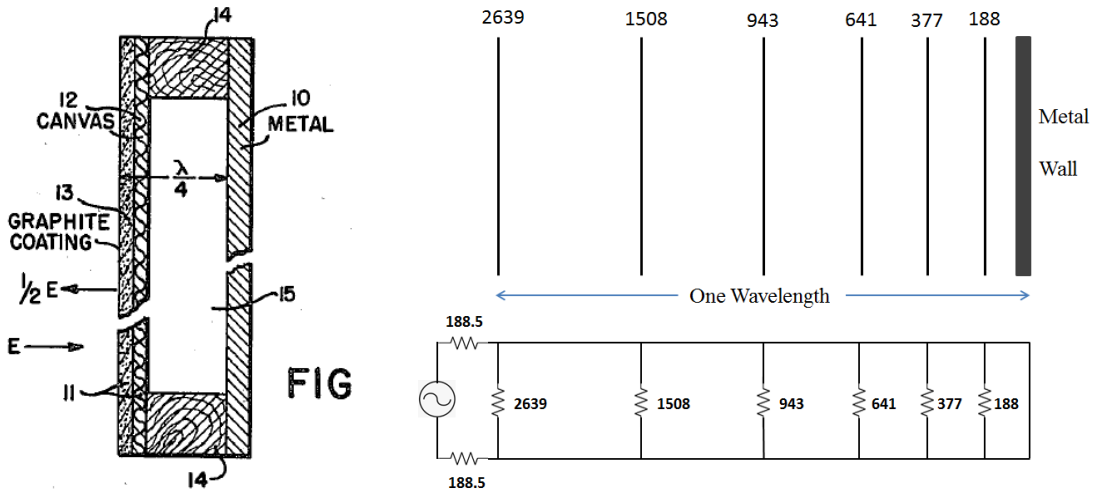

(a) *(b)*

Fig. 2.1 (a) Schematic diagram draft of Salisbury screen [22]. (b) An example of Jaumann Sandwich using a straggered array of resistive sheets, and its transmission line model under normal incidence. Both the resistances and the distances from the metal wall are tapered.

In 1950s, a novel idea of broadband absorber design emerged. The idea was based on arranging gradually tapered material from characteristics near that of free space at the front surface to those of a dissipative medium at the back surface [23, 24]. Low reflection over a wide band of frequencies could be achieved through use of long gradual geometrical transition from a sharp point into dissipative material [4]. A variety of surface geometrics, such as pyramids, cones, and wedges, were carried out through experiments during that period, as shown in Fig.2.2. This idea has still been used even in the recently past decades [25]–[27]. The tapered shape of the pyramidal material performs a role similar to the tapered resistances of the Jaumann Sandwich structure as the example displayed in Fig 2.1 (b) [26]. As the electromagnetic waves pass into the pyramid, many small reflections are created and tend to cancel out [27]. The pyramids have to be at least one half wavelength long at the lowest frequency of interest to be effective, although this size can be reduced by the fact that the wavelength is mitigated when the electromagnetic waves pass through the pyramidal material, the use of technologies such as ferrite tiles other than pyramidal absorbers are still required to provide anechoic effects below 100 MHz because of the large size needed [26]. What makes ferrite tiles work is that their complex permeability and permittivity make them lossy materials and the waves passing through the ferrite materials can be

attenuated. Nowadays, the special RF (radio frequency) absorbing pyramidal materials widely utilized in the RF anechoic chambers are commonly carbon loaded foam pyramids with the gradual taper from tip to core. Sharp tips on the absorbers keep RF waves from bouncing off, allowing the radio waves to slowly transition from air to the lossy carbon inside of the foam.

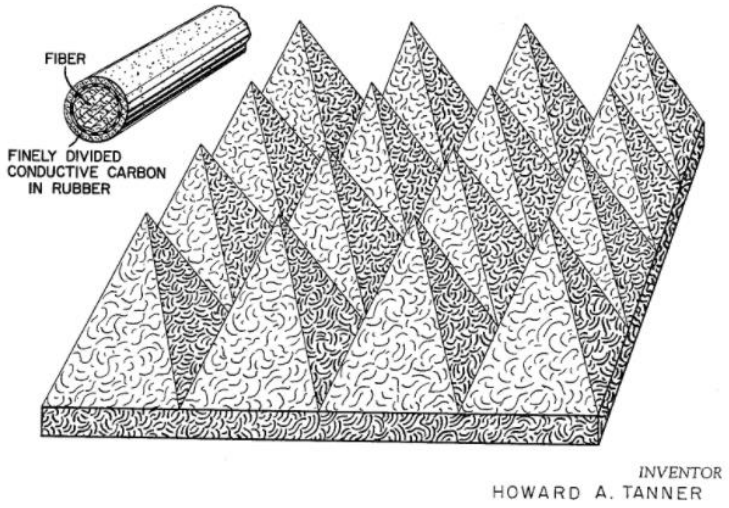

Fig. 2.2 Fibrous microwave absorber with gradually tapered geometry [24].

A type of resonant electromagnetic wave absorber, known as the crossed grating absorber [28]–[30], was proposed in 1970s. This type of absorber developed from the postulate of the possible effects of anomalous diffraction [31]. Through a reflective metal plane with an etched shallow periodic grid, a resonance could be created due to the interaction between the periodic grid and incident radiation, leading to a period of anomalous diffraction [28]. However, this kind of absorber was mainly used to absorb visible spectrum and was hard to be implemented with microwaves absorption.

Althrough the conventional radar absorbers can provide effective absorption, their limitations are obvious. For example, the limitation of Salisbury screen is the narrow operation bandwidth since it only works at one specific frequency. For Jaumann Sandwich, the wider operation frequency bandwidth achieved, the more layers of resistances needed, which might lead to a large thickness and size of the absorber. As to the pyramidal materials, the lower operation frequency band means larger size of absorbers.

2.1.2 Electromagnetic metamaterials

Electromagnetic metamaterials [32, 33] are arrays of structured subwavelength elements which may be described as effective materials via $\varepsilon(\omega)$ and $\mu(\omega)$, the electric permittivity and magnetic permeability, respectively [6].

From the electromagnetic point of view, the wavelength λ determines whether a collection of atoms or other objects can be considered a material. Consider light, which is an electromagnetic wave consisting of oscillating electric and magnetic fields, passing through a plate of glass. Since visible light has a wavelength which is hundreds of times larger than the atoms of which the glass is composed, the atomic details lose importance in describing how the glass interacts with light [34]. In practice, the atomic scale can be averaged, conceptually replacing the otherwise inhomogeneous medium by a homogeneous material characterized by just two macroscopic electromagnetic parameters: the electric permittivity and magnetic permeability [34].

The electromagnetic parameters ε and μ need not arise strictly from the response of atoms or molecules: any collection of objects whose size and spacing are much smaller than λ can be described by an ε and μ. Although such an inhomogeneous collection may not satisfy the intuitive definition of a material, and electromagnetic wave passing through the structure cannot tell the difference [34]. In this way, from the electromagnetic point of view, an artificial material, or metamaterial, is created. Values of electric permittivity ε and magnetic permeability μ are determined by the scattering properties of the structured objects, which means that metamaterials owe their properties to subwavelength details of structure rather than to their chemical composition, and this leads to the design flexibility of metamaterials to have properties impossible to find in nature [35].

A negative index of refraction is an example of a material property that does not exist in nature but has been enabled by using metamaterial concepts [35, 36]. Negative index of refraction is a phenomenon first postulated by Veselago in 1968 [37] and was experimentally demonstrated in [38] and [39]. In addition to negative refractive index, many other applications of

metamaterials were demonstrated including invisibility cloaking [40], perfect lenses [41], and aberration free lenses [42]. Besides, the exotic and manipulatable electromagnetic characteristics make metamaterials perfect candidates for EM wave absorbers [8].

To understand the importance of metamaterials for EM wave absorbers, the general theoretical background is briefly introduced in the followed paragraphs.

Based on Fresnel equation, the reflectivity at the air interface of a medium with refractive index *n* for transverse electric (TE) and transverse magnetic (TM) polarized waves are as follow [6]:

$$R_{TE} = \left| \frac{cos\theta - \frac{\sqrt{n^2 - sin^2\theta}}{\mu_r}}{cos\theta + \frac{\sqrt{n^2 - sin^2\theta}}{\mu_r}} \right|^2 \tag{2.1}$$

$$R_{TM} = \left| \frac{\varepsilon_r cos\theta - \sqrt{n^2 - sin^2\theta}}{\varepsilon_r cos\theta + \sqrt{n^2 - sin^2\theta}} \right|^2 \tag{2.2}$$

where θ is the angle of incidence, ε_r and μ_r are electric permittivity and magnetic permeability of the medium, respectively, and $n = \sqrt{\varepsilon_r \mu_r}$ is the refractive index of the medium. In the case of normal incident angle, i.e. $\theta = 0^{\circ}$, the above equations reduce to [6],

$$R_{TE} = \left| \frac{1 - \frac{n}{\mu_r}}{1 + \frac{n}{\mu_r}} \right|^2 \tag{2.3}$$

$$R_{TM} = \left| \frac{\varepsilon_r - n}{\varepsilon_r - n} \right|^2 \tag{2.4}$$

According to Kirchhoff's rule, the sum of the transmittance $T(\omega)$, reflectance $R(\omega)$, and absorbance $A(\omega)$ should be equal to 1 in the absence of scattering and diffraction [43]. In the case of electromagnetic wave absorbers, by using the metallic ground plane, a zero transmissivity can be achieved, and the absorptivity can therefore be written as $A(\omega) = 1 - R(\omega)$.

For transverse electric and transverse magnetic polarized waves, the absorptivity equations are as follow,

$$A_{TE}(\omega) = 1 - R_{TE}(\omega) = 1 - \left|\frac{Z - Z_0}{Z + Z_0}\right|^2 = 1 - \left|\frac{\mu_r - n}{\mu_r + n}\right|^2 \tag{2.5}$$

$$A_{TM}(\omega) = 1 - R_{TM}(\omega) = 1 - \left|\frac{Z - Z_0}{Z + Z_0}\right|^2 = 1 - \left|\frac{\varepsilon_r - n}{\varepsilon_r + n}\right|^2 \tag{2.6}$$

where Z is the impedance of the material and Z_0 is the impedance of free space.

With the equations listed above, in order to get a near unity absorptivity for both polarizations, the reflectivity should equal to zero, which is equivalent to $\varepsilon_r = \mu_r$. This means impedance of the material should match that of air in order to minimize the reflection [44].

Metamaterials allow for the explicit design of the effective parameters $\varepsilon(\omega)$ and $\mu(\omega)$. Hence, the design flexibility of metamaterials makes them excellent candidates for electromagnetic wave absorbers.

2.1.3 Microwave metamaterial absorbers

As mentioned in section 2.1.1, conventional radar absorbers suffer from many disadvantages. In order to overcome the limitations of the conventioanl radar absorbers and provide absorbers with better properties and design flexibility, Engheta proposed to introduce metamaterials to the design of absorbers in 2002 [7]. Although the operational bandwidth was still limited, this technological breakthrough reduced the thickness drastically.

The first experimentally demonstrated metamaterial absorber was proposed by Landy *et al*. in 2008 [8]. As shown in Fig. 2.3, the structure was composed of two metallic layers and a dielectric substrate. The top layer consisted of an electric ring resonator which provided the electric response along with the ground plane by coupling strongly to incident electric field at a certain resonance frequency. The second metallic layer, which consisted of a cut wire in a parallel plane, also contributed to the electric response [8]. These two metallic layers were spaced apart by a

dielectric substrate. The magnetic coupling was achieved via antiparallel currents in the centre wire of the electric ring resonator from the top metallic layer and the cut wire from the second metallic layer. An incident time varying magnetic field might couple to these antiparallel currents, giving a Lorentz like magnetic response [8]. Since the structure consisted of two metamaterial resonators that coupled separately to electric and magnetic fields, the combined design allowed for individual tuning of the electric and magnetic responses.

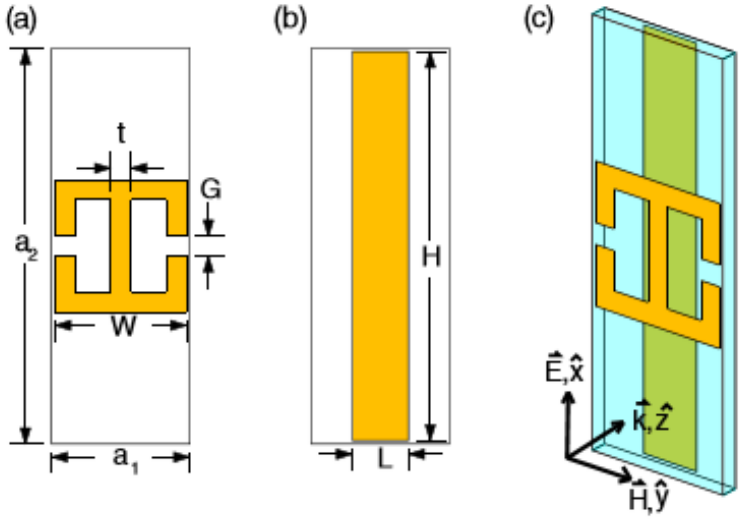

Fig. 2.3 Electric resonator (a) and cut wire (b). The unit cell is shown in (c) with axes indicating the propagation direction [8].

The absorber in [8] was demonstrated a simulated absorptivity of 99% at 11.48 GHz and experimentally achieved a peak absorption greater than 88% at 11.48 GHz. Although the properties of less thickness and lightweight had been achieved, the absorber was still limited by narrow bandwidth due to its single resonating structure. In the past decades, there are three widely used approaches developed to widen the operation bandwidth of metamaterial microwave absorbers. The first one is the use of lumped elements [45]–[47], as the one displayed in Fig. 2.4. The proposed absorber has a unit cell structure as shown in Fig. 2.4(a), where four lumped resistors are mounted on each unit cell to obtain a broad absorption band. It can be observed from Fig. 2.4(b) that as the resistance value increases, the full width at half maximum bandwidth of the structure decreases gradually [46]. An optimum value of resistor (Rc = 150Ω) can provide a wide

absorption bandwidth as well as maintain the −10 dB reflection level. Although the effect of lump loaded approach has been experimentally demonstrated, this approach results in the complexity of fabrication due to the resistors on each unit cell.

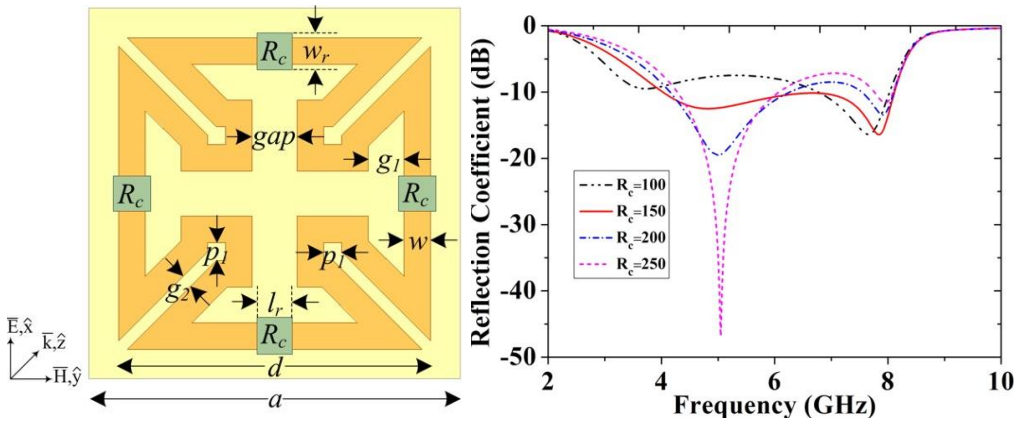

(a) *(b)*

Fig. 2.4 (a) Front view of the unit cell geometry. (b). Reflection coefficient for different chip resistor (*Rc*) values of the proposed absorber [46].

Comparing with the lump loaded method, a more simple and effective approach to obtain broadband absorption is to create multiple resonances through adding more resonators with different shaped patterns on the same plane [48]–[50]. Fig. 2.5 shows an example of this approach. The proposed absorber is a combination of two different structures with individual microstrip bends (I and II). From Fig. 2.5(c), it is observed that the structure I on its own achieves 70% absorption from about 8 GHz to 13.9 GHz, while the structure II on its own achieves 90% absorption from 13.8 GHz to 20.3 GHz. As the absorption bands of two structures are continuous while their absorption peaks are well apart from each other, it can be expected that the combination of them can provide a broadband absorption, as shown in Fig. 2.5(b).

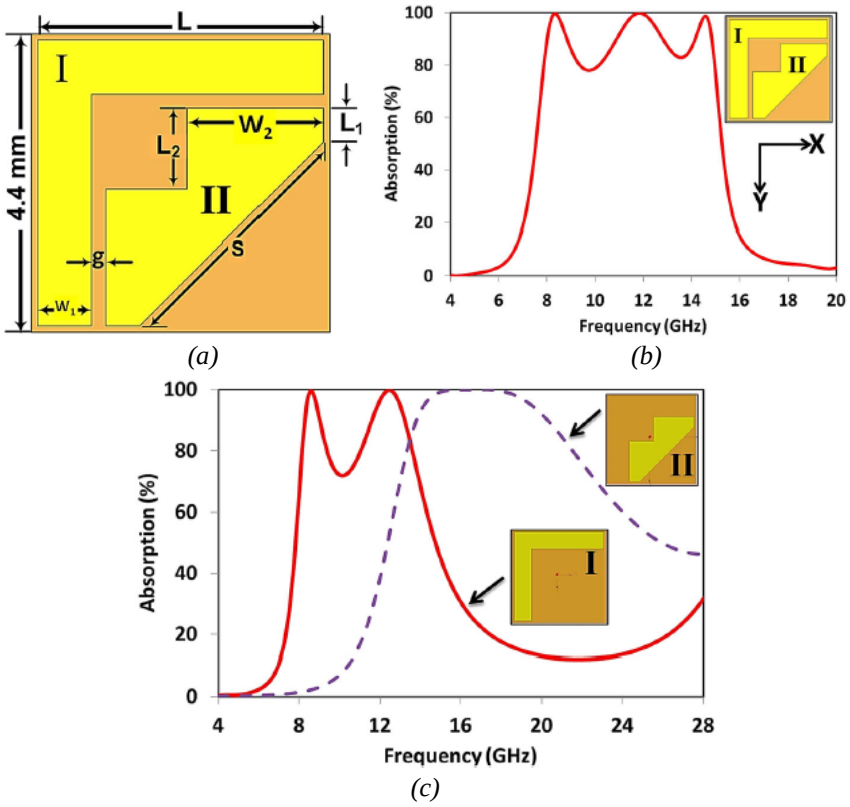

Fig. 2.5 (a) Front view of the proposed unit cell structure with geometrical dimensions. (b) Simulation results of the proposed structure. (c) Simulated absorption of the individual structure I and II [50].

Fig. 2.6 displays an example of the third approach, which introduces multiple resonances through multi-layer structures [51]–[54].This absorber is composed of two dual-band sub-cells. Between these two sub-cells, there is an air spacer with height *t*. The surface of each layer is covered by a metallic pentagon pattern. The bottom of second layer is a metal ground plane. Fig. 2.6(c) displays the simulated result of this absorber. Four absorption peaks of resonance are observed at f_1 = 9.14GHz, f_2 = 10.46GHz, f_3 = 11.86GHz, and f_4 = 13.67GHz. At these frequencies, the absorption is nearly perfect [51].

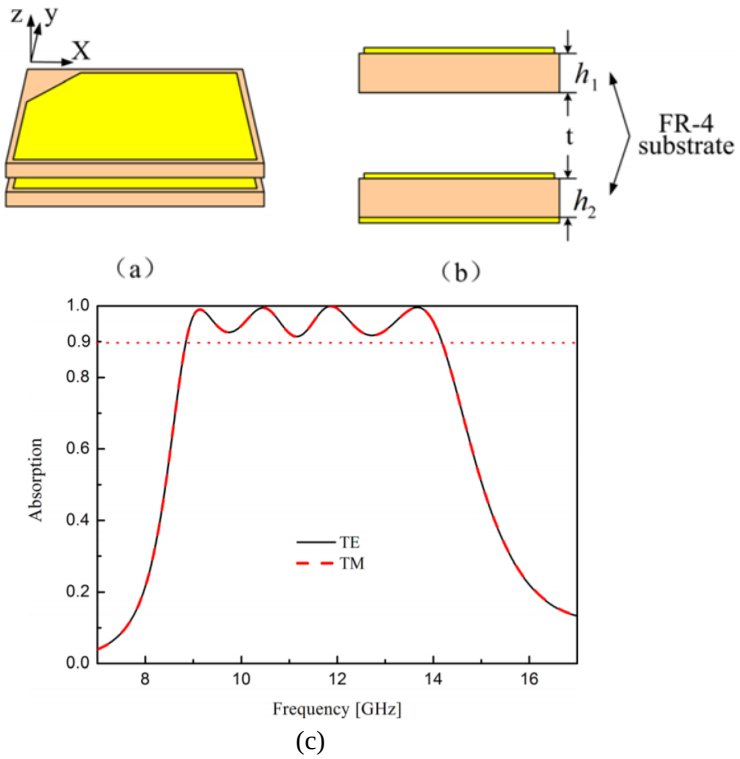

Fig. 2.6 Unit cell of the metamaterial microwave absorber: (a) the perspective view and (b) side view. (c) Simulated absorption of the absorber [51].

Fig. 2.7 shows the simulated surface current distribution at four resonant frequencies, illustrating the mechanism of the multi-layer absorber. In Fig. 2.7(a) and 2.7(b), the surface current of the metal ground plane is anti-parallel to the surface current of the metallic pentagon pattern of the lower layer, and the current loop is driven by the incident H-field, resulting in a strong magnetic resonance. As the electric response and the magnetic response appear simultaneously at the resonant frequency f_1 = 9.14 GHz and f_2 = 10.46 GHz, the absorber can absorb the incident EM waves. Since the surface current of the upper layer metal pattern is not anti-parallel to the current of the lower layer pattern or the ground metal plane, the magnetic resonance at frequency f_1 = 9.14 GHz and f_2 = 10.46 GHz is mainly induced by the lower layer sub-cell. For Fig. 2.7(c) and 2.7(d), it can be observed that the anti-parallel current exists in both layers, which means the magnetic resonance at these two frequencies is induced by the two layers together, or it can be explained as the magnetic resonance is induced by upper layer and strengthened by lower layer [51].

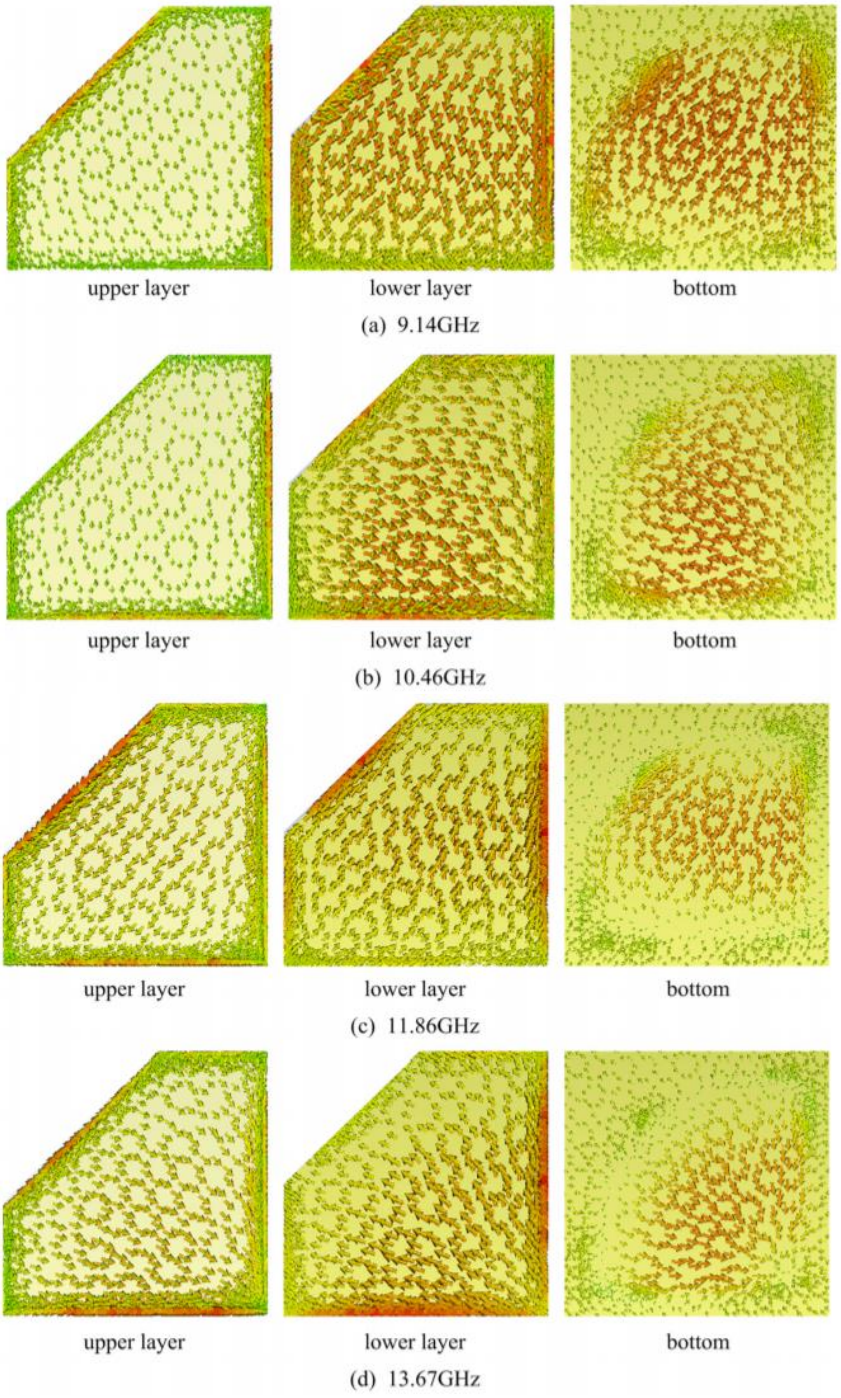

Fig. 2.7 Simulated surface current distribution for the broadband metamaterial microwave absorber at resonant frequencies [51].

2.1.4 THz metamaterial absorbers

Terahertz (THz) regime, which has inherent advantages in civil and military applications, is widely applied in detectors [55, 56], sources [57]–[59], imaging [60]–[62], sensors [63]–[65], and

security systems [66,67]. Since few nature materials can respond to THz frequency, the potential payoffs of metamaterials drive a great of interest in THz-related applications [68]. In particular, due to the extensive requirements of absorbers in system applications [69]–[71], the research of THz metamaterial absorbers [72, 73] gets a very rapid growth in recent years.

With different structures and periodic patterns, a variety of metamaterial absorbers with single-band [74, 75], multi-band [76], and broadband [77] absorption have been designed in spectral ranges of microwave [78, 79], terahertz [80], and optical regimes [81]. Among these absorbers, the broadband metamaterial absorbers are of great importance to the applications of THz identification [82, 83], imaging [84], energy harvesting [85], and so on.

For THz regime, two common strategies are utilized to achieve broadband absorption. One is to generate extra resonances [86] which are contiguous in operation frequency band through introducing multiple different geometry patterned resonators on a single layer of unit cell. The other strategy relies on multi-layer structures [87, 88] with different periodic patterns or dielectric substrates for each layer. However, the former method normally leads to more complexity of the periodic patterns and larger size of unit cell, while the second strategy suffers from more sensitive to wide-angle incidence and fabrication complexity due to the multi-layer structures.

In addition to wide operation bandwidth, tunable property is also an attractive function for THz metamaterial absorbers [89]–[91]. The previous reported tuning approaches can be classified into two categories. The first one depends on mechanical changes, such as tuning through nanoelectromechanical systems (NEMS) [92] and stretchable metasurfaces [93]. The second category realizes tunability through incorporating active materials including Vanadium di Oxide (VO_2) [76, 94], liquid crystals [95], Indium Tin Oxide (ITO) [96], and phase change materials (PCMs) [97]. The properties of active materials can be controlled by an external stimulus instead of mechanical changes, which provides a higher tuning speed [98].

As a single layer two dimensional hexagonal structured lattice of carbon atoms, graphene has become the most popular material in recent years due to its interesting electromagnetic properties

[99]. More importantly, the conductivity of graphene can be dynamically changed by tuning its Fermi energy through an external DC voltage [100]. The unique properties make graphene a perfect candidate for tunable broadband THz metamaterial absorbers [101]–[104]. Fig. 2.8 displays a tunable multi-band THz absorber using a single-layer square graphene ring structure [104]. Although the absorption spectra can be tuned by changing the geometric dimensions of the patterns, the physical dimensions are fixed once the absorber is eventually fabricated. However, the tunability of graphene makes the tunable property of THz absorber possible. As shown in Fig. 2.8 (b), it can be seen that the absorption performance can be manipulated by changing the chemical potential of graphene pattern. As the value of chemical potential increases, the absorption peaks move to higher frequencies.

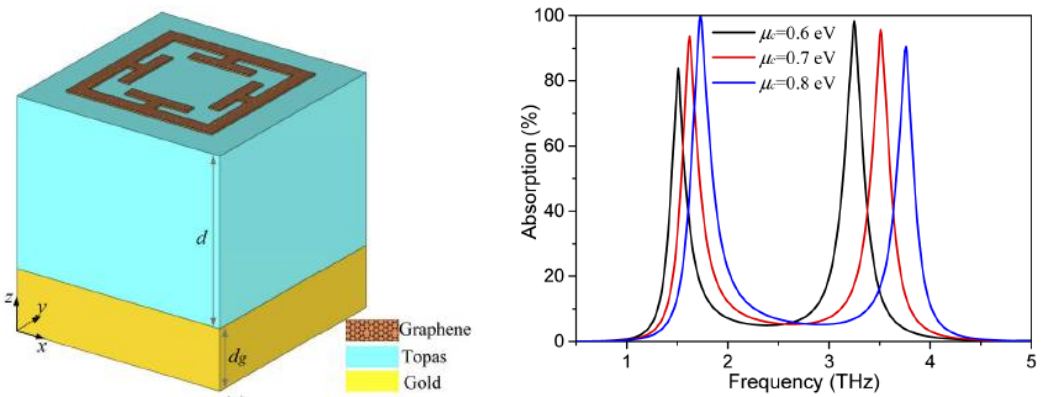

(a) (b)

Fig. 2.8 (a) Perspective view of the proposed graphene-based dual-band THz absorber. (b) Absorption spectra with different values of graphene chemical potential under normal TE incident wave [104].

2.2 Graphene

2.2.1 Geometry of monolayer graphene

Graphene is a 2D allotrope of carbon, which is made out of carbon atoms arranged on a honeycomb structure, as shown in Fig. 2.9. Graphene is exactly one layer of graphite [105], which is ideally an infinite plane. However, real graphene exhibits edges that can either be zigzag or arm-chair (in Fig. 2.9 (b)) [106]. Graphene has been theorized by scientists for decades and has likely been produced unknowingly in small quantities for centuries, through the use of pencils or other similar applications of graphite [107]. It was isolated and characterized in lab in 2004 by

Andre Geim and Konstantin Novoselov at the University of Manchester [10], who were later awarded the Nobel Prize in Physics for their research on this material.

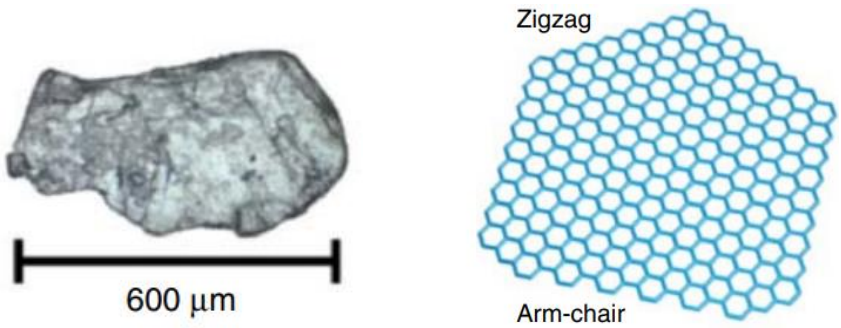

(a) (b)

Fig. 2.9 (a) A flake of natural graphite [106]. (b) Graphene with zigzag and arm-chair edges [108].

Graphene plays an important role among systems with only carbon atoms. Fig. 2.10 shows several allotropes of carbon. The three dimensional allotrope of carbon in Fig. 2.10 is graphite, which is made out of stacks of graphene layers that are weakly coupled by van der Waals forces [109]. Carbon nanotubes, which can be obtained by rolling graphene along a given direction and reconnecting the carbon bonds, have only hexagons and can be thought as one-dimensional objects [110]. Fullerenes are molecules where carbon atoms are arranged spherically [111]. It can be obtained from graphene with the introduction of pentagons which create positive curvature defects. From the physical point of view, fullerenes are zero-dimensional objects with discrete energy states. On the other hand, it can also be thought as wrapped up graphene [109].

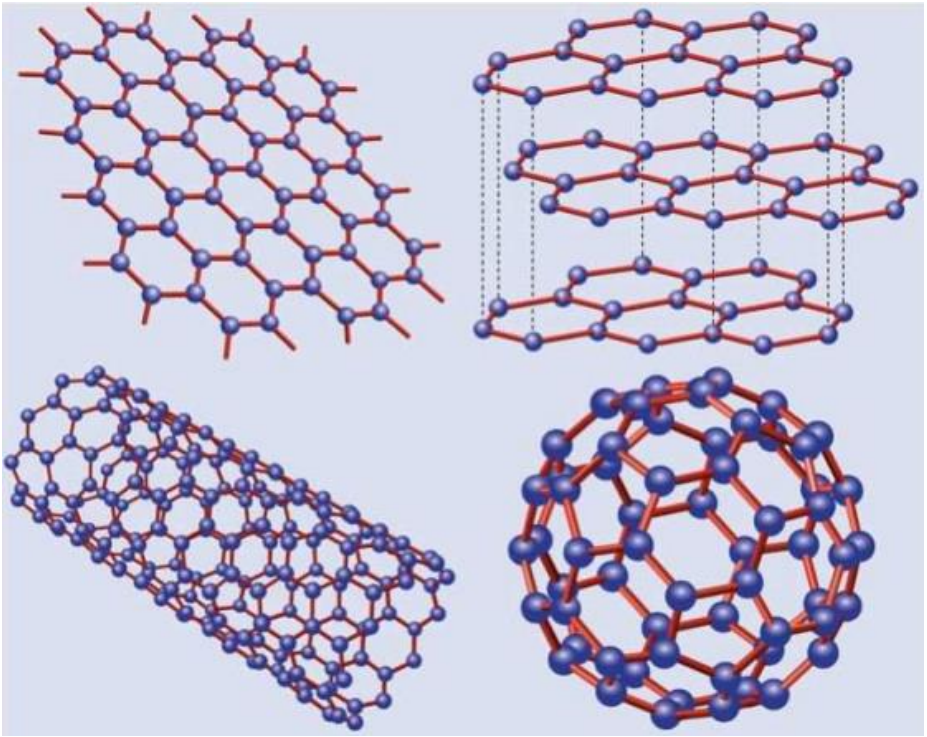

Fig. 2.10 Allotropes of carbon: Graphene (top left) is a honeycomb lattice of carbon atoms; graphite (top right) can be viewed as a stack of graphene layers; carbon nanotubes (bottom left) are rolled-up cylinders of graphene; fullerenes (C_{60}) are molecules consisting of wrapped graphene by the introduction of pentagons on the hexagonal lattice [109].

The structural flexibility of graphene is reflected in its electronic properties. The sp^2 hybridization between one s-orbital and two p-orbitals leads to a trigonal planar structure with a formation of a σ-bond between carbon atoms which are separated by 1.42 Å. The σ-bond is responsible for the robustness of the lattice structure in all allotropes. The unaffected p-orbital, which is perpendicular to the planar structure, can bind covalently with neighbouring carbon atoms leading to the formation of a π-band [109]. Since each p-orbital has one extra electron, the π-band is half-filled. The Coulomb energies are very large due to the strong tight binding character of the half-filled bands, leading to strong collective effects, magnetism, and insulating behaviour due to correlation gaps or Mottness [112].

Fig. 2.11 shows the hexagonal structure with carbon atoms. Generic honeycomb lattices consist of two interpenetrating triangular sub-lattices denoted A (the blue one) and B (the yellow

one). The structure can be seen as a triangular lattice with a basis of two atoms per unit cell. The lattice vectors can be written as [109],

$$a_1 = \frac{a}{2}(3, \sqrt{3}), \qquad a_2 = \frac{a}{2}(3, -\sqrt{3}) \tag{2.7}$$

where $a \approx 1.42$ Å is the carbon-carbon distance. The reciprocal lattice vectors are therefore,

$$b_{1,2} = \frac{2\pi}{3a}(1, \pm\sqrt{3}) \tag{2.8}$$

Each lattice position has three nearest neighbours separated by

$$\delta_1 = \frac{a}{2}(1, \sqrt{3}), \qquad \delta_2 = \frac{a}{2}(1, -\sqrt{3}), \qquad \delta_3 = -a(1,0) \tag{2.9}$$

The positions of two points *K* and *K'* at the corners of the graphene Brillouin zone are given by,

$$K = \left(\frac{2\pi}{3a}, \frac{2\pi}{3\sqrt{3}a}\right), \qquad K' = \left(\frac{2\pi}{3a}, -\frac{2\pi}{3\sqrt{3}a}\right) \tag{2.10}$$

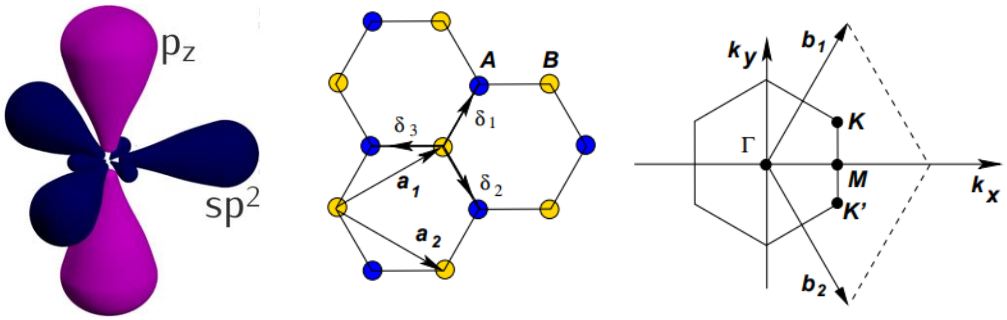

Fig. 2.11 Left: The sp^2 hybridization has three major lobes at 120 °, while the remaining p-orbital is sticking out of the graphene's plane. Middle: Lattice structure of graphene, consisting of two interpenetrating triangular lattices (a1 and a2 are the lattice unit vectors and δ_i are the nearest neighbour vectors). Right: Corresponding Brillouin zone. The Dirac cones are located at the K and K' points [109].

2.2.2 Properties of graphene

Graphene is known as the thinnest material ever made with the one-atom thickness of 0.345 nm. The density of graphene is 0.77 mg per square meter [113]. Although graphene has the thinnest thickness and light weight, it is the strongest material ever tested, with an intrinsic tensile

strength of 130 GPa and a Young's modulus close to 1 TPa [114, 115]. The Nobel announcement illustrated this by saying that a 1 square meter graphene hammock would support a 4 kg cat but would weigh only as much as one of the cat's whiskers, at 0.77 mg, which is about 0.001% of the weight of 1 m^2 of paper [116].

Thermal transport in graphene has attracted attention due to the potential for thermal management applications. Early measurements of the thermal conductivity of suspended graphene reported an exceptionally large thermal conductivity up to 5300 $W \cdot m^{-1} \cdot K^{-1}$ [117]. However, later studies primarily on more scalable but more defected graphene derived through chemical vapor deposition (CVD) method were unable to reproduce such high thermal conductivity measurements, producing a wide range of thermal conductivities between 1500–2500 $W \cdot m^{-1} \cdot K^{-1}$ for suspended single layer graphene [118]–[121]. The large range in the reported thermal conductivity can be caused by the difference of graphene quality and the measurement conditions. The potential for the high thermal conductivity can be seen by considering graphite, the 3D version of graphene that has basal plane thermal conductivity of over a 1000 $W \cdot m^{-1} \cdot K^{-1}$ comparable to diamond [122, 123].

With the outstanding properties such as the thin thickness, light weight, excellent intrinsic tensile strength and thermal characteristics, graphene is naturally a great candidate for metamaterial absorbers. Additionally, the tunability of carrier density under a modulating electrical field makes graphene appropriate for designing flexible components, including tunable flexible THz metamaterial absorbers [124]. The tunable property of graphene can be realized by applying external electric field, such as an external DC voltage. Fig. 2.12 shows the tunability of graphene. At frequency lower than 100 GHz, the real part and the imaginary part of graphene's surface conductivity almost stay frequency independent, while at frequency of lower THz, both of the two parts can be tuned according to various values of chemical potential.

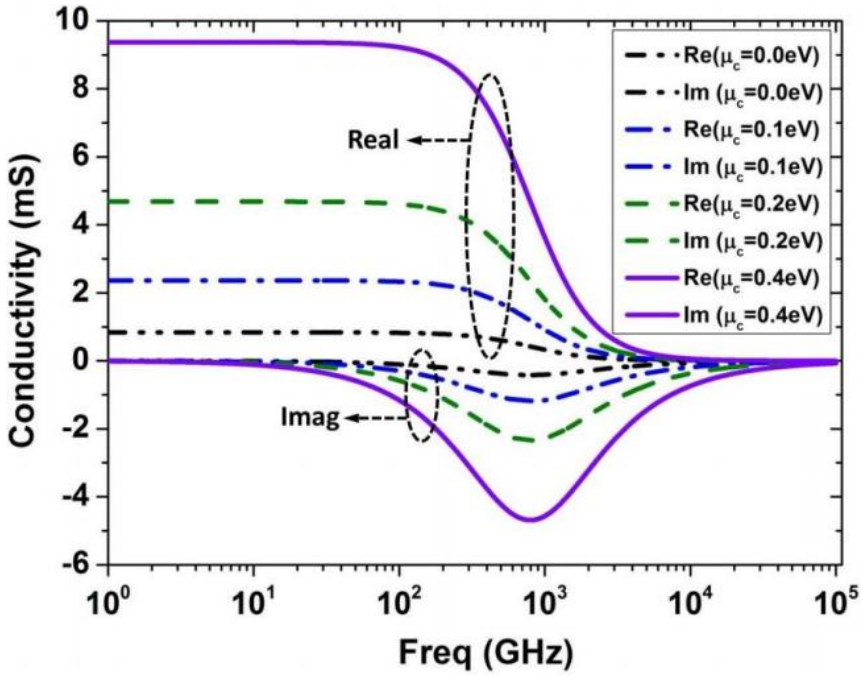

Fig. 2.12 The tunability of graphene's surface conductivity from microwave to THz frequency bands [125].

2.2.3 Graphene synthesis

The access to graphene is one hurdle for the development of applications based on graphene. Generally, there are two approaches to graphene. One is bottom-up approach which starts from small molecules that are used to build up graphene, while the other one is top-down approach which starts from graphite [108].

The bottom-up approach focuses on the synthesis of graphene on solids using a carbon source. The mostly chosen method is chemical vapor deposition (CVD) [126] using a metal surface and small molecules, such as methane or acetylene. Different metal surfaces [127]–[129] have been used in this approach, but the most popular substrate is still copper. Typical copper foils used are polycrystalline with a thickness of around 25 μm. The growth temperature is about 1000 °C. The carbon source, such as methane, is used in a mixture with hydrogen and reacts on the surface with the C – H bonds cleaved [130, 131]. Carbon segregates on the surface and forms graphene. When crystals of graphene grow, they will interact with each other and start to form continuous films (as shown in Fig. 2.13). After the continuous films grown on metal surface, the grown graphene

can be transferred to desired targeting substrate, such as SiO_2 or polymer. The most popular methods for transferring graphene are based on etching or using a polymer, such as poly-methylmethacrylate (PMMA). As displayed in Fig. 2.13 (d), the graphene binds to the PMMA and can be transferred to the desired substrate, and then the PMMA is dissolved with acetone to leave the graphene on the surface [131]. However, the crucial drawback of CVD growth of graphene on copper is the different thermal expansion coefficient of graphene and copper that causes wrinkling of graphene (as shown in Fig.2.13 (e)) after cooling, leading to the reduction of the quality of produced graphene [130].

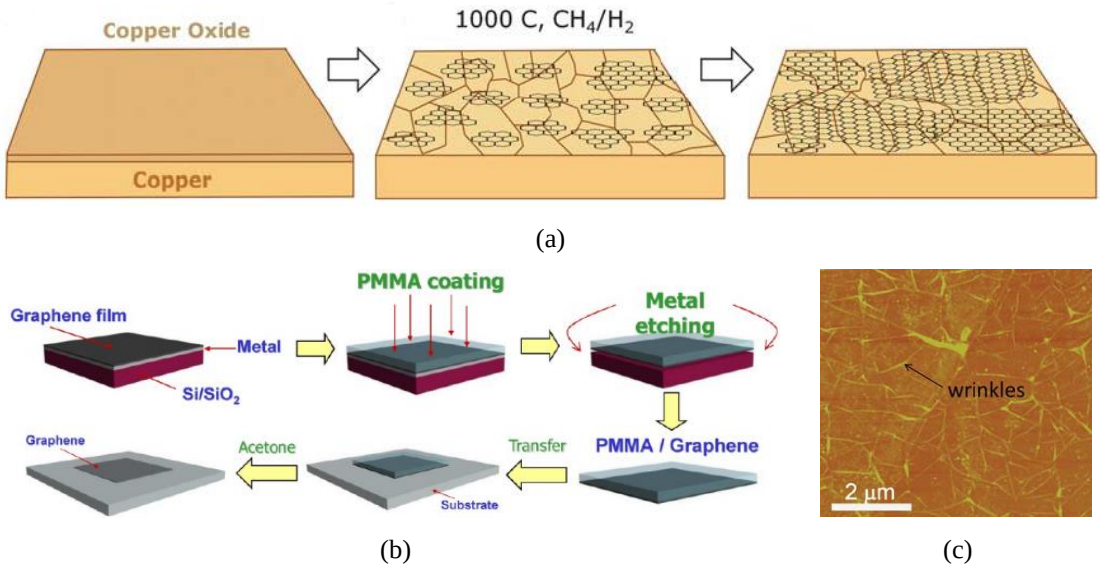

Fig. 2.13 (a) Illustration of the formation process of graphene grown on copper surface. (b) Illustration of the transfer of graphene from metal surfaces by PMMA coating, metal etching, transfer on the desired substrate, followed by dissolution of the polymer, leaving graphene back on the substrate. (c) AFM images of graphene films transferred onto SiO_2, displaying wrinkles [130, 131].

The isolation of graphene from graphite can be performed mechanically using adhesive tape [10, 132], or in solvents by sonication [133]–[136], shear mixing [137], or ball milling [138, 139]. Besides, the delamination of single layers of graphite can be facilitated using chemical methods that involve chemical functionalization and defunctionalization after processing [140, 141]. The most famous method to isolate graphene from graphite is the "scotch tape" method introduced by Novoselov *et al*. [10]. In the procedure of this method, an adhesive tape is used for repeatedly pealing of few-layers of graphene from flakes of graphite. After that, the adhesive tape is placed

on the SiO_2/Si wafer and is pressed gently before peeled slowly off from the wafer. In this way, it is possible to deposit some flakes of graphene on the surface of the wafer [10].Graphene produced with this method has high quality. However, this method is not efficient for technical applications. To produce graphene from graphite more efficiently, other methods have been developed. Fig. 2.14 shows the procedure of liquid phase exfoliation method. The highly oriented pyrolytic graphite is sonicated in solvents, and through centrifugation single layer of graphene can be obtained together with bilayer graphene and few layer graphene [142, 143]. The graphene ink produced through this method can be further deposited and printed on substrate to form uniform films.

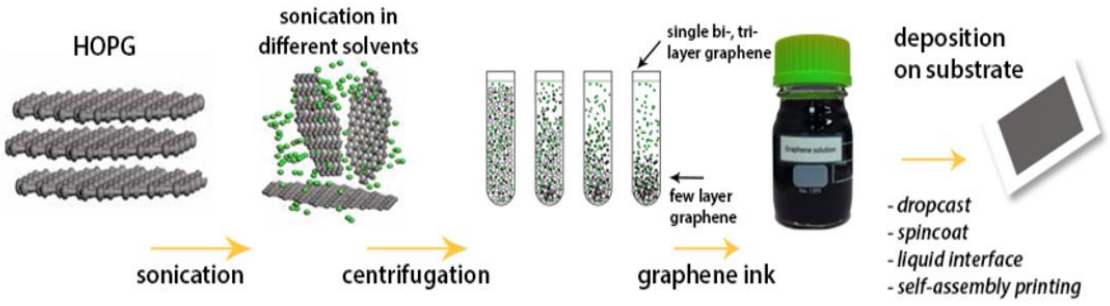

Fig. 2.14 Liquid phase exfoliation of graphene [142].

The challenge that all methods for the synthesis of graphene have in common is that the quality of graphene differs. The density and type of defects can vary strongly depending on the type of processing. The defects can be those within the carbon framework, such as missing atoms or substituted atoms. To determine the quality of graphene by identifying the density of defects within the C-framework, Raman spectroscopic characterization of graphene is the most reliable method [108]. Raman spectroscopy of graphene can be performed by using several laser wavelengths ranging from the blue to red region of the light spectrum, among which the green laser is the most popular one. The Raman spectrum of graphene displays three major peaks (G peak, D peak, and 2D peak) that can be used to evaluate the quality of graphene. The G peak at about 1580 cm^{-1} is an allowed phonon emission and its intensity scales with the number of C-

atoms probed by the laser spot. The D peak at about 1345 cm^{-1} is a consequence of forbidden phonon emission which is only possible due to the activation by defects and, thus, the D peak evolves with the introduction of defects. The 2D peak is the most intense peak in graphene, which is a result of an allowed phonon process. Since the intensity of the G peak remains almost constant, the rising of the intensity of D peak will lead to an increased I_D/I_G ratio [144, 145]. Fig. 2.15 (b) displays the reference Raman spectra of graphene. When the density of defects is 0.77%, the I_D/I_G ratio equals to 2.2 and the distance of defects is about 2 nm, while the 2D peak is barely detectable, which means the structure of graphene is destroyed [145].

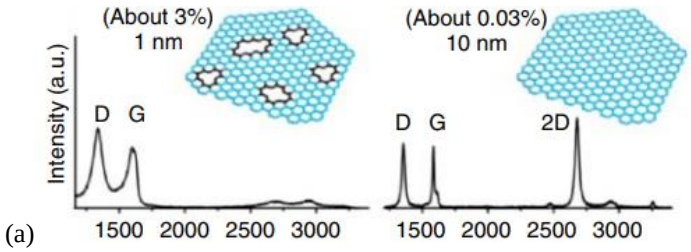

(a)

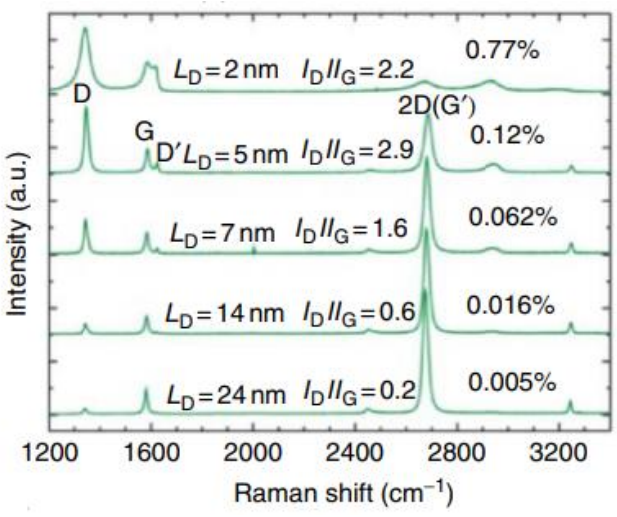

(b)

Fig. 2.15 (a) Raman spectra of graphene with different densities of defects[108]. (b) Reference Raman spectra of graphene that relate to densities of defects between 0.005% and 0.77% [145].

2.2.4 Printed graphene

In the past decades, printed conductive inks for electronic applications have grown rapidly. Among various kinds of conductive inks, silver nanoparticle inks [146, 147] are expensive,

copper nanoparticle inks [148, 149] are cheaper but easy to be oxidized, while conductive polymers [150, 151] are thermal and chemical instable and less conductive. Carbon black and carbon nanotubes [152, 153] have stable properties, but their typical sheet resistance is above 50 Ω/sq, which limits their application for microwave components. Comparing with the conductive inks mentioned above, graphene ink is good candidate for microwave applications due to their high conductivity, relatively low cost and good flexibility. Graphene ink, a dispersion of graphene flakes in solvents, can be easily patterned via spraying [154]–[157], screening printing [158], inkjet-printing [159, 160], and doctor blading [161] technologies.

Fig. 2.16 displays a printed graphene nano-flakes enabled flexible and conformable wideband radar absorber [154]. This absorber was fabricated through spraying method. The printed graphene patterns on top of the absorber have the sheet resistance of around 20 Ω/sq.

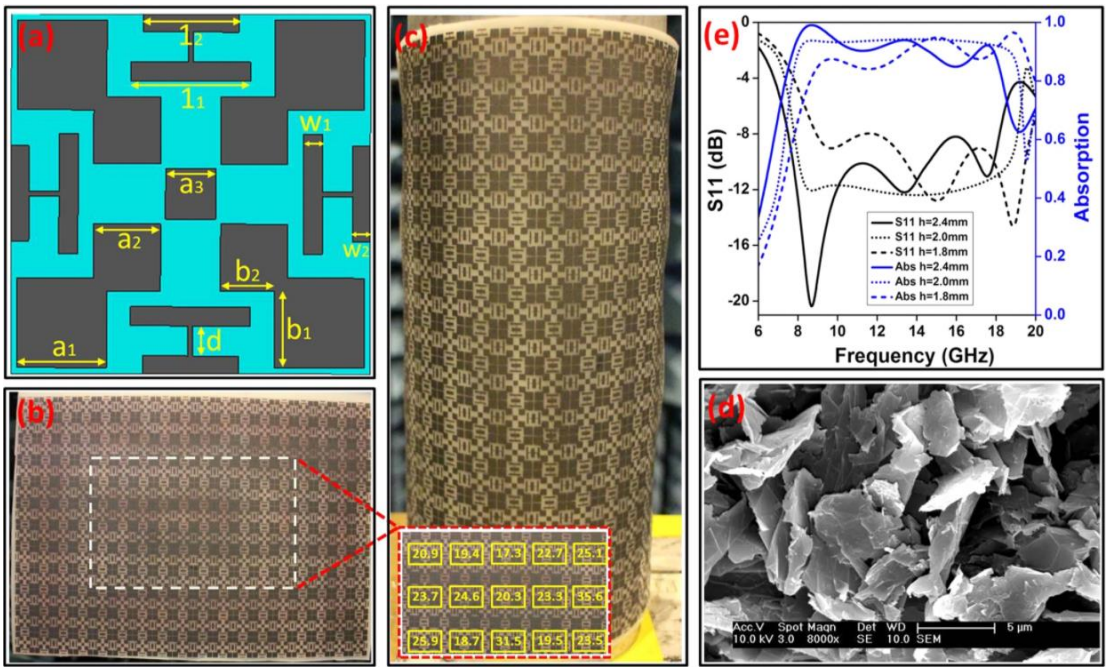

Fig. 2.16 (a) Unit cell structure of the absorber. (b) Fabricate graphene absorber. (c) Flexible absorber conformably bended and attached to a metal cylinder. (d) SEM of top-view printed graphene. (e) Simulated S_{11} and absorption of graphene absorber under different substrate thickness [154].

Fig. 2.17 illustrates the printed graphene antennas. These antennas were designed for low cost, flexible and disposable wireless applications. They were printed on A4 papers through screen printing method. The printed graphene patterns have a sheet resistance of 37 Ω/sq, which can be

improved to be 1.2 Ω/sq on average after compression process. The printed patterns have excellent mechanical flexibility, which has a great potential in wearable and deformable applications [158].

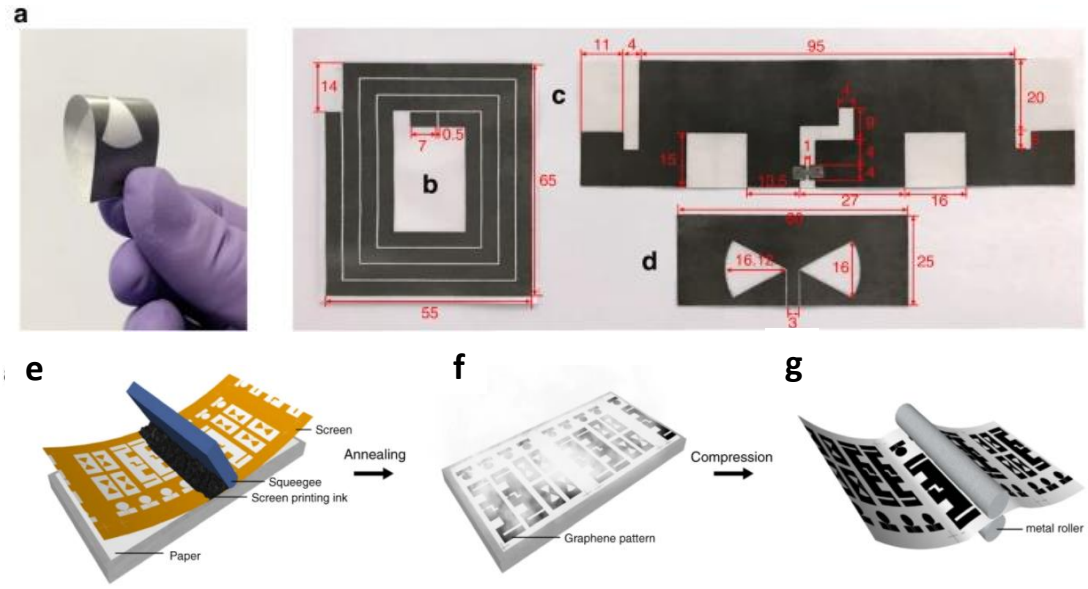

Fig. 2.17 (a) Flexibility of the printed graphene antenna. (b)–(d) Printed graphene antennas. And screen-printing steps: (e) patterning graphene ink via exposed screen and squeegee, (f) annealing printed patterns and (g) compressing dried pattern with steel rolling machine [158].

2.3 Important Concept and Basic Theory

2.3.1 Sheet resistance and measurement (4-point)

For microwave absorbers, thin films of conductors are normally dealt with. The concept of sheet resistance is critical to an understanding of thin film conductors, especially in microwave engineering where skin depth is very small. Sheet resistance is a convenient measurement of resistance of thin films which are nominally uniform in thickness. Sheet resistance is applicable to two-dimensional systems. When the term sheet resistance is used, it is implied that the current is along the plane of the sheet. Sheet resistance is usually expressed in ohms per square (Ω/sq) [162].

For a regular three-dimensional conductor, the resistance can be calculated as,

$$R = \rho \frac{L}{Wt} \tag{2.11}$$

where ρ is the bulk resistivity (Ω.m) which is a property that is independent of frequency and geometry, L is the length of the conductor, W is width, and t is the thickness.

Upon combining the resistivity with the thickness, (2.11) can be written as,

$$R = \frac{\rho}{t}\frac{L}{W} = R_s\frac{L}{W} \tag{2.12}$$

where $R_S = \rho/t$ is the sheet resistance. According to Eq.(2.12), if a conductor sheet has the same length and width, its resistance will have the same value with its sheet resistance. That's the reason for the name "ohms per square". A square sheet with the sheet resistance of 50 Ω/sq has an actual resistance of 50 Ω, regardless of the size of the square.

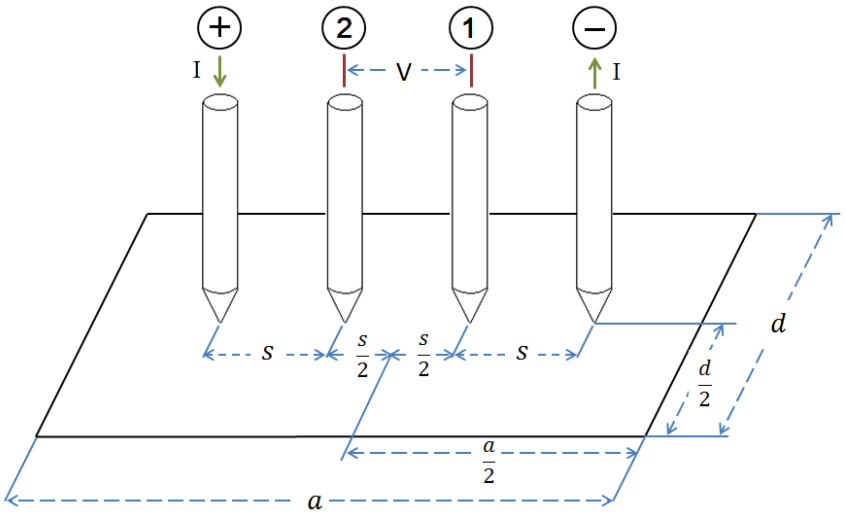

Fig. 2.18 Arrangement of four-point probe on a rectangular sample.

Four-point probe based instruments are used to measure the sheet resistance by passing current through the outside two points of the probes and measuring the voltage across the inner probes as displayed in Fig.2.18. For a rectangular sample with a finite size, the sheet resistance measured with the four-point probe measurement can be calculated as [163],

$$\rho_s = \frac{V}{I}C_f\left(\frac{a}{d},\frac{d}{s}\right) \tag{2.13}$$

where C_f represents the finite-size correction factors. The specific values of C_f for different geometries are displayed in Table 2.1.

Table 2.1 Correction Factor C_f for the Measurement of Sheet Resistivities with the Four-point Probe.

d/s	a/d=1	a/d=2	a/d=3	a/d≥4
1.0			0.9988	0.9994
1.25			1.2467	1.2248
1.5		1.4788	1.4803	1.4803
1.75		1.7196	1.7238	1.7238
2.0		1.9454	1.9475	1.9475
2.5		2.3532	2.3541	2.3541
3.0	2.4575	2.7000	2.7005	2.7005
4.0	3.1137	3.2246	3.2248	3.2248
5.0	3.5098	3.5749	3.5750	3.5750
10.0	4.2200	4.2357	4.2357	4.2357
15.0	4.3882	4.3947	4.3947	4.3947
20.0	4.4516	4.4553	4.4553	4.4553
40.0	4.5120	4.5129	4.5129	4.5129
∞	4.5324	4.5324	4.5324	4.5324

2.3.2 The Bode-Fano criterion

As mentioned in Section 2.1, when the effective impedance of the absorber matches the free space impedance Z_0, the reflection will be minimized and the absorption will be maximized. For a broadband absorber, a perfect match over a wide frequency band is desired. However, there exists a general limit on the bandwidth over which an arbitrarily good impedance match can be obtained in the case of a complex load impedance. It is related to the ratio of reactance to resistance, and to the bandwidth over which the impedance match is desired. This limitation is given by the Bode-Fano criterion [164].

For a lossless network used to match a parallel RC load impedance, the Bode-Fano criterion states that

$$\int_0^\infty ln\frac{1}{|\Gamma(\omega)|}d\omega \leq \frac{\pi}{RC} \tag{2.14}$$

where $\Gamma(\omega)$ is the reflection coefficient seen looking into the arbitrary lossless matching network. Since ln(1) = 0, there is no contribution to this integral over frequencies for which |Γ| = 1, so the maximum mismatch out of the band of interest is desired. If assume this condition, the integral is limited to the bandwidth of interest $\Delta\omega$. Consider the idealized situation shown in Fig. 2.19, where the reflection coefficient is unity outside the band of interest and is Γ_m in the frequency range $\Delta\omega$ [165].

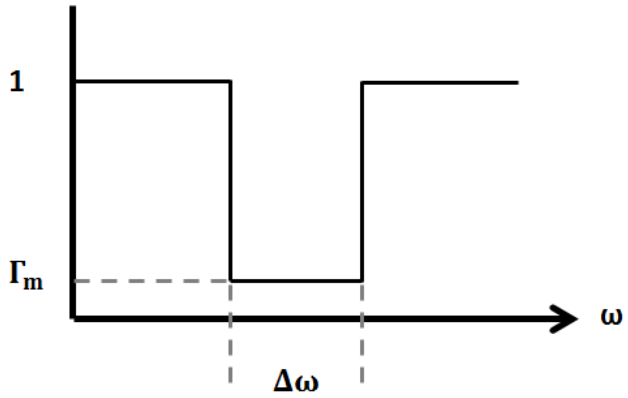

Fig. 2.19 Idealized reflection coefficient response.

For this simplification, the integral becomes

$$\Delta\omega\ ln\frac{1}{\Gamma m} \leq \frac{\pi}{RC} \tag{2.15}$$

Recalling that ln(x) = -ln(1/x) and solving for Γ_m, the result can be given as

$$\Gamma m \geq e^{-\frac{1}{2\Delta fRC}} \tag{2.16}$$

This can be solved for the maximum bandwidth for which a given RC product can be matched to within a given reflection coefficient. There are similar limitations on other forms of complex impedance. A general implication of the Bode-Fano limit is that one should not waste any match out-of-band, and that the best in-band match is obtained with Chebyshev rather than

maximally flat networks [165]. Such results are important because they specify an upper limit of performance and provide a benchmark against which a practical design can be compared.

2.3.3 Equivalent circuit model

Equivalent circuit model approach is widely used in metamaterial absorber design and analysis [166]–[169]. To understand this approach, a simple structure is taken as an example given in Fig. 2.20 (a). When $t = \lambda/4$, this is referred as Salisbury absorber. Its transmission line equivalent circuit is shown in Fig. 2.20 (b), and the input impedance can be calculated as

$$\frac{1}{Zin} = \frac{1}{Rs} + \frac{1}{jZctan\beta t} \tag{2.17}$$

When the thickness $t = \lambda/4$,

$$\frac{1}{Zin} = \frac{1}{Rs} + \frac{1}{\infty} = \frac{1}{Rs} \tag{2.18}$$

Which means, for Salisbury screen, $Z_{in} = R_S$. The reflection coefficient of this absorber is,

$$\Gamma = \frac{Zin - Zo}{Zin + Zo} \tag{2.19}$$

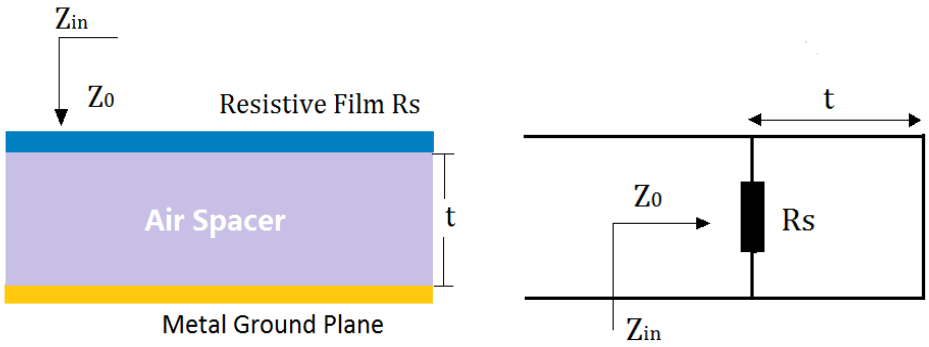

(a) *(b)*

Fig. 2.20 (a) Typical absorber and (b) its transmission line equivalent circuit model.

If $Z_{in} = Z_0$, the reflection $\Gamma = 0$, which means there is no wave reflected from the absorber. The purpose of the absorber design is to find the proper structure and materials to construct the absorber and meet the conditions to obtain as little reflected wave as possible in wide frequency

band and incident wave angles. For Salisbury screen, if the Rs = 377 Ω, then the input impedance of the absorber $Z_{in} = R_S = Z_0$, the screen has perfect absorption when the thickness is $\lambda/4+n\lambda/2$ [170].

To design absorbers with better broadband performances, lower profiles, and wide-angle performances, the resistive frequency selective surface (FSS) based absorbers were designed. The resistive FSS based absorbers usually have periodically patterned resistive films, spacer and ground plane. Fig. 2.21 displays the examples of periodic FSS based structures and their equivalent circuits. The R and L can be created by the FSS patches, while C is induced by the gaps between the patches. The physical meaning of these C and L values of different FSS can be understood using simple electrostatic principles like capacitance of a parallel plate capacitor and inductance of two parallel wires. The inductive and capacitive surfaces can be combined together to produce a desired response [171].

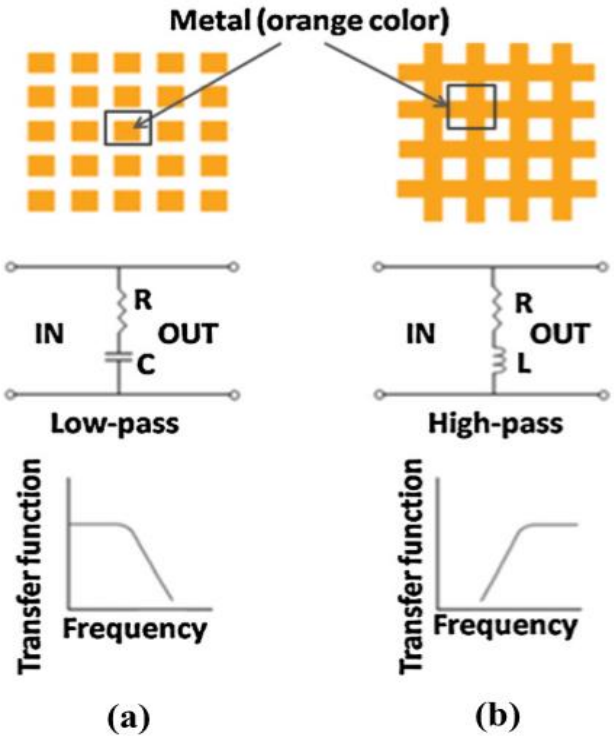

Fig.2.21 Periodic structures comprising of complimentary elements and their corresponding equivalent circuits and frequency responsed. The patch array show a capacitive response, while the slot array presents an inductive response [171].

Fig. 2.22 gives an example of a unit cell of a metamaterial absorber with a broadband absorption. The crisscross and fractal square patch along the electric field direction can be modelled as series RLC circuit (R_f, L_1, and C_1 in Fig. 2.22 (b)). To ensure the symmetry of the FSS, the crisscross arrange along the magnetic field direction. Electric and magnetic coupling occur between the vertical crisscross and the fractal square patch (as L_2 and C_2 in Fig. 2.22 (b)) [172]. The FSS impedance calculated according to the circuit model is

$$Z_f = R_f + \frac{1}{j\omega C_1} + j\omega L_1 + \frac{j\omega L_2}{1-\omega^2 L_2 C_2} \tag{2.20}$$

The impedance of the ground dielectric substrate can be obtained from transmission line method, which is

$$Z_d = \mathrm{j}Z_0\sqrt{\frac{1}{\varepsilon_r}}\tan\left(\frac{2\pi f}{c}\sqrt{\varepsilon_r}d\right) \tag{2.21}$$

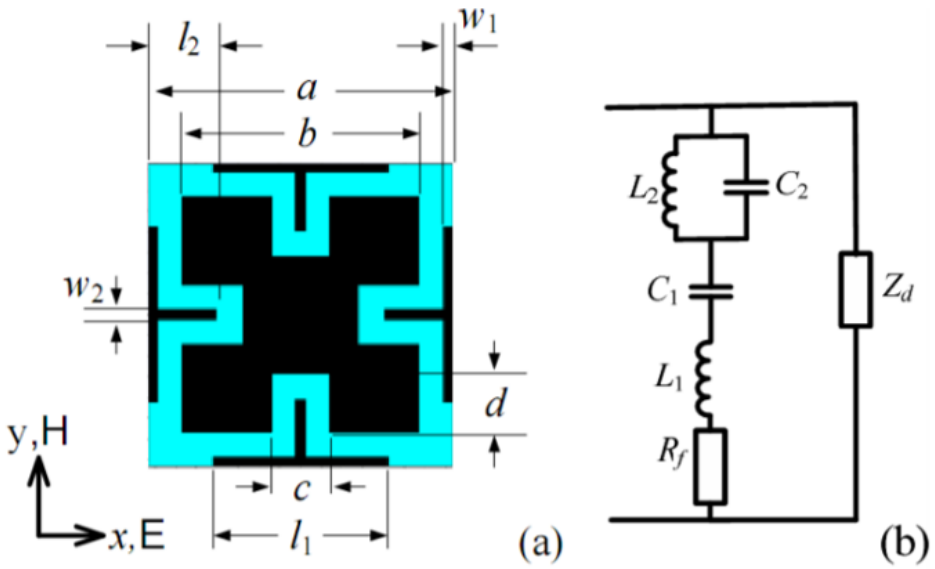

Fig. 2.22. (a) Unit cell of a broadband metamaterial absorber and (b) its equivalent circuit model [172].

With the equivalent circuit and Eq. (2.20) and (2.21), the optimized parameters of the designed absorber can be obtained. With these optimized parameters, the simulated reflectivity of this absorber with thickness of 4 mm can achieve -10dB from 5.27GHz to 18GHz.

2.3.4 Interference theory

In [173], the interference theory was introduced to analyze metamaterial absorbers and elucidate the absorption mechanism. The interference theory states that the two layers of metal structures in metamaterial absorbers are linked only by multiple reflections with negligible near-field interactions or magnetic resonances, and the surface currents with anti-parallel directions are a result of interference and superposition, rather than excitation of a magnetic resonance. The interference theory approach can be explained with a simple and typical metamaterial absorber structure operating at terahertz frequencies, as shown in Fig. 2.23. This absorber structure consists of a cross-resonator array and a ground plane separated by d = 10 μm thick polyimide dielectric spacer [173].

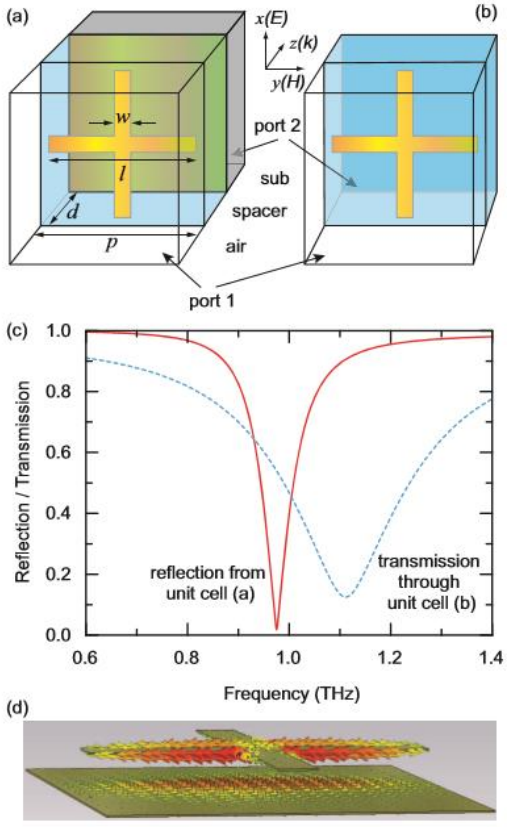

Fig. 2.23. (a) Schematic structure of the metamaterial absorber unit cell, which repeats in the x and y directions. (b) Unit cell used to obtain the reflection and transmission coefficients at the air-spacer interface with the cross-resonator array. (c) The simulated results of $|S_{11}|$ and $|S_{21}|$. (d) Surface anti-parallel currents of the metamaterial absorber at the peak absorption frequency. The current at the cross flows to left direction, while the current at the ground plane flows to right direction [173].

The above model treats the metamaterial absorber as a coupled system, and the possible near-field interactions and magnetic resonance have been taken into account between the cross-resonator array and the ground plane. However, in the interference model, the metamaterial absorber is decoupled into two tuned interfaces, with the cross-resonator array and ground plane located at two sides of the spacer. They are only linked by multiple reflections, while any near-field interaction or magnetic resonance has been neglected. The presence of the metal cross-resonance array can be considered resulting in an impedance-tuned air-spacer interface with dramatically modified complex reflection and transmission coefficients shown in Fig. 2.24. On the other hand, the ground plane functions as a perfect reflector with reflection coefficient -1 [173].

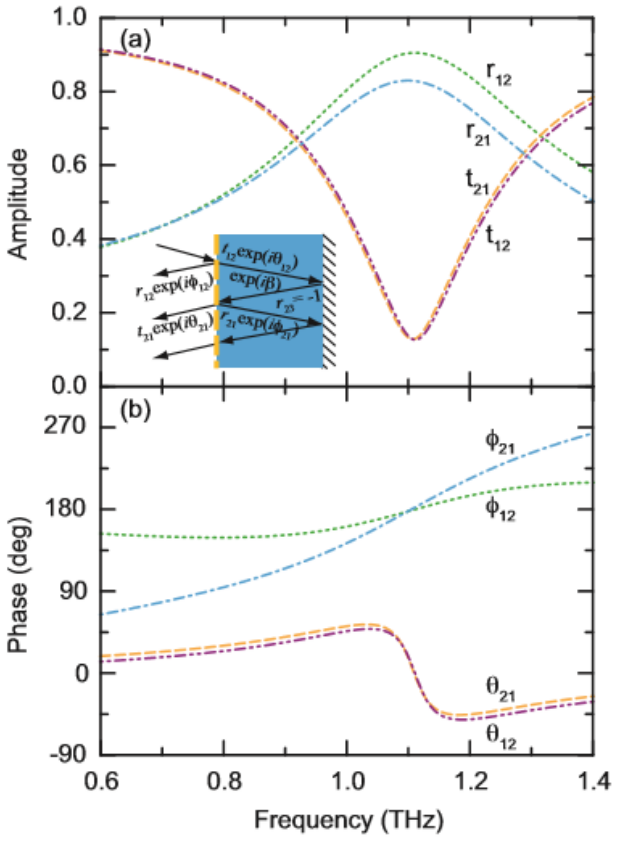

Fig. 2.24. (a) Amplitude and (b) phase of the reflection and transmission coefficients at the air-spacer interface with cross-resonator array, obtained by numerical simulations using the unit cell shown in Fig. 2.23 (b). Inset: Multiple reflections and interference model of metamaterial absorber [173].

As shown in the inset to Fig. 2.24 (a), at the air-spacer interface with cross-resonator array, the incident light is partially reflected back to air with a reflection coefficient $\boldsymbol{r}_{12} = r_{12}e^{i\phi_{12}}$ and partially transmitted into the spacer with a transmission coefficient $\boldsymbol{t}_{12} = t_{12}e^{i\theta_{12}}$. The latter continues to propagate until it reaches the ground plane, with a complex propagation phase $\boldsymbol{\beta} = \beta_r + i\beta_i = \sqrt{\boldsymbol{\varepsilon}_{spacer}}k_0 d$, where k_0 is the free space wavenumber, β_r is the propagation phase, and β_i represents the absorption in the spacer. After the reflection at the ground plane and addition of another propagation phase $\boldsymbol{\beta}$, partial reflection and transmission occur again at the air-spacer interface with cross-resonators with coefficients $\boldsymbol{r}_{21} = r_{21}e^{i\phi_{21}}$ and $\boldsymbol{t}_{21} = t_{21}e^{i\theta_{21}}$. Similar to the light propagation in a stratified media [174], the overall reflection is then the superposition of the multiple reflections,

$$\boldsymbol{r} = \boldsymbol{r}_{12} - \frac{\boldsymbol{t}_{12}\boldsymbol{t}_{21}e^{i2\boldsymbol{\beta}}}{1 + \boldsymbol{r}_{21}e^{i2\boldsymbol{\beta}}} \tag{2.22}$$

where the first term is the reflection directly from the cross-resonator array, and the second term, including the "−" sign, is the reflection resulting from superposition of the multiple reflections between the cross-resonator array and ground plane. The absorption can be calculated through $A(\omega) = 1 - |\boldsymbol{r}(\omega)|^2$ since the transmission is zero due to the presence of the ground plane. With the reflection and transmission coefficients simulated and shown in Fig. 2.24, the absorption can be calculated in the decoupled metamaterial absorber system and the calculated results are in excellent agreement with the simulated results [173]. The absorption has a peak at 1 THz when the spacer thickness is about 10 μm. The explanation of the mechanism of this absorber is as follows. The multiple reflection (the second term in Eq.(2.22)) in the metamaterial absorber constructively interfere as evidenced by the fact that near 1 THz the phase change of a round trip is $2\beta_r + \phi_{21} + 180^0 \approx 360^0$. The superposition of the multiple reflections then destructively interferes with the direct reflection (the first term in equation Eq.(2.22)) from the air-spacer interface with cross-resonators. With an optimized spacer thickness and in a narrow frequency range, these two terms completely cancel each other and results in zero reflection [173].

According to the interference theory, it is not required in a metamaterial absorber to have simultaneous electric and magnetic responses. It is the destructive interference that causes the high absorption.

2.3.5 Wide-angle impedance matching

Wide-angle impedance matching (WAIM) is a method used in antenna array design to reduce the variation of reflection coefficient with scan angle and polarization [175, 176]. The wide-angle impedance matching layer can also be used to minimize the impedance discontinuity between the absorber and free space and improve the performance in terms of the angle of incidence [177].

A thin dielectric sheet has wave-reflection properties useful in wide-angle impedance matching. The admittance of such a sheet is purely susceptive and, thus can be regarded as a shunt capacitive susceptance in space. The variation of the effective value of this susceptance with incident angle θ and polarization can be used for compensating the corresponding variations of reflection at a phased array [175].

Generally, the effective susceptance $B(\theta)$ varies oppositely with increasing incident angle in the *E* and *H* plane. As the incident angle increases, the effective susceptance increases in *H* plane, because *E* is parallel to the sheet and the effective thickness in the wave direction increased with angle. On the other hand, it decreases in *E* plane, because *E* departs from parallel to the sheet and the field is influenced thereby in a lesser degree [178].

With the effective susceptance at broadside ($B(0)$ for $\theta = 0$) as a reference, the variation of the effective susceptance with incident angle θ is expressed for *H* and *E* planes as [175],

$$\frac{B(\theta)}{B(0)} = \frac{1}{\cos\theta} \quad (H\ plane) \tag{2.23}$$

$$\frac{B(\theta)}{B(0)} = \cos\theta - \frac{sin^2\theta}{k_c \cos\theta} \quad (E\ plane) \tag{2.24}$$

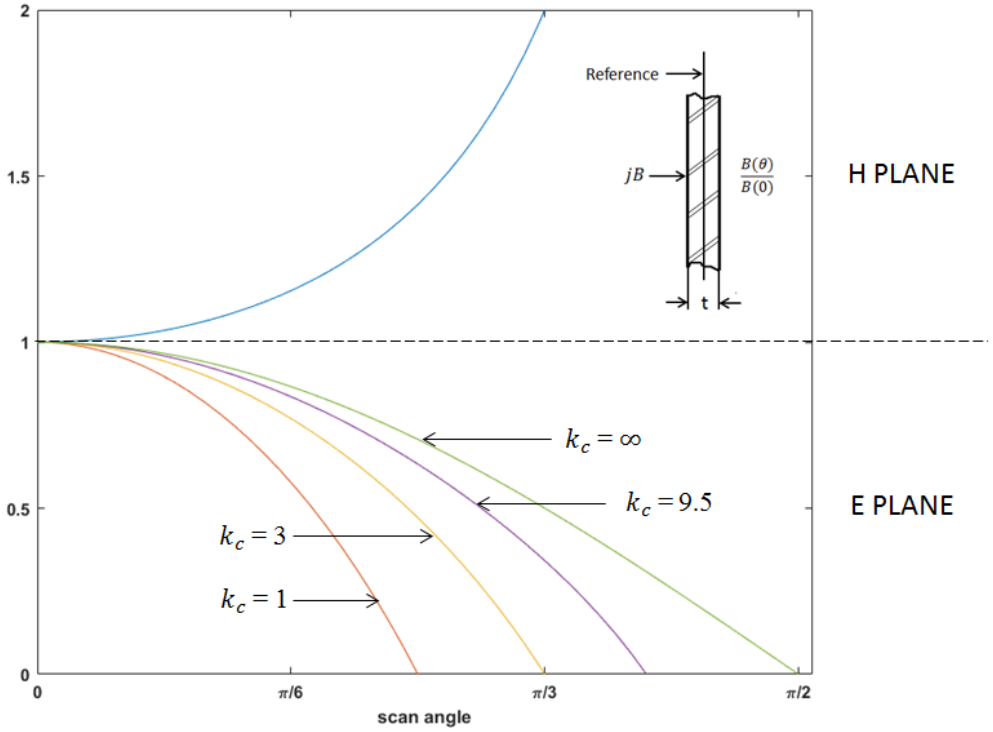

Fig. 2.25 Normalized susceptance of thin dielectric sheet.

With increasing of dielectric constant k_c, the second part of equation (2.24) decreases and these ratios approach reciprocal relationship, as illustrated in Fig.2.25. Within the thin-sheet approximation, any variation between 0 and 60 ° can be realized if within the following value [175],

$$\left|\frac{B(60°) - B(0)}{G_0}\right| < \frac{\pi}{4}\frac{k_c - 1}{\sqrt{k_c}} \tag{2.25}$$

where G_0 represents the wave conductance of free space.

2.3.6 Eddy current

What happens when a time-varying electric current passes through a simple loop of wire held near a conductor such as a metal plate? As shown in Fig. 2.26, the time-varying current flowing in the wire loop has the effect of inducing an electric current which flows in the metal plate. The current in the plate in some sense mirrors the applied current flowing in the wire loop, but flows

in the opposite direction. These induced currents are known as eddy currents, which in practice always flow in closed paths [179].

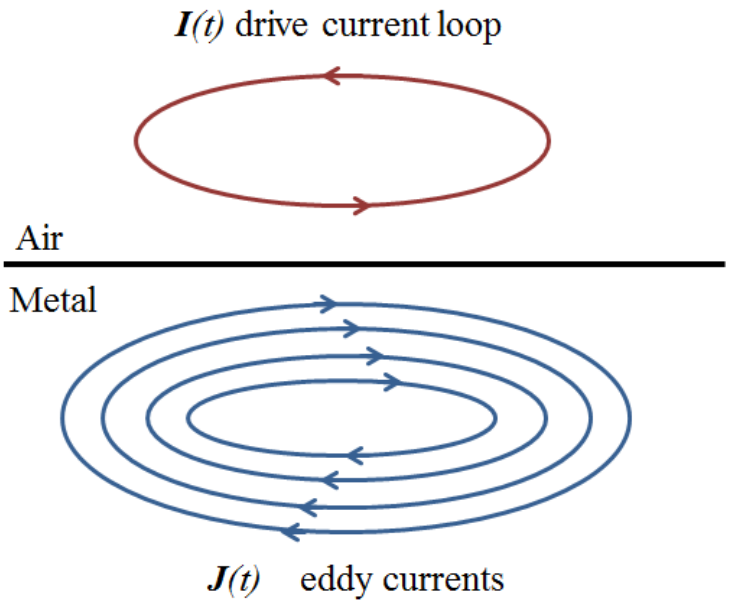

Fig. 2.26 Eddy currents induced in a metal part by a time-varying current loop in air.

The inducing of eddy currents relies on the phenomenon of electromagnetic induction, which is first observed experimentally by Faraday, who hypothesized the existence of the electric and magnetic fields in order to explain the observations. The applied time-varying current means that a magnetic field is produced in the vicinity of the current loop. This time-varying magnetic field then couples with the nearby metal and induces electric current in the metal. The eddy currents that flow in the metal are themselves time-varying and produce their own associated magnetic field [179].

2.4 AMC Structures for RCS Reduction

The artificial magnetic conductors (AMC) could modify the reflect wave by altering their phase and amplitude [180]. The metasurface based on combination of AMC and PEC cells was proposed by Paguay *et al.* in 2007 [181]. The structures were in a chessboard like configuration. Its principle of operation was based on scattering cancellation. The reflected waves from AMC cells and PEC cells had a phase difference of 180 °, which resulted in the destructive interference

and a null in the specular direction. The reflect energy was mainly scattered into four diagonal direction, leading to dramatically reduce the radar cross section (RCS) in the normal incident angel [181]. However, the operation frequency of this design was very limited. In 2009, a design of radar absorbing material based on a combination of two kinds of AMC units was proposed and the bandwidth of RCS reduction was broadened remarkably [182]. After that, different designs of dual AMCs were investigated to provide broadband RCS reduction [183]–[191]. In previously proposed works, the phase difference was obtained by either combining two AMCs with different size [183]–[186], or using different shapes in two types of AMC structures [187]–[189].

A guideline of phase difference between dual AMCs was proposed in the work [191]. As illustrated in Fig. 2.27 (a), the proposed chessboard surface consists of four elements: two AMC1 with 4×4 square patches and two AMC2 with 4×4 circular patches. This surface can be treated as a planar array with a progressive phase shift of around 180 °[191].

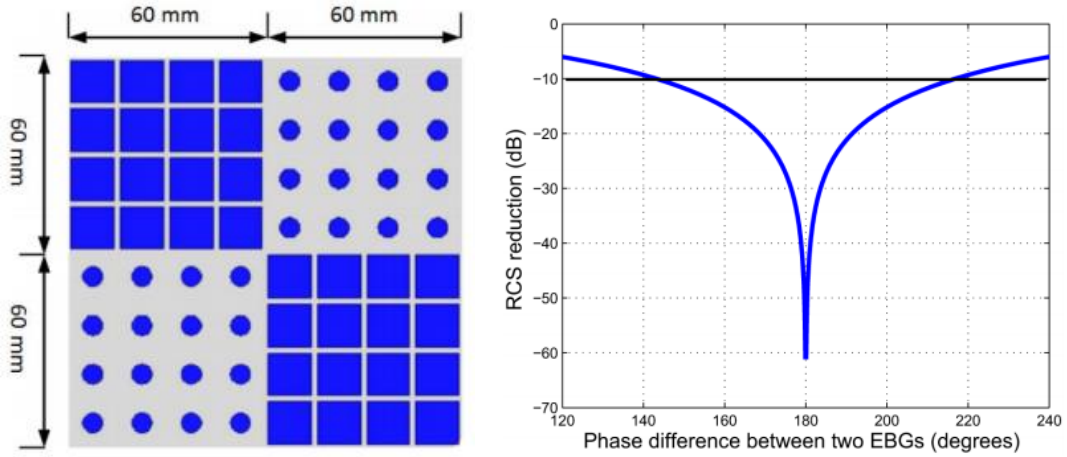

(a) *(b)*

Fig. 2.27. (a) One period of a square checkerboard surface that combines AMC1 and AMC2 structures alternately with their 4×4 square patches and 4×4 circular patches. (b) Approximate RCS reduction completed with Eq.(2.30) [191].

For this plane, the array factor can be represented by

$$\mathrm{AF} = I_0 \cdot \sum_{m=1}^{M} e^{j(m-1)(kd_x \sin\theta \cos\phi + \beta_x)} \cdot \sum_{n=1}^{N} e^{j(n-1)(kd_y \sin\theta \sin\phi + \beta_y)} \qquad (2.26)$$

where β_x and β_y are the progressive phase shifts between the elements in the x and y directions, respectively. The distances d_x and d_y are the spacing between the elements along x and y axis, respectively, while M and N are the number of elements in x and y directions [191].

The principal maximum, directed along ϕ_0 and θ_0 can be found using (2.27) and (2.28) [192],

$$\tan \phi_0 = \frac{\beta_y d_x}{\beta_x d_y} \tag{2.27}$$

$$\sin^2 \theta_0 = (\frac{\beta_x}{k d_x})^2 + (\frac{\beta_y}{k d_y})^2 \tag{2.28}$$

The RCS reduction of a scattering surface, compared to that of a PEC, can be represented by

$$\text{RCS reduction} = 10 \log \left[\frac{\lim\limits_{r\to\infty} \left[4\pi r^2 \frac{|E^s|^2}{|E^i|^2} \right]}{\lim\limits_{r\to\infty} [4\pi r^2 (1)^2]} \right] = 10 \log \left[\frac{|E^s|^2}{|E^i|^2} \right] \tag{2.29}$$

which for a dual AMC chessboard surface can be approximately by [191]

$$\text{RCS reduction} = 10 \log \left[\frac{A_1 e^{jP_1} + A_2 e^{jP_2}}{2} \right]^2 \tag{2.30}$$

where A_1 and A_2 are the reflection coefficient amplitudes of the two AMC structures, and P_1 and P_2 are their reflection phases. In (2.29), the ratio of the scattered field and the incident field is equal to the reflection coefficient of the surface. Since the chessboard surface consists of two AMC surfaces, each of the AMC surfaces occupies exactly half of the area of the entire chessboard surface. Thus, the reflection coefficient of the entire surface can be expressed by the average reflection coefficient of the two AMC structures. Therefore, the RCS reduction can be approximated by (2.30), which does not include edge effects, but provides a good guideline for RCS reduction of a dual AMC surface compared to that of a PEC [191].

By applying (2.30), the boresight RCS reduction of a chessboard surface versus the phase difference of the two AMC structures is displayed in Fig. 2.27 (b). A 10 dB RCS reduction occurs,

in the ideal case of an infinite chessboard surface, with $180° \pm 37°$ phase difference between two AMC structures [191].

2.5 Calling CST from MATLAB

CST Studio Suite is a computational electromagnetic (EM) tool developed by Dassault Systemes Simulia. It is a high-performance 3D EM analysis software package for designing, analyzing and optimizing EM components and systems [193]. Common subjects of EM analysis include the performance and efficiency of antennas, sensors, absorbers and filters. In CST Studio Suite, EM field solvers for applications across the EM spectrum are contained within a single user interface and can be coupled to perform hybrid simulations to analyze whole systems made up of multiple components [193].

MATLAB(an abbreviation of 'matrix laboratory'), which combines a desktop environment tuned for iterative analysis and design processes with a programming language that expresses matrix and array mathematics directly [194], is a proprietary multi-paradigm programming language and numeric computing environment developed by MathWorks.

An analysis of the available CST and MATLAB help showed that both programs support the use of the ActiveX framework [195]. ActiveX, which is a technology introduced in 1996 by Microsoft as a development of Component Object Model (COM) [196] and Object Linking and Embedding (OLE) technologies, is a framework for defining software components usable from programs written in different programming languages. The description of CST Studio indicates that any of its components can act as a managed OLE server, while OLE can be used to link and embed objects into other documents and objects developed by Microsoft [195]. Therefore, the Microsoft Windows and OLE technology can be a solution of calling CST from MATLAB.

There are a few basic functions to work with the ActiveX interface [197]. Function *actxserver* can create a local or remote server, while function *invoke* can call a method for an ActiveX object. In another word, the function *actxserver* can be used to initialize and open a program acting as a managed one, while *invoke* can be used to access certain sections of the managed program [197].

For example, the command cst = actxserver('CSTStudio.Application') binds the 'CSTStudio.Application' OLE-managed object to the 'cst' variable in MATLAB. To create a new empty project file in CST, the command mws = invoke(cst, 'NewMWS') can be used. Through the ActiveX interface, all the commands that need to be executed in CST, instead of being contained in a VBA .bas file are contained in a MATLAB .m file, which offers complete control of CST MWS from within MATLAB [198]. With this technology, operations such as building models, investigating parameters, analyzing simulation results, and etc. are all accessible in MATLAB.

2.6 Genetic Algorithm

Genetic algorithms are utilized to solve optimization problems, which are problems of finding optimal solutions. Optimization problems can be found in many domains, from natural sciences to math and computer science, from engineering to social and daily life [199]. Whenever the aim is to maximize the profit and scores, or to minimize the cost and deviation, the essence of the optimization problems is to find the optimal solutions which have a better quality than others.

The design of broadband metamaterial absorbers is exactly a general optimization problem. The broad effective absorption bandwidth can be affected by many factors, such as the geometry parameters of unit cell model, the sheet resistance of resistive patterns, and the dielectric constant of substrate. Seeking for the widest effective absorption bandwidth among such plenty of influence factors can be a tedious task. With genetic algorithm, this tedious task can be processed by machines. If modelled in an appropriate kind of way, genetic algorithm is able to solve most optimization problems, including the design of broadband metamaterial absorbers.

Genetic algorithm is inspired by the biological concept of evolution [200] which explains the biological development of species with mating selection and survival of the fittest. Firstly, the initialized solutions are generated randomly or manually at the beginning of the evolutionary process. Each solution represents a potential candidate for an optimum of the optimization problem. After initialization, two solutions in the initialized generation are picked out as 'parents'

to recombine and produce a 'child' during the crossover processing. The crossover operator allows the combination of the genetic material of two or more solutions [201]. From a biological perspective, most species have two parents who combine their genetic material and inherit it to their offspring. Crossover operators in genetic algorithms implement a mechanism that mixes the genetic material of parents [199]. A famous operator for bit string representation is n-point crossover, as illustrated by Fig. 2.28. Two 'parents' are divided into parts at n positions and alternately assembled to provide a 'child'.

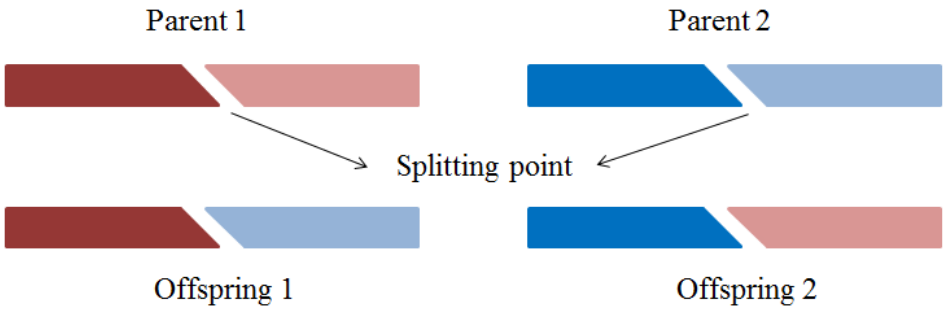

Fig. 2.28 Example of one-point crossover (here the arbitrary point is assumed to locate in the middle).

The produced 'child' is then mutated to give a new solution. Mutation is based on random changes. Mutation operators change a solution by disturbing it with a mutation rate which represents the strength of the disturbance.

In the fitness computation step, the fitness function measures the quality of the solutions. The better solutions generated are selected through fitness operator for the next generation. In the case of designing a broadband metamaterial absorber, the fitness operator is expected to give bigger weights to solutions which provide broader effective absorption bandwidth.

Finally, the evolutionary cycle examines whether the termination condition has been met or not. If there is a 'child' in the new generation satisfies the termination condition, the processing ends up being a success, otherwise the evolutionary cycle continues and the new generation (produced 'children') replaces the initialized solutions to become new 'parents'.

The Algorithm in Table 2.2 shows the pseudocode of the basic genetic algorithm.

Table 2.2 The Pseudocode of the Basic Genetic Algorithm

Algorithm 1: Basic Genetic Algorithm
1: initialize population as original generation
2: **repeat**
3: **repeat**
4: crossover
5: mutation
6: fitness computation
7: **until** population complete
8: select and produce next generation
9: **until** termination condition

2.7 Chapter Summary

This chapter deals with the literature review of metamaterial absorbers and graphene, with a focus on the development from conventional electromagnetic absorbers to metamaterial absorbers, and along with several specific examples proposed by previous papers. The review of graphene concerns its geometry, property, synthesis, and eventually the graphene based metamaterial absorbers.

The chapter then details several important concepts and absorber related theory, which would be used or mentioned in the following chapters. The principle of AMC based radar absorbers is given in detail. The method to call CST from MATLAB is explained briefly, together with the abbreviated introduction of genetic algorithm.

Chapter 3: Multi-layer Broadband Printed Graphene Microwave Absorbers: Multi-layer Structures with Equivalent Circuit Model

3.1 Triple-layer Polarization-independent Broadband Microwave Absorber

3.1.1 Design and performances

This section presents the design and numerical simulation results of a broadband and polarization-independent microwave absorber composed of three layers of metasurfaces with different patterns and sheet resistances. The numerical simulations of the absorber are performed through modelling the unit cell of designed absorber as an infinite periodic structure by applying periodic boundary condition in x and y directions with the full-wave software CST Microwave Studio 2016.

Fig. 3.1 shows the schematic of the unit cell, which is composed of three layers of resistive surfaces, printed on three layers of substrates, respectively. A perfect electric conductor (PEC) is placed on the back side to block the transmission. The top dielectric substrate is modelled as open-cell polyethylene foam with relative permittivity (ε_r) of 1.05 and loss tangent ($\tan\delta$) of 0.02. The middle and bottom dielectric substrates are silicone material with relative permittivity of 2.9. The top and bottom resistive patches are square patches with same dimensions, while the middle resistive patches are circular rings. The sheet resistances of three layers of surfaces, from top to bottom, are 400 Ω/sq, 65 Ω/sq, and 110 Ω/sq, respectively. The optimized geometrical parameters of unit cell are: h_t = h_m = 2 mm, h_b = 1 mm, p = 7.5 mm, w = 7 mm, r_{in} = 2.4 mm, r_{out} = 3.5 mm.

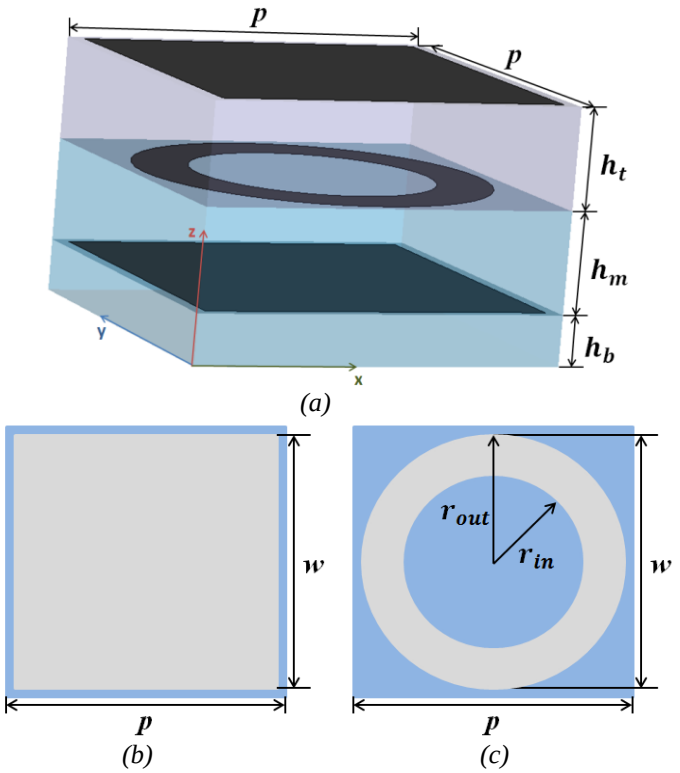

Fig. 3.1 Unit cell geometry of proposed absorber with (a) perspective view, (b) top-layer and bottom-layer pattern, (c) middle-layer pattern.

The absorptivity of the proposed absorber can be obtained through the formula $1 - T(\omega) - R(\omega)$, where $T(\omega)$ is defined as the transmission part and $R(\omega)$ is the reflection part. Since there is a perfect electric conductor (PEC) on the back side of the proposed absorber, the transmission is blocked. Therefore, the absorptivity can be calculated through $A(\omega) = 1 - R(\omega) = 1 - |S_{11}|^2$, where S_{11} is the reflection coefficient.

The absorption performance of the absorber is displayed in Fig. 3.2. The effective absorption (with over 90% absorptivity) is achieved from 6 GHz to 50 GHz, with a relative absorption bandwidth of 157%. Due to its symmetric structure, the absorber has the property of polarization-insensitive, which is illustrated in Fig. 3.2. The absorption performance keeps consistent as the polarization angle changes from 0 °to 90 °with a step of 30 °.

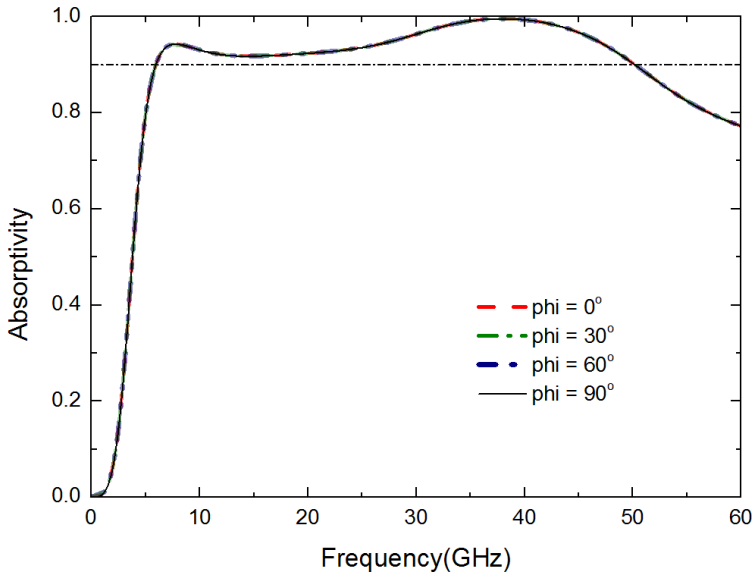

Fig. 3.2 Absorptivity characterisitics with various polarisation angles under normal incidence.

The comparison of the effective absorptivity bandwidth and thickness between this design and some previously proposed absorbers is shown in Table 3.1, in which λ represents for the wavelength at the lowest operation frequency under normal incidence in free space. The comparison in Table 3.1 indicates the advantage of ultra-wide bandwidth of this triple-layer absorber.

Table 3.1 Comparison of This Work and Some Previously Presented Multi-layer Absorbers.

Reference	Effective absorption bandwidth (GHz)	Relative bandwidth (%)	Thickness (mm)	Unit size (mm)
[202]	5.6 - 16.8	100	6.13 (0.114 λ)	30 (0.56 λ)
[203]	1.4 - 6	124	2.44 (0.11 λ)	52 (0.243 λ)
[204]	3.7 - 17.5	130	11.5 (0.14 λ)	5 (0.062 λ)
[205]	10 - 70	150	4.5 (0.15 λ)	6.4(0.213 λ)
[206]	4.96 - 18.22	114	4.6 (0.076 λ)	13 (0.215 λ)
This work	6 - 50	157	5 (0.1 λ)	7.5 (0.15 λ)

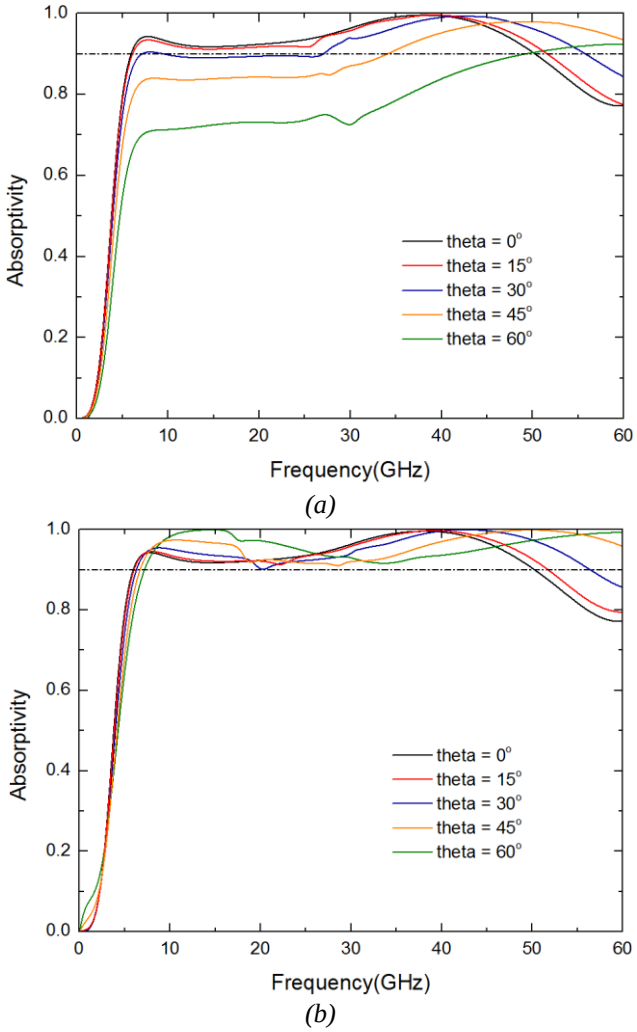

Fig. 3.3 Absorption performances under various incident angles for (a) TE and (b) TM mode.

In order to investigate the operation performance stability under various incident angles, the absorptivity results with different oblique incident angles for transverse electric (TE) wave and transverse magnetic (TM) wave are simulated and displayed in Fig. 3.3 (a) and Fig. 3.3 (b), respectively. It is worthy to point out that this triple-layer absorber has an ultra-wide-angle absorption property for TM mode. As the incident angle increases from 0 ° to 60 ° with the step of 15 °, the lower absorption frequency bound moves to higher frequency gently, while the upper absorption frequency bound changes much faster to higher frequency, leading to a wider effective absorption bandwidth. On the other hand, the absorption performance for TE wave mode is more sensitive to the incident angle. When the incident angle increases to 30 °, the absorptivity keeps

around 90% grudgingly. As the incident angle increases continuously after 30°, the absorptivity decreases dramatically.

3.1.2 Equivalent circuit model

Based on the introduction and elucidation of equivalent circuit model method in basic theory section earlier, periodic structures comprising of tiled patches can be equivalent to series resistor inductor capacitor (RLC) circuits, with *R* and *L* created by the periodic patches, while *C* induced by the gaps between patches [171]. Fig. 3.4 displays the equivalent circuit model of the triple-layer microwave absorber. The three layers of periodic resistive surfaces are equivalent to three RLC circuits in parallel, while the dielectric structures are modelled as transmission lines connected to RLC circuits.

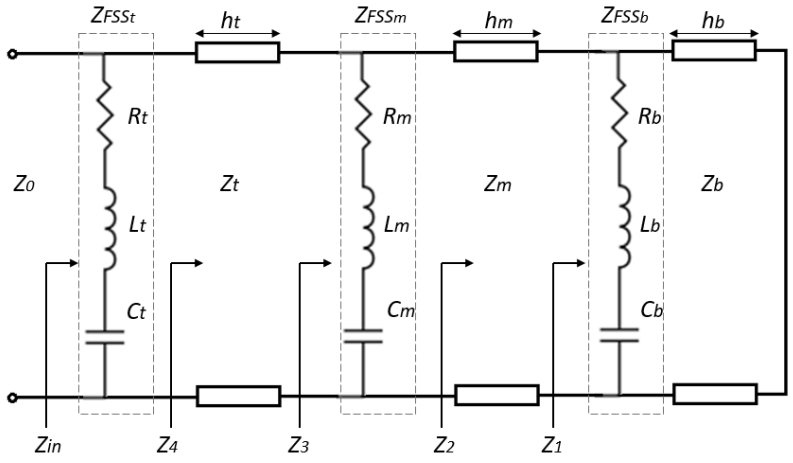

Fig. 3.4 Equivalent circuit model of the proposed absorber.

In Fig. 3.4, Z_0 is the free space impedance with value of 377 Ω, while Z_{in} is the input impedance of the proposed absorber; Z_t, Z_m, and Z_b represent the equivalent impedance of three layers of dielectric substrute from top to bottom; h_t, h_m and h_b are the thickness of dielectric substrates from top to bottom, respectively. For the three RLC circuits in parallel, the *R* and *L* are supposed to be provided by the resistive patterns on each layer of periodic resistive surfaces, and the *C* is induced by the gaps between the periodic patterns. According to transmission line theory, Z_{in} can be described as:

$$Z_{in} = Z_{FSS_t} || Z_4 \tag{3.1}$$

$$Z_4 = Z_t \frac{Z_3 + jZ_t \tan(\frac{2\pi f}{c}\sqrt{\varepsilon_{r_t}} h_t)}{Z_t + jZ_3 \tan(\frac{2\pi f}{c}\sqrt{\varepsilon_{r_t}} h_t)} \tag{3.2}$$

in which $Z_t = Z_0/\sqrt{\varepsilon_{r_t}}$

$$Z_3 = Z_{FSS_m} || Z_2 \tag{3.3}$$

$$Z_2 = Z_m \frac{Z_1 + jZ_m \tan(\frac{2\pi f}{c}\sqrt{\varepsilon_{r_m}} h_m)}{Z_m + jZ_1 \tan(\frac{2\pi f}{c}\sqrt{\varepsilon_{r_m}} h_m)} \tag{3.4}$$

in which $Z_m = Z_0/\sqrt{\varepsilon_{r_m}}$

$$Z_1 = Z_{FSS_b} || Z_b \tag{3.5}$$

$$Z_b = j\frac{Z_0}{\sqrt{\varepsilon_{r_b}}} \tan(\frac{2\pi f}{c}\sqrt{\varepsilon_{r_b}} h_b) \tag{3.6}$$

$$Z_{FSS_k} = R_k + j\omega L_k - \frac{j}{\omega C_k}, \quad k = t, m, b \tag{3.7}$$

where ε_{r_t}, ε_{r_m} and ε_{r_b} are the relative permittivity of dielectric substrates from top to bottom, respectively.

After the input impedance Z_{in} is calculated from (3.1)–(3.7), the reflection coefficient can be obtained through

$$\Gamma = \frac{Z_{in} - Z_0}{Z_{in} + Z_0} \tag{3.8}$$

When the input impedance matches the free space impedance, the reflection coefficient becomes zero. In order to broaden the operation bandwidth of proposed absorber, the matching between input impedance and free space impedance should be achieved through a broad frequency range. The software Advanced Design System (ADS) and MATLAB are used to evaluate and

optimize the values of equivalent RLC circuits. The established values of lumped elements are shown in Table 3.2.

Table 3.2 Values of Equivalent Circuit Elements.

Parameter	Value	Parameter	Value
R_t	480 Ω	L_b	0.08 *nH*
R_m	330 Ω	C_t	0.105 *pF*
R_b	160 Ω	C_m	0.08 *pF*
L_t	0.3 *nH*	C_b	0.26 *pF*
L_m	1.55 *nH*		

The comparison between the reflection coefficients obtained from CST full-wave simulation and the equivalent circuit model analysis is shown in Fig. 3.5. The reflection coefficient from the equivalent circuit model analysis is under -10 dB from 6 GHz to 50 GHz. At the two resonant frequencies of 7.8 GHz and 37.8 GHz, the reflection coefficients are about -12.3dB and -23.6dB, respectively. The simulation and equivalent circuit model analysis results are in almost perfect agreement, verifying the precision of the equivalent circuit model.

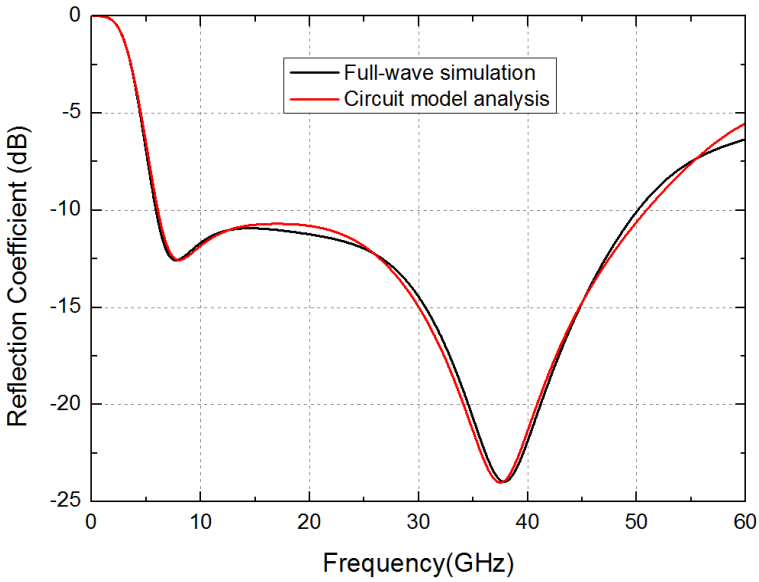

Fig. 3.5 Comparison of reflection coefficients obtained from equivalent circuit model analysis (red line) and full-wave simulation (black line).

3.2 Ultra-wideband Radar Absorber Operating in the S, C, X and Ku Band

3.2.1 Design and performances

Although the effective absorption bandwidth of the triple-layer microwave absorber introduced in Section 3.1 covers a great frequency range from 6 GHz to 50 GHz, corresponding to half of the C band (6–8 GHz), X band (8–12 GHz), Ku band (12–18 GHz), K band (18–27 GHz) and Ka band (27–40 GHz) of the microwave band of the electromagnetic spectrum, there are still the S band (2–4 GHz) and the other half of C band (4–6 GHz) which cannot be covered by the operation frequency band of the absorber. Additionally, the 10 cm radar short-band ranges roughly from 1.55 to 5.2 GHz, which is also cannot be covered by the triple-layer microwave absorber.

The S band is used by plenty of devices and applications, such as the air surveillance radar, weather radar, and communications satellites, especially those used by NASA to communicate with the Space Shuttle and the International Space Station. Besides, the S band contains the 2.4–2.483 GHz ISM band which is widely used for low power unlicensed microwave devices in our daily life such as wireless networking, electronics using Bluetooth, keyless vehicle locks, microwave ovens and so on. These widely used devices in the everyday life may have electromagnetic interference among each other and cause harmful EM wave pollution. In this section, an ultra-wideband radar absorber operating in the S, C, X and Ku band is designed to effectively reduce the electromagnetic interference and prevent harmful EM wave pollution.

The schematic of the unit cell performed with the full-wave software CST Microwave Studio 2016 is displayed in Fig. 3.6. The unit cell of proposed absorber is modelled as an infinite periodic structure by independently applying periodic boundary condition in X and Y directions, and Floquet boundary condition in Z direction.

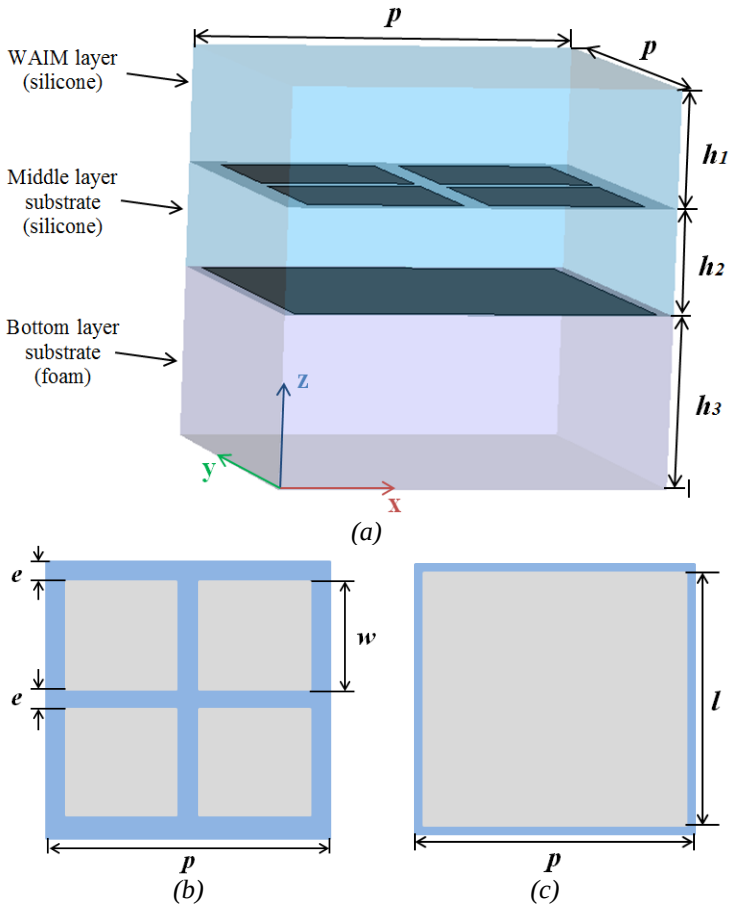

Fig. 3.6 Unit cell geometry of proposed absorber with (a) perspective view, (b) middle layer resistive pattern, and (c) bottom layer resistive pattern.

As shown in Fig. 3.6, the unit cell is composed of two layers of graphene surfaces printed on two layers of substrates. Comparing with triple-layer absorber, the fabrication complexity of this absorber is reduced. To design an absorber which operates at lower frequencies while keep the relative frequency bandwidth as wide as the one provided by triple-layer absorber, a wide-angle impedance matching (WAIM) layer is added at the top of the designed structure. A perfect electric conductor (PEC) is assumed to be the metal ground plane and block the transmission. The bottom dielectric substrate of 6.5 mm thickness is chosen to be open-cell polyethylene foam with relative permittivity (ε_r) of 1.05 and loss tangent ($\tan\delta$) of 0.02. The middle layer dielectric substrate and the WAIM layer are modelled as silicone material with relative permittivity of 2.9. The optimized geometrical parameters of unit cell are: h_1 = 4.5 mm, h_2 = 4 mm, h_3 =6.5 mm, p =

15 mm, w = 6 mm, e = 1 mm, l = 14 mm. The sheet resistances of two layers of resistive surfaces, from middle layer to bottom layer, are 400 Ω/sq and 150 Ω/sq, respectively.

Fig. 3.7 displays the numerically simulated absorption performance of the absorber. The bandwidth of effective absorption (over 90% absorptivity) is from 2.2 GHz to 18.4 GHz, covering almost the whole S-, C-, X-, and Ku-band with relative absorption bandwidth remains 157%. The total thickness of the proposed absorber is 15 mm, which corresponds to 0.11λ at the lowest operating frequency. Due to the symmetric structure of the design, the absorber has polarization-independent property.

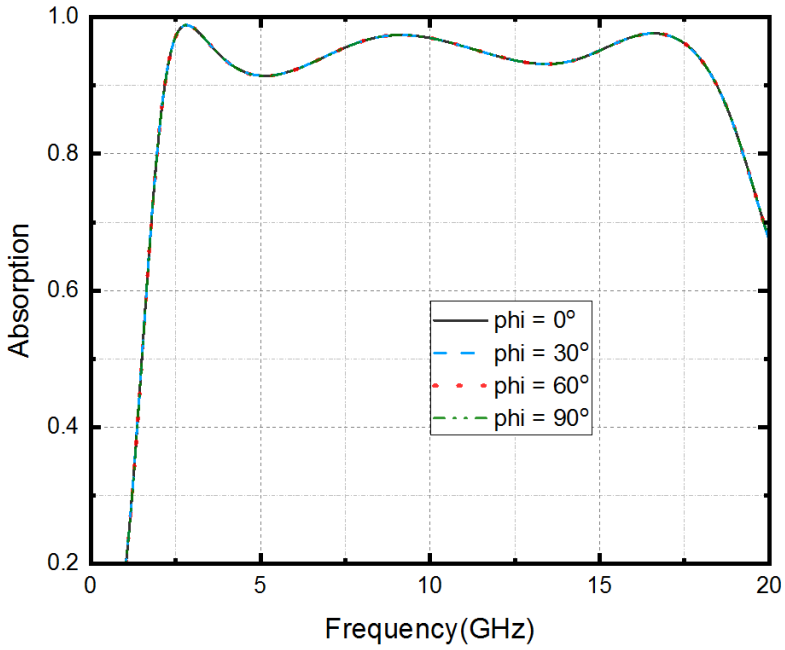

Fig. 3.7 Absorption performance with various polarisation angles under normal incidence.

3.2.2 Equivalent circuit model

The equivalent circuit model of the proposed absorber is displayed in Fig. 3.8. The two layers of periodic resistive surfaces are equivalent to two series resistor inductor capacitor (RLC) circuits in parallel, with R and L created by the periodic resistive patches, while C is due to the gaps between patches. The dielectric structures and the WAIM layer are modelled as transmission lines.

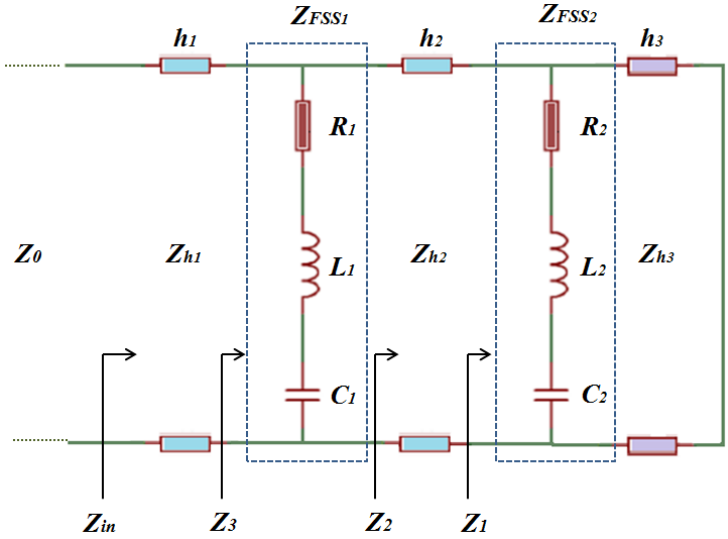

Fig. 3.8 Equivalent circuit model of the proposed absorber.

With the aforementioned method, Z_{in} can be described by the following equation:

$$Z_{in} = Z_{h_1}\frac{Z_3 + jZ_{h_1}\tan(\frac{2\pi f}{c}\sqrt{\varepsilon_{r_s}}h_1)}{Z_{h_1} + jZ_3\tan(\frac{2\pi f}{c}\sqrt{\varepsilon_{r_s}}h_1)} \tag{3.9}$$

$$Z_3 = Z_{FSS_1}||Z_2 \tag{3.10}$$

$$Z_2 = Z_{h_2}\frac{Z_1 + jZ_{h_2}\tan(\frac{2\pi f}{c}\sqrt{\varepsilon_{r_s}}h_2)}{Z_{h_2} + jZ_1\tan(\frac{2\pi f}{c}\sqrt{\varepsilon_{r_s}}h_2)} \tag{3.11}$$

$$Z_1 = Z_{FSS_2}||Z_{h_3} \tag{3.12}$$

$$Z_{h_3} = j\frac{Z_0}{\sqrt{\varepsilon_{r_f}}}\tan(\frac{2\pi f}{c}\sqrt{\varepsilon_{r_f}}h_3) \tag{3.13}$$

$$Z_{FSS_k} = R_k + j\omega L_k - \frac{j}{\omega C_k},\ k = 1,2 \tag{3.14}$$

where h_1, h_2 and h_3 are the thickness of WAIM layer and two dielectric substrates from top to bottom, respectively. ε_{r_s} and ε_{r_f} are the relative permittivity of silicone and foam substrates, respectively. Z_0 represents the free space impedance with value of 377 Ω, while Z_{h_1} and Z_{h_2} in (3.9) and (3.11) can be obtained through calculating $Z_0/\sqrt{\varepsilon_{r_s}}$.

In order to match the input impedance with the free space impedance through a broad radar frequency band, the values of equivalent RLC circuits are evaluated and optimized using Advanced Design System (ADS) and MATLAB. The derived values of lumped elements are shown in Table 3.3.

Table 3.3 Derived Values of Equivalent Circuit Elements.

Parameter	Value	Parameter	Value
R_1	680 Ω	R_2	185 Ω
L_1	1.05 nH	L_2	0.15 nH
C_1	0.068 pF	C_2	0.35 pF

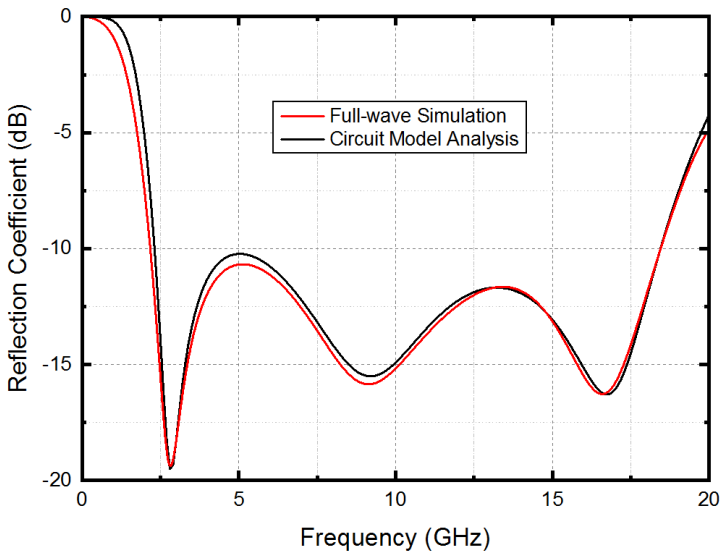

Fig. 3.9 Comparison of reflection coefficients obtained from equivalent circuit model analysis (red line) and full-wave simulation (black line).

The red line in Fig. 3.9 displays the reflection coefficient of the unit cell obtained from CST full-wave simulation using periodic boundary conditions. It can be observed from Fig. 3.9 that the reflection coefficient is less than -10 dB between 2.2 GHz and 18.4 GHz, which leads to over 90% absorptivity within this frequency range. There are three absorption peaks located at 2.8 GHz, 9.2 GHz, and 16.6 GHz, respectively. The reflection coefficient obtained from circuit model analysis

is also displayed in Fig. 3.9 by the black line, which is in good agreement with the red one, indicating the accuracy of the equivalent circuit model.

3.2.3 Efficacy of the WAIM layer

To investigate the influence of the WAIM layer on the absorption performance and verify the efficacy of the WAIM layer, the unit cell models with and without the WAIM layer are simulated with CST, respectively. Fig. 3.10 illustrates the simulated reflection coefficients, as well as the absorption bandwidth comparison of the unit cell with and without the WAIM layer. It can be seen from the comparison that although the WAIM layer increases the total thickness of the designed structure, it does improve the absorption performance and broaden the effective absorption bandwidth.

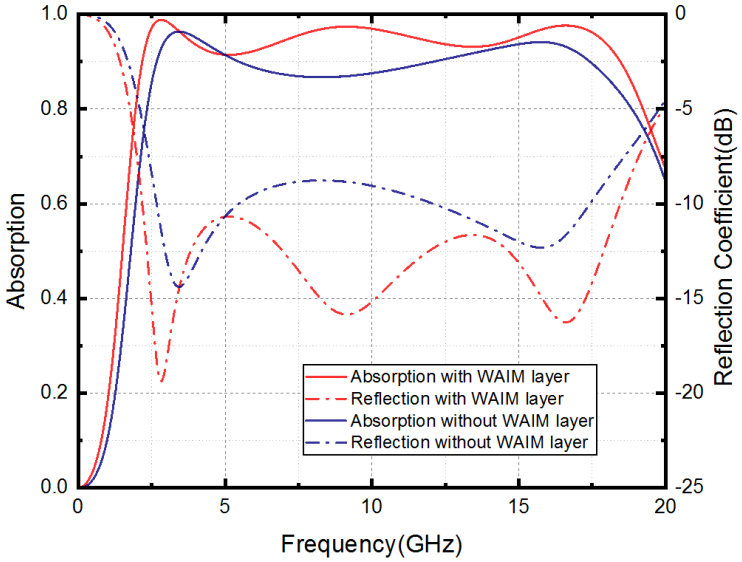

Fig. 3.10 The comparison of simulation results of the proposed absorber with and without the WAIM layer on top.

The efficacy of the WAIM layer is also further investigated through the operation performance under wide incident angles. The absorption results with and without WAIM layer under oblique incident angles from 0° to 60° with the step of 10° for transverse electric (TE) wave and transverse magnetic (TM) wave are simulated and displayed in Fig. 3.11. It can be seen from the absorption contour maps that the absorber with WAIM layer (as shown in Fig. 3.11 (a)

and (c)) has a much better wide-angle operation performance comparing with that without WAIM layer (as shown in Fig. 3.11 (b) and (d)), which verifies the efficacy of the WAIM layer. For TE mode illustrated in Fig. 3.11 (a), the absorption of the proposed absorber decreases as the incident angle increases. Within the operation frequency range (2.2 GHz – 18.4 GHz), the absorptivity keeps over 80% even at incident angle of 50 °. On the other hand, with the incident angle increases to 60 ° under TM mode in Fig. 3.11 (c), the absorber remains broadband effective absorption (over 90% absorptivity). Although the operation frequency range moves slightly to higher frequency, the effective absorption can still be achieved in S-, C-, X-, and Ku-band. The performance under various incident angles indicates the ultra-wideband absorber based on double layer graphene patterns and topped with single WAIM layer is a wide-angle absorber.

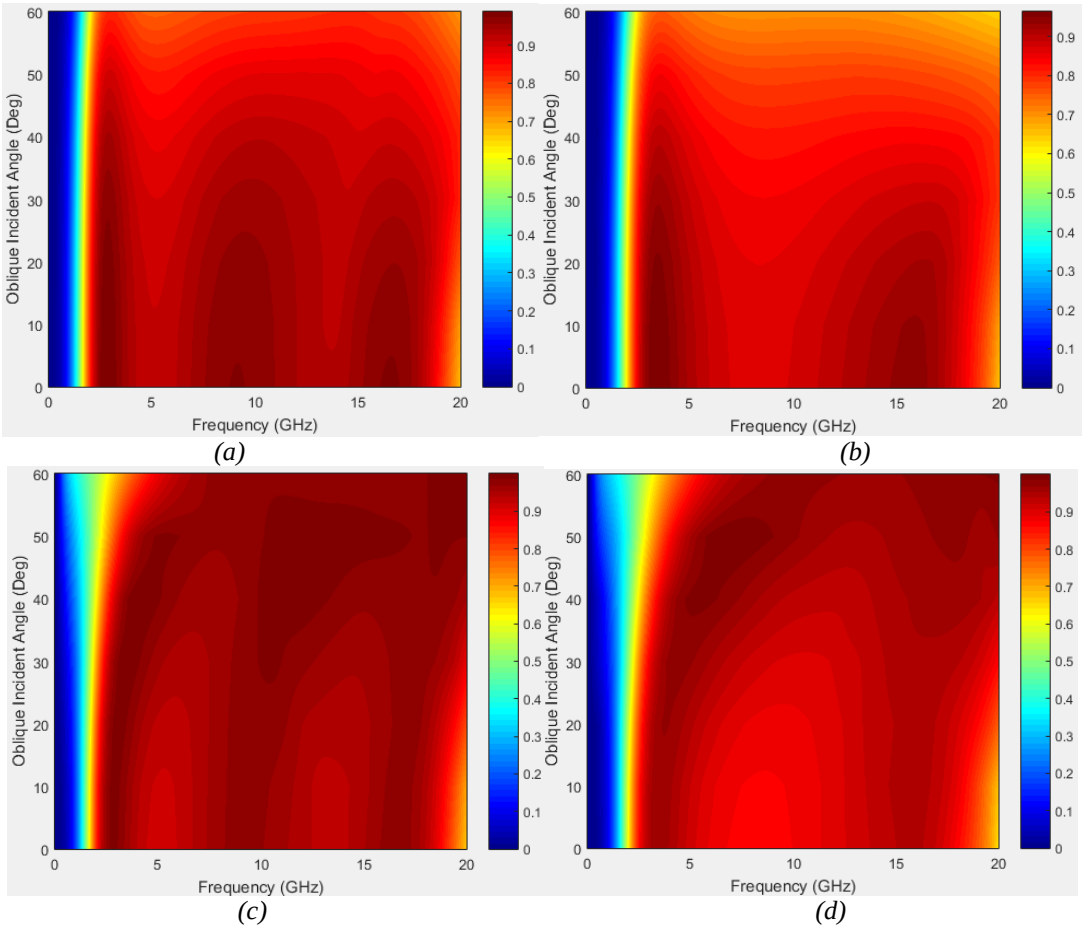

Fig. 3.11 Absorption contour map of the absorber with and without WAIM layer under oblique incident angles from 0 ° to 60 ° with the step of 10 ° for (a) TE mode (with WAIM layer), (b) TE mode (without WAIM layer), (c) TM mode (with WAIM layer) and (d) TM mode (without WAIM layer).

3.3 Chapter Summary

In this chapter, two different multilayer broadband metamaterial absorbers based on printed graphene patterns are designed and simulated through multilayer structure approach and analyzed through equivalent circuit model method. Both of the two multilayer absorbers are polarization-insensitive and angle-insensitive. They have exactly the same relative absorption bandwidth of 157%, while operate in different microwave frequency bands. The effective absorption bandwidth at normal incidence of the first absorber in section 3.1 is from 6 GHz to 50 GHz, while that of the second one is from 2.2 GHz to 18.4 GHz, covering S-, C-, X-, and Ku-band.

The equivalent circuit models of the two absorbers are investigated thoroughly. The results derived from the equivalent circuit models agree well with the full-wave simulation results, which indicate the accuracy of the equivalent models. For the second absorber, a single WAIM layer is added at the top of the structure to improve the wide-angle and broadband frequency performance at relatively lower microwave frequencies. The numerical simulation results under various incident angles show a good absorption performance for both TE and TM modes, indicating the efficacy of the WAIM layer.

Due to the fabrication complexity of the multilayer structures with multi-layer graphene patterns, there is no experimental validation for the simulation results in this chapter. However, the experimental demonstration can be expected in the near future with the rapid development of graphene printing techniques.

Chapter 4: Novel Ultra-thin Printed Graphene Radar Absorber with Ultra-wide Fractional Bandwidth

Generally, with fixed geometry of patterns for a metamaterial absorber, when the thickness of the dielectric substrate is increased, the absorption bandwidth will have a red shift, moving to lower frequencies. In this chapter, an ultra-thin printed graphene radar absorber with novel absorption mechanism is introduced. This absorber provides better absorption performance and works at lower frequency bands when the thickness of dielectric substrate decreases.

4.1 Design and Ultra-wideband Performance

This metamaterial absorber consists of two layers of printed graphene sheets, one layer of dielectric substrate, and a metal ground plane. As shown in Fig. 4.1, the two resistive sheets are printed on the top surface and bottom surface of the dielectric substrate, respectively, composing a sandwich-like structure. The metal ground plane is put on the back of the sandwich structure. In CST numerical simulation, the top layer of patterns have a sheet resistance of 10 Ω/sq, while the bottom layer of patterns have a sheet resistance of 1600 Ω/sq, and the dielectric substrate is chosen to be silicone with dielectric constant of 2.9 and loss tangent of 0.1. A perfect electric conductor (PEC) is used to simulate the metal ground plane. The geometric parameters in Fig. 4.1 are as follows: P = 45 mm, a = 36 mm, b = 27 mm, c = 12 mm, d = e = 3 mm, w = 4.5 mm, L = 44.5 mm. The thickness of the dielectric substrate is 0.3 mm.

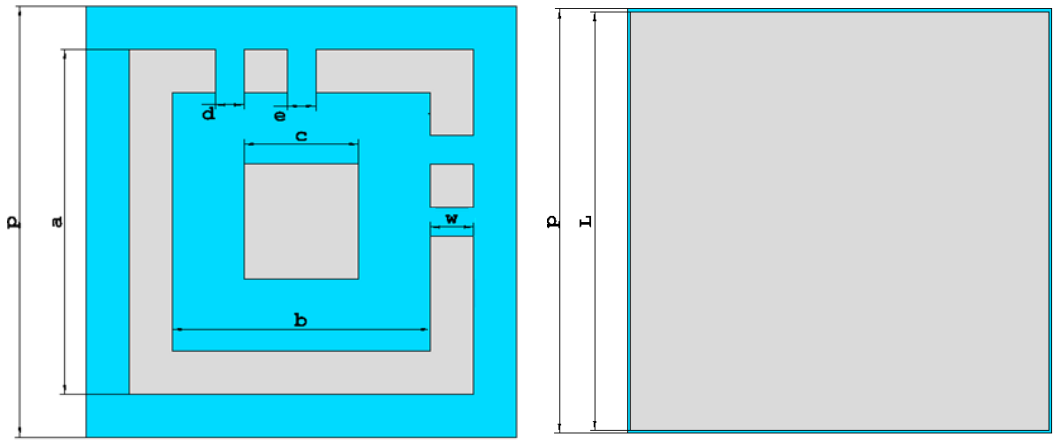

(a) *(b)*

Fig. 4.1 The schematic diagram of the sandwich structure composed of two layers printed graphene patterns and one layer of dielectric substrate. *(a)* The top layer patterns of the structure and *(b)* the bottom resistive sheet.

The simulated absorption of this metamaterial absorber at normal incidence is displayed in Fig. 4.2 through the red line. This absorber can achieve the effective absorption (over 90% absorptivity) from 1.15 GHz to 20 GHz, with an ultra-wide bandwidth of 21.15 GHz and the relative absorption bandwidth of 178%.

In order to investigate the performance of this absorber at various angles of incidence, the absorption performance at different incident angles for transverse electric (TE) and transverse magnetic (TM) waves are simulated separately, and the results are displayed in Fig. 4.2 (a) and Fig. 4.2 (b), respectively. The absorption results in Fig. 4.2 (a) indicate that for the TE mode, the absorptivity and the effective absorption bandwidth decrease slightly as the incident angle varies from 0 ° to 60 °. When the incident angle is increased to 60 °, the absorptivity is still over 80% from about 1.08 GHz to 17 GHz. For the TM mode, the absorptivity also changes slightly as the incident angle varies from 0 ° to 40 °. As the incident angle raised, the absorptivity at lower frequency bands decreases while it increases at higher frequency, indicating that for the TM mode, the effective absorption band have a blue shift as the incident angle increases. In conclusion, this absorber shows relatively stable performances at wide incident angles for both TE and TM waves.

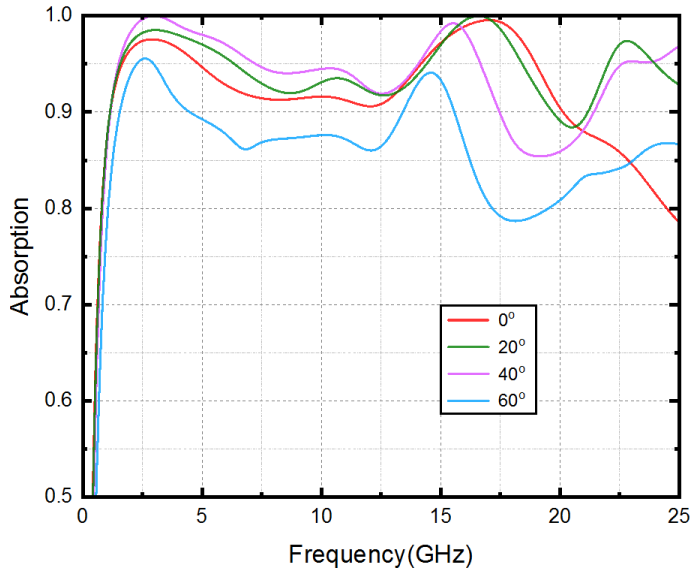

(a)

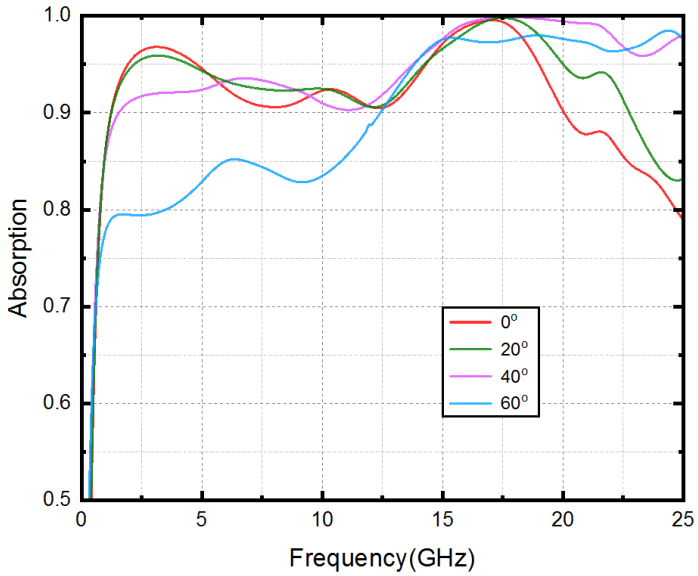

(b)

Fig. 4.2 Simulated absorption performances at incident angles from 0 °to 60 °with a step of 20 °for *(a)* TE waves and *(b)* TM waves, respectively.

4.2 Influence of Different Parameters on Absorption Performances

To analyze the influence of the dielectric substrate's thickness and the printed patterns' sheet resistances on the absorption performances. The unit cell model with different parameters is required to be simulated. To begin with, the sheet resistance of the bottom square patch is changed from 600 Ω/sq to 3100 Ω/sq with a step of 500 Ω/sq. From Fig. 4.3, it can be seen that the absorption within the frequency range from 5 GHz to 10 GHz reduces to a value lower than

90% when the sheet resistance increases to 2100 Ω/sq. On the other hand, when the sheet resistance decreases to 600 Ω/sq, the absorption at the middle part of frequency range is below 90%. It is worth noting that with a sheet resistance of 1100 Ω/sq, this absorber can achieve an even broader effective absorption bandwidth. Furthermore, the over 80% absorptivity can still be achieved over a broad frequency band within the large changing range from 600 Ω/sq to 3100 Ω/sq, indicating that this design has a great tolerance of fabrication deviations for the printed graphene resistive sheets at the bottom layer.

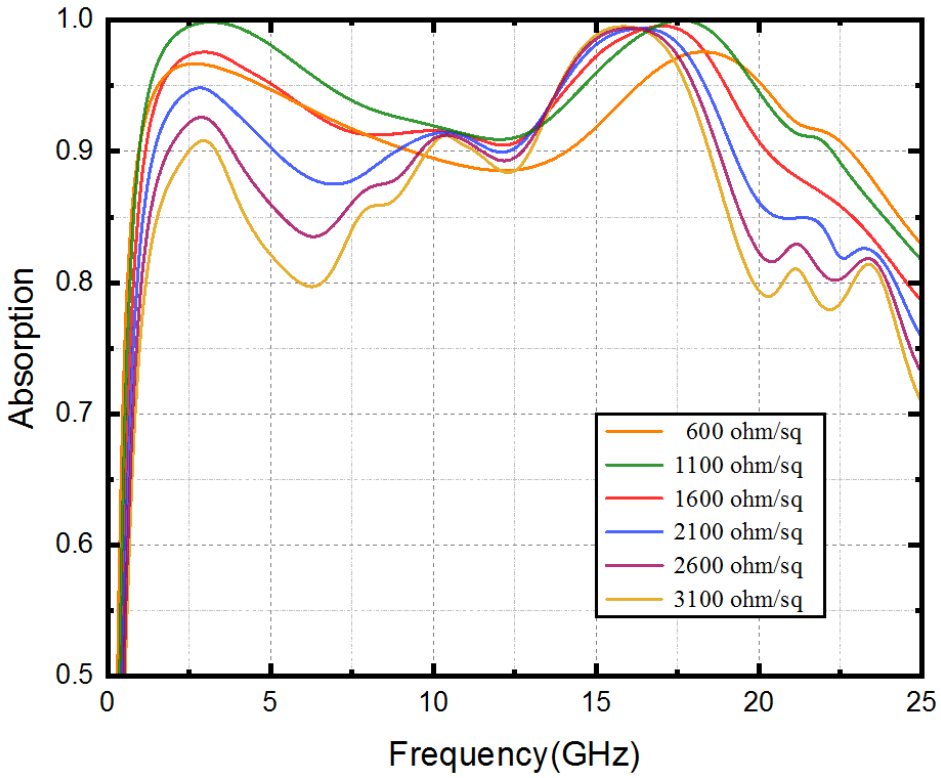

Fig. 4.3 Simulated absorption performances with various sheet resistances of the bottom square.

Fig. 4.4 shows the absorption results of the absorber with different sheet resistances of the printed resistive patterns on the top layer. With the sheet resistance lower than 5 Ω/sq, the absorption at around 13 GHz decreases and cannot achieve 90% absorptivity. When the sheet resistance is increased to 20 Ω/sq, the better absorption performance is obtained with higher absorptivity over the operation frequency range, indicating an optimization of the absorption performance with higher sheet resistances for the top layer patterns. However, as the sheet

resistance keeps increasing to higher than 50 Ω/sq, the absorption performance at lower frequencies gets worse.

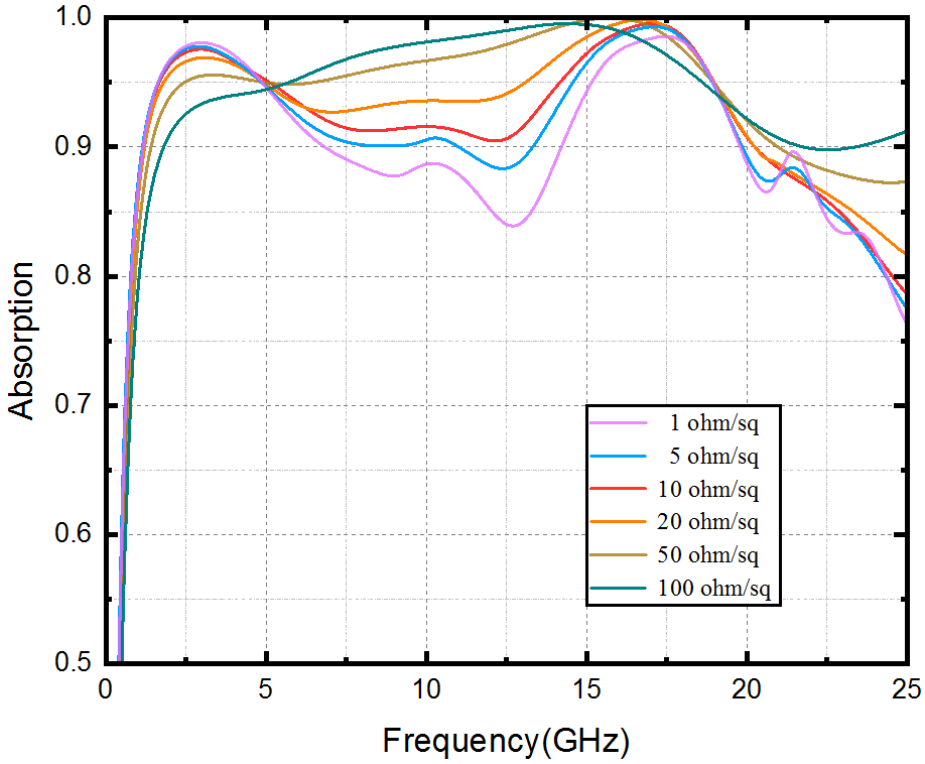

Fig. 4.4 Simulated absorption performances with various sheet resistance values of the top layer pattern.

The influence of the thickness of dielectric substrate is investigated and illustrated in Fig. 4.5. Unlike common metamaterial absorbers, thicker dielectric substrate of this absorber cannot result in a red shift of the absorption bandwidth. With the thickness increases from 0.1 mm to 1.5 mm, the absorption performance at lower frequency band (from 1.25 GHz to 3.68 GHz) almost keeps unchanged, while the absorption performance from 3.68 GHz to 25 GHz decreases. Comparing the absorption results with various values of substrate thickness, it is obvious that thinner dielectric substrate provides broader effective absorption (>90%) bandwidth.

The influence of the dimension of center square patch is also investigated and illustrated in Fig. 4.6. With the side length increased from 4 mm to 12 mm, the lower border of effective absorption band almost keeps unchanged, while the upper border moves to higher frequency,

leading to a broader effective absorption bandwidth. When the side length increases to longer than 16 mm, the square patch keeps enlarged and the absorption performance gets worse.

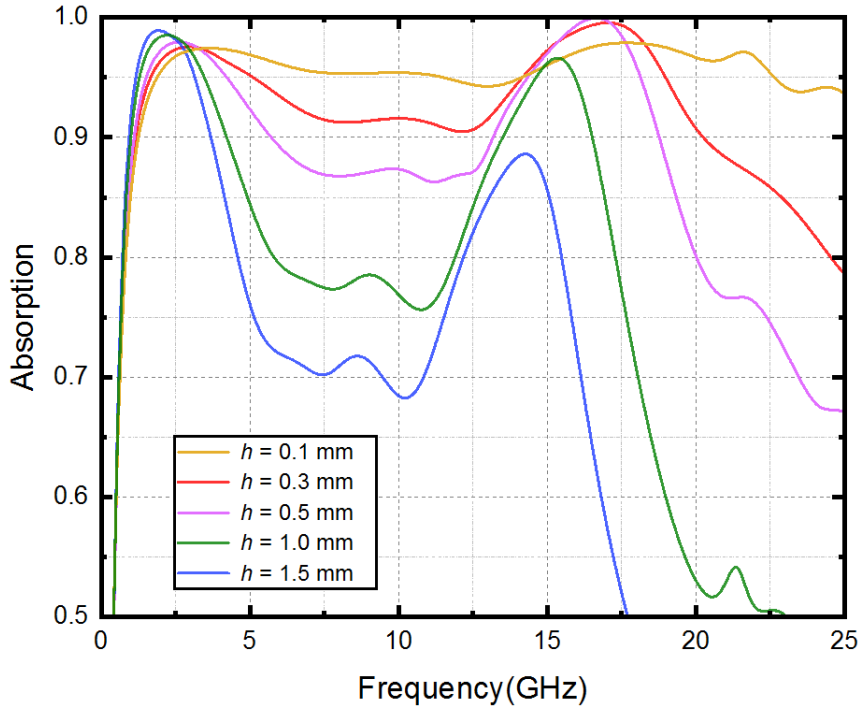

Fig. 4.5 Simulated absorption performances with various thickness of the dielectric substrate.

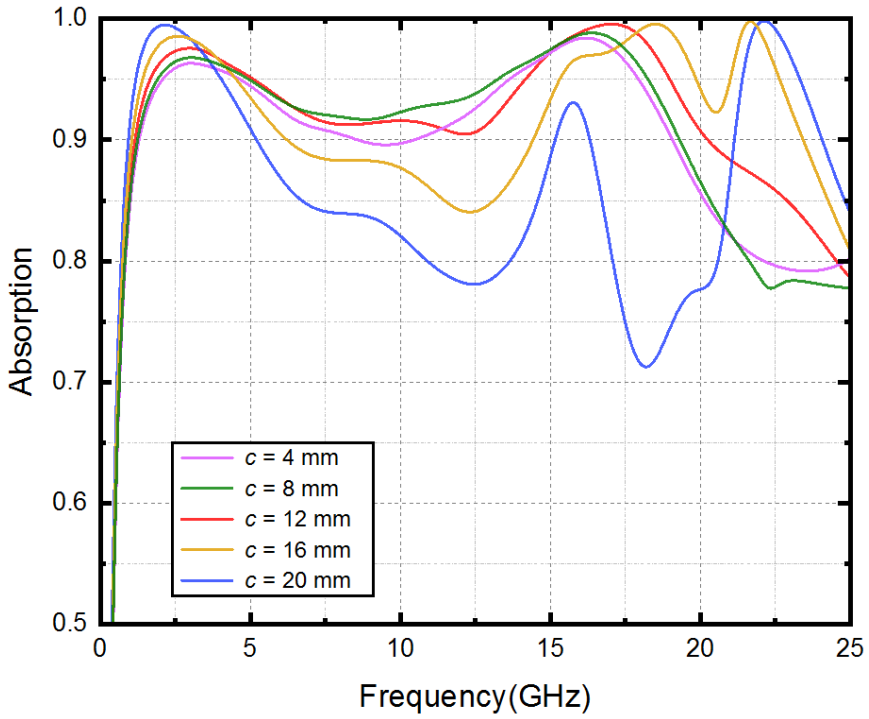

Fig. 4.6 Simulated absorption performances with various dimensions of the center square patch.

The dimension of the interstices on the top and right sides of the outer square ring is investigated. The absorption results of the absorber with different size of interstices are illustrated in Fig. 4.7. It can be seen that with narrow interstices (when the dimension is 1 mm or 2 mm), the absorption of the middle part of the frequency band is below 90%. When the interstices are wider than 3 mm, the absorptivity at lower frequency band (around 2.5 GHz) decreases as the interstices become wider, while the absorptivity at higher frequency band (around 17.5 GHz) increases. Although the absorptivity has certain fluctuations at different frequencies, the effective absorption bandwidth almost keeps unchanged as the dimension increases from 3 mm to 5 mm.

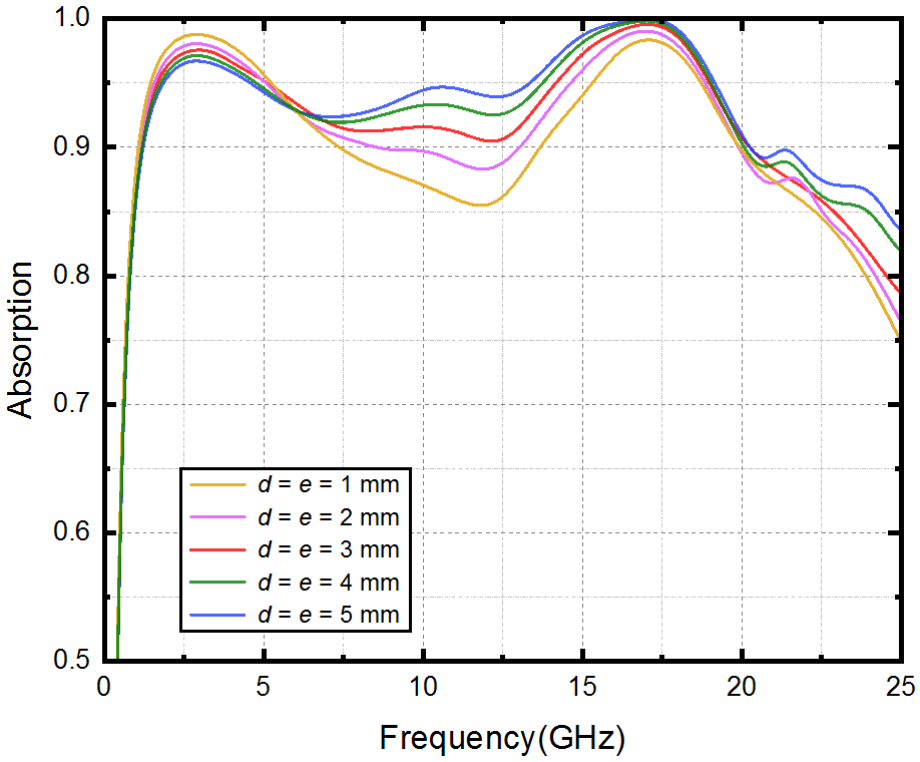

Fig. 4.7 Simulated absorption performances with various dimensions of the interstices on the top and right sides of the outer square ring.

4.3 Investigation of Absorption Mechanism

The distributions of power loss density for TE mode at frequency 3 GHz, 10 GHz, 13 GHz, and 17 GHz are illustrated in Fig. 4.8 to investigate the absorption mechanism. It can be seen that this structure resonates at different spatial areas for different frequencies. At 2 GHz, the power loss locates mainly at the corners of both the inner centre square and outer square ring, while at 8

GHz, the power loss takes place at the edges of the inner centre square and outer square ring. At 14 GHz, the power loss is mainly concentrated at the interspace part on the left of the centre square and the two interstices on the right side of the outer square ring, while at 20 GHz, the power loss density distributes at the interspace between unit cells, the two interstices on the top side of the outer square ring, and the interspace between the inner centre square and the outer square ring on each of the unit cells, with more of the power loss occurs at the interspace on the right part of the centre square.

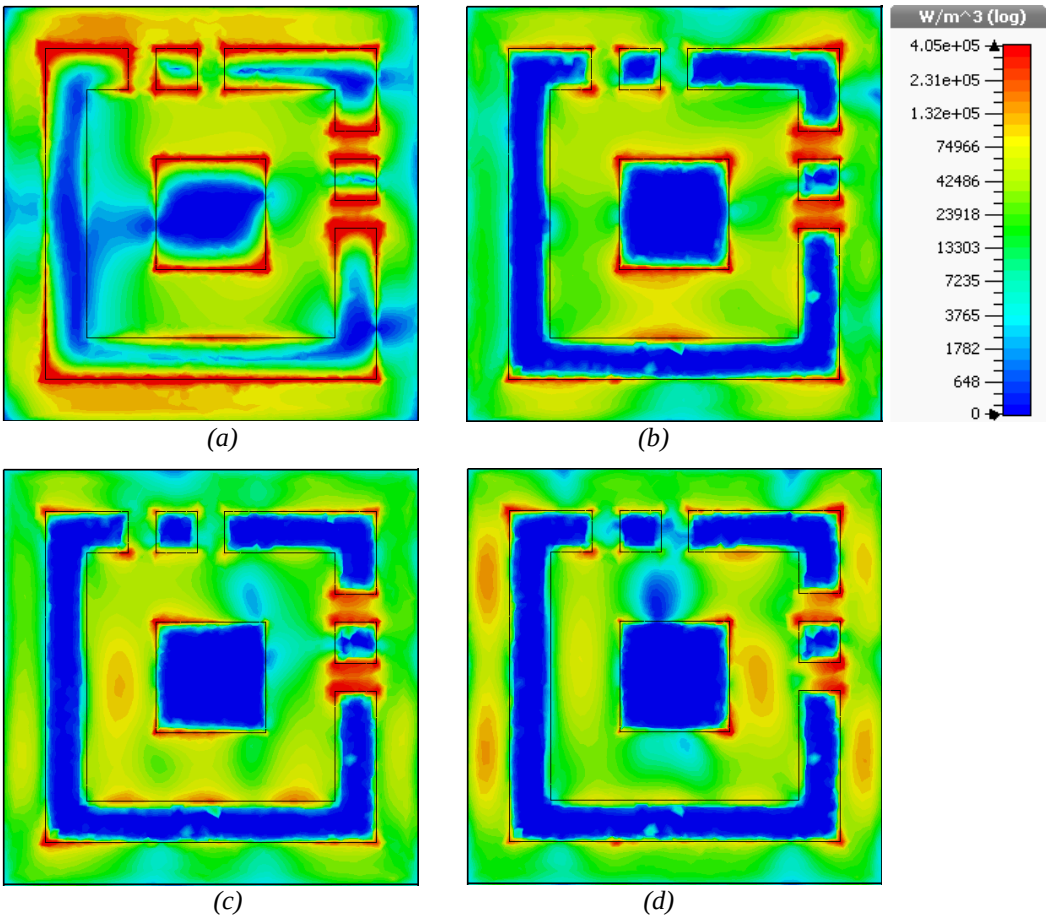

Fig. 4.8 Distributions of power loss density for TE (transverse electric) mode at *(a)* 3 GHz, *(b)* 10 GHz, *(c)* 13 GHz, and *(d)* 17 GHz.

To elucidate the absorption mechanism of the ultra-thin metamaterial radar absorber more thoroughly, the distribution of surface currents at 14 GHz is displayed in Fig. 4.9. Fig. 4.9 (a), (b) and (c) show the surface currents in the top layer of printed graphene pattern, the surface currents in the bottom layer of resistive sheet and the overall surface currents in both layers, respectively.

The arrows in the figures signify the directions of the surface currents. The surface currents in the bottom layer of resistive sheet might be excited by the ohmic contact between the metal ground plane and the resistive sheet. At the contact, some of electrons from one material move to the other material due to the different energy of charge carriers in different materials, leading to a double layer that balances the electrochemical potentials in both materials and creates a discontinuity in the electric potential, which contributes to the surface currents in the bottom layer of resistive sheet observed in Fig. 4.9 (b). As shown in Fig. 4.9 (a) and (b), the surface currents in the outer square ring from the top layer of resistive patterns and the surface currents in the bottom layer of resistive sheet have opposite directions. The anti-parallel surface currents lead to strong magnetic resonances. The thickness of this substrate is very thin, which is merely 0.3 mm. If the distance between the surface currents from two layers can be ignored, these surface currents, as displayed in Fig. 4.9 (c), can together constitute current loops like eddy currents flowing in closed loops within conductors, and lead to energy loss in the material. Comparing with the distribution of power loss density in Fig. 4.8 (c), the locations of these eddy currents are exactly the same with the locations where the power loss occurs. This also explains the influence of substrate thickness on the absorption performance to a certain extent. As the thickness of dielectric substrate increases, the distance between the anti-parallel surface currents from the two layers of resistive patterns also increases and cannot be omitted, which means no eddy currents can be achieved.

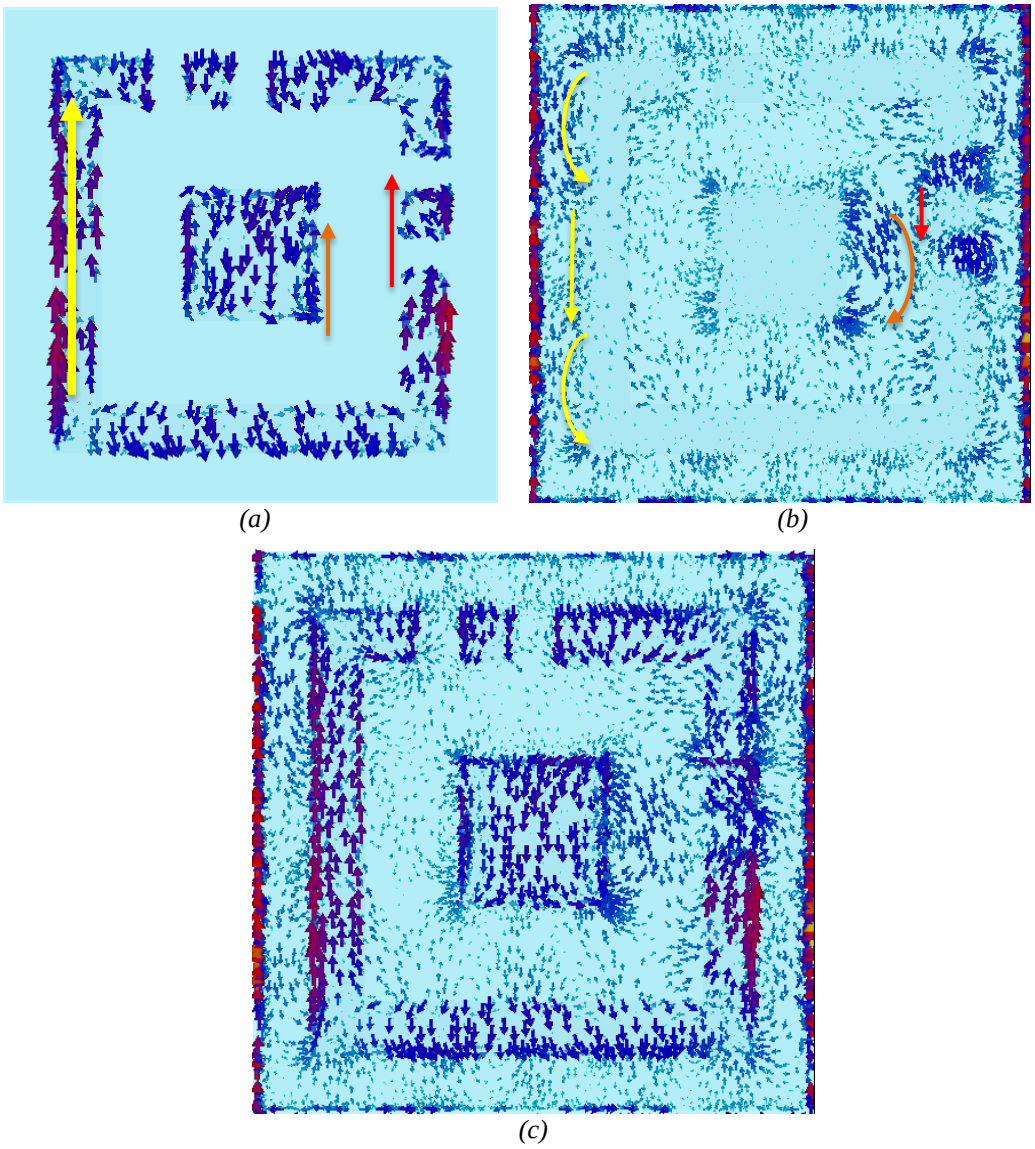

Fig. 4.9 Distributions of surface currents at 17 GHz for TE mode. *(a)* The surface currents in the top layer patterns of the unit cell, *(b)* the surface currents in the bottom resistive sheet and *(c)* the overall surface currents in both layers.

4.4 Chapter Summary

This chapter concerns the eddy current approach, according to which the absorbers with smaller thickness can achieve broader absorption bandwidth. To demonstrate this approach, an ultra-thin broadband metamaterial radar absorber which is composed of two different layers of printed graphene resistive patterns placed on the front and back surface of the 0.3 mm dielectric substrate is designed.

The mechanism of the high absorption in broadband is elucidated through the distributions of power loss density and surface currents. As the thickness of the dielectric substrate becomes thin enough to be omitted, the anti-parallel surface currents in the front and back surfaces constitute current loops like eddy currents flowing in closed loops within conductors, and lead to strong magnetic resonances and energy loss in the material. This absorber is numerically simulated to achieve an effective absorption from 1.15 GHz to 20 GHz, with a relative absorption bandwidth of 178%. Compared with other metamaterial radar absorbers proposed in recent years, this design has significant advantage in thickness and relative absorption bandwidth, indicating the outstanding efficacy of the eddy current approach.

Chapter 5: Experimental Demonstration of Controlling Graphene Sheet Resistance for Broadband Printable and Flexible AMC Based Radar Absorber: Anti-phase Reflection Cancellation Approach

Current artificial magnetic conductor (AMC) designs use metallic patterns on rigid substrates and focus on shapes and sizes of AMC structures, rather than on material performance, which has hindered operation bandwidth and design flexibility. In this chapter, a novel approach to achieve the effective phase difference between two AMC structures with printed graphene resistive sheet is presented. To verify the novel approach of designing printed graphene AMCs, a fully screen printed graphene AMC-based broadband and flexible microwave radar absorber is designed, analyzed, and experimentally demonstrated. The presented absorber not only redirects but also absorbs the incident wave so to broaden the operation bandwidth. Contrasting to other reported works, the phase characteristics of the AMCs are realized through the control of the surface resistance provided by printed graphene laminates. The AMCs in this design are composed of printed graphene ring arrays with exactly the same shape and size, but different sheet resistances. By carefully designing the sheet resistance of printed graphene laminates, the optimized anti-phase reflection cancellation between AMCs can be achieved. With printed graphene AMCs and flexible dielectric substrate, the presented absorber has a broadband effective absorption (above 90% absorptivity) from 7.58 GHz to 18 GHz, is polarization insensitive under normal incident and can work at relatively wide incident angles. Furthermore, this absorber is capable of bending easily with notable performance, which makes it ideal for applications with irregular and uneven shapes.

5.1 Printed Graphene

5.1.1 Graphene conductive ink preparation and screen printing process

Pristine graphite flakes (Alfa Aesar, >99%) were first dispersed in 400ml of N-Methyl-2-pyrrolidone (NMP, Sigma, >99%) in a concentration of 20 mg ml^{-1}. After sonication for 24h, the mixture was filtered with a 300-mesh stainless steel screen and centrifuged at low speed (500 rpm) for 20 min. Then NMP was removed from the obtained dispersion through vacuum filtering. In order to achieve appropriate viscosity for screen printing, the collected graphene nanoflakes were re-dispersed in viscous solvent Ethylene Glycol (Alfa Aesar, >99%) at concentration of 50 mg ml^{-1}.

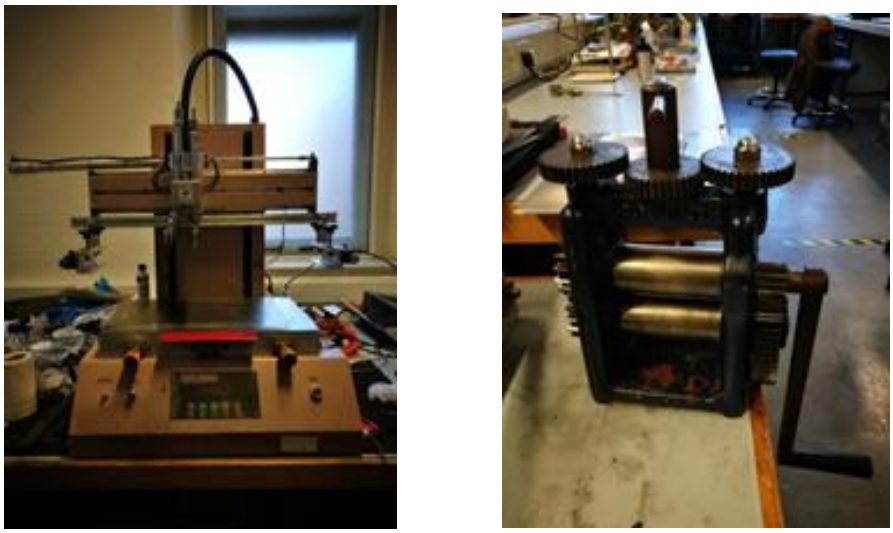

(a) *(b)*

Fig. 5.1 (a) Screen printer and (b) roller compressor.

Screen printing was performed to print graphene patterns on normal A4 printing papers. The semi-automatic pneumatics screen printer (YICAI4060PV) with pneumatic cylinder (XINGCHEN CQ2B32-20, max press of 0.7 MPa) was used for screen printing. The printer worked at a printing speed of 70–90 mm s^{-1} with a 70 ° angle squeegee. The printing screen of 49 mesh was specially fabricated and patterned with capillary film (ULANO, EZ50-Orange) to achieve the uniform laminate and resolution. The printed samples were dried in an oven under

vacuum environment at 120 °for 5 hours. Samples with required sheet resistances were obtained through a further rolling compression.

5.1.2 Characterization of printed graphene sample

The conductivity of the prepared samples can be obtained through

$$\sigma = \frac{1}{R_s \times t} \tag{5.1}$$

where R_s is sheet resistance of printed graphene patterns, which can be measured using 4-point probe station (Jandel, RM3000) and semiconductor characterization system (Keithley, 4200C), while *t* is the thickness of the printed graphene patterns, which can be represented by the average thickness of the printed layers measured based on cross-section SEM view.

Fig. 5.2 and Fig. 5.3 display SEM images of 3 samples of the printed graphene laminates on paper substrate. The three rectangular samples had the dimension of 8 mm × 25 mm, with Sample 1 and 3 were printed at the same time to make sure they had the same sheet resistance after the printing process, while Sample 2 with a higher sheet resistance was printed separately from the others. Then the compressing process was only applied to Sample 3 to obtain a sheet resistance lower than Sample 1. By using the 4-point probe measurement, the sheet resistances of Samples 1, 2, and 3 were measured to be 36.6 Ω/sq, 98 Ω/sq, and 8.7 Ω/sq, respectively. Through controlling the thickness of the printed graphene laminates during the printing and compressing processes, different sheet resistances of graphene laminates can be achieved. With relatively lower printing speed and squeegee pressure, the graphene laminate of Sample 1 was made thicker than that of Sample 2, as shown in Fig. 5.2 (a) and (b), resulting in a relatively lower sheet resistance. Based on the cross-section SEM view in Fig. 5.2 (a), the average thickness of Sample 1 (uncompressed sample) was measured to be around 54 μm. With the measured sheet resistance of 36.6 Ω/sq, the conductivity was calculated to be 506 S/m according to Eq.(5.1).

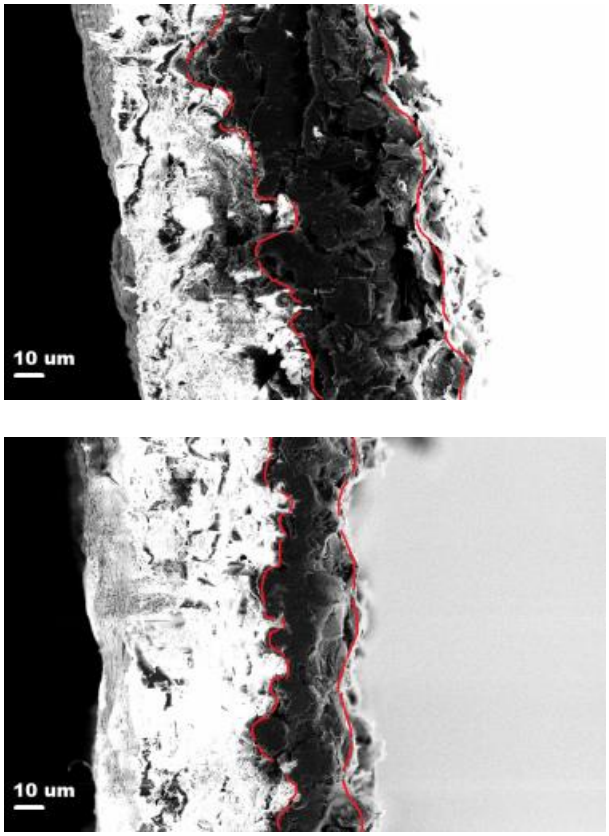

Fig.5.2 SEM images of printed graphene laminates on paper substrate: cross-section view of uncompressed (a) sample 1 (sheet resistance of 36.6 Ω/sq) and (b) sample 2 (sheet resistance of 98 Ω/sq) with 500× magnification.

To obtain a much lower sheet resistance, rolling compression was applied in preparing Sample 3. Unlike the uncompressed samples with porous structure which limits the conductivity (Fig.5.3 (a) and (b)), the graphene laminate of Sample 3 had much denser surface, as shown in Fig. 5.3 (c) and (d). The average thickness of compressed Sample 3 was measured to be 18.7 μm, and the conductivity was calculated to be 6.14×10^3 S/m, which led to a sheet resistance of 8.7 Ω/sq. More details of printed graphene electrical properties can be found in [208, 209].

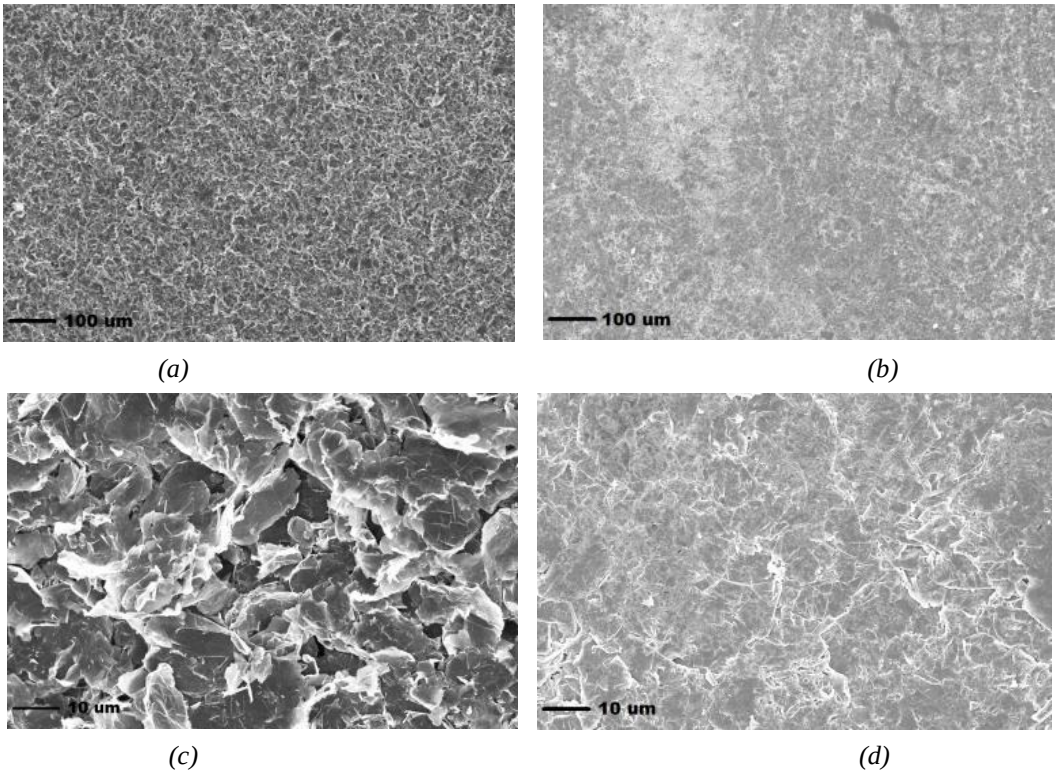

Fig. 5.3 SEM images of printed graphene laminates on paper substrate: Top view of (a) uncompressed sample 1 and (b) compressed sample 3 (sheet resistance of 8.7 Ω/sq) with 100× magnification, (c) uncompressed sample 1 and (d) compressed sample 3 with 1000× magnification.

5.2 Design of Printed Graphene AMCs and Numerical Simulation Results

5.2.1 AMC cells with square-ring arrays

As displayed in Fig. 5.4 (a), two AMC structures with different sheet resistance are periodically arranged in a chessboard configuration. Each AMC structure is composed of a 4 × 4 square ring patch array with 16 unit cells as seen in Fig. 5.4 (b). Fig. 5.4 (c) displays the single unit cell with parameters a = 5.6 mm, b = 4.4 mm, p = 7 mm, h = 3.5 mm. The shape and size are exactly the same for the two AMC structures. The only difference between them is the sheet resistance. CST Microwave Studio is used to simulate the phase characteristics and absorption properties of the proposed AMC structures and radar absorber. In the simulation, the AMC square ring patches are modelled with different sheet resistance rs_1 and rs_2. Silicone with dielectric constant of 2.9 is chosen as the substrate. A PEC is used as the ground plane. To obtain broadband anti-phase reflections for two AMC structures, the reflection phase difference between two AMC structures is required to be around 180° in the widest possible frequency band. The

sheet resistances rs_1 and rs_2 for AMC 1 and AMC 2 are optimized to be 8 Ω/sq and 120 Ω/sq, respectively.

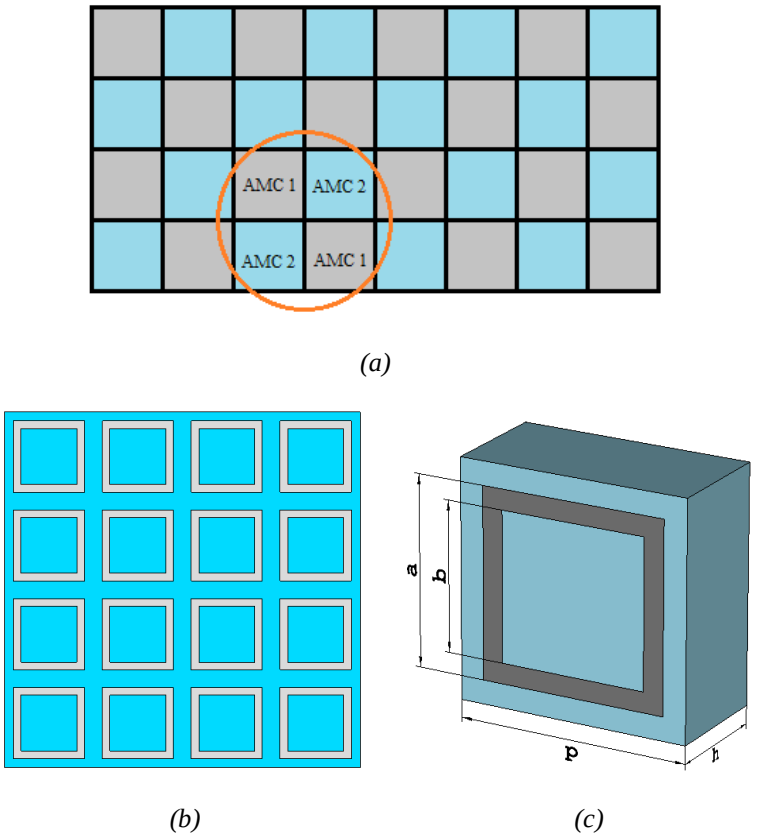

(a)

(b) *(c)*

Fig. 5.4 Proposed metasurface AMC absorber and unit cell. *(a)* Chessboard configuration of the metamaterial radar absorber. *(b)* AMC structure with a 4 × 4 square ring patch array. *(c)* Single unit cell with square ring patch.

By modelling the unit cell in Fig. 5.4 (c) as an infinite periodic structure, the reflection phases of the AMC structures with different sheet resistance can be obtained and the phase difference between them is displayed in Fig. 5.5. Following array theory, in the ideal case of an infinite chessboard surface, a phase difference within $180° \pm 37°$ can provide a 10 dB RCS reduction (90% absorptivity). From Fig. 5.5, the phase difference is maintained between $143° \sim 217°$ from 7 GHz to 13.8 GHz. As illustrated in Fig. 5.6, each individual AMC structure provides very narrow band absorption. However, the combination of them, thanks to the combined phase characteristics due to the difference of the surface resistance, exhibits much wider absorption bandwidth. Furthermore the bandwidth can be controlled by adjusting the sheet resistance, which provides an

opportunity of novel tuning mechanism for tuneable radar absorbers either electronically or optically.

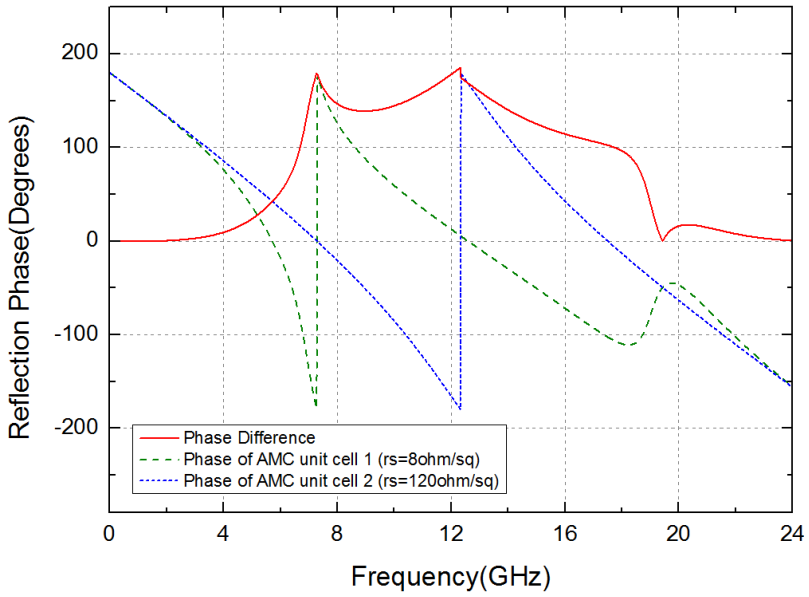

Fig. 5.5 Reflected phases of two AMC structures and the phase difference between them.

As illustrated in Fig. 5.6, the AMC structure with sheet resistance of 120 Ω/sq cannot achieve over 90% absorptivity within the given frequency band. The AMC structure with sheet resistance of 8 Ω/sq can achieve over 90% absorptivity with narrow bandwidth from 6.34 GHz to 7.85 GHz, which provides a narrow relative absorption bandwidth of 21%. By combining them in a chessboard configuration, the effective phase difference between two AMC structures leads to destructive interference and anti-phase reflections are cancelled out, which results in over 90% absorptivity from 6.68 GHz to 12.27 GHz with a relative absorption bandwidth of 59%, increasing the absorption bandwidth significantly. It is worth to point out that the absorption in our proposed structure is not only influenced by the cancellation effect of reflections due to the phase difference, but also by the absorption of AMC cells due to their own resistance. Nevertheless, the phase cancellation has played a dominant role as indicated in Fig. 5.6.

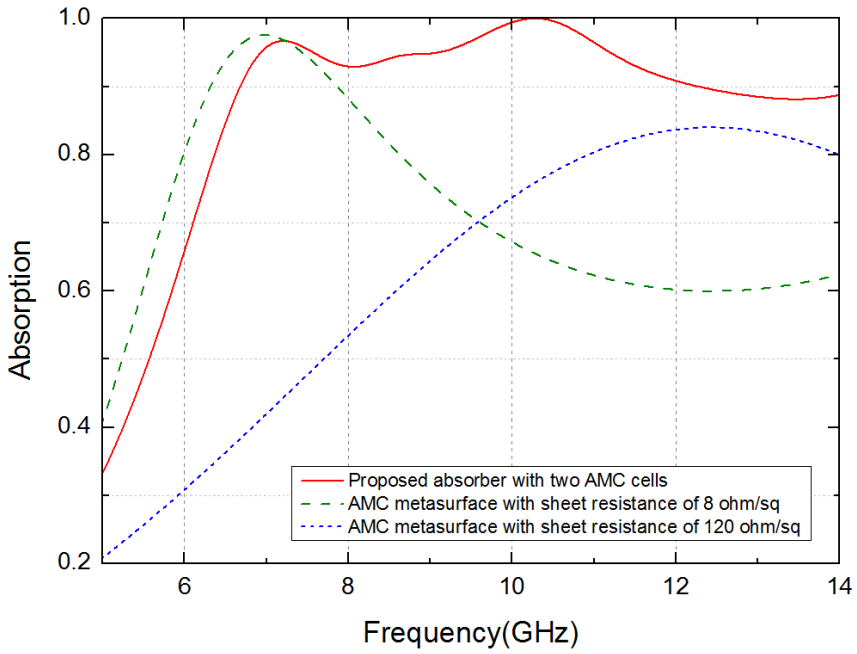

Fig. 5.6 Simulated absorption results of proposed radar absorber and two different AMC structures.

5.2.2 AMC cells with optimized circular-ring arrays

The foregoing design verifies the novel approach of achieving the effective phase difference between two AMC structures with printed graphene resistive sheet. Based on the foregoing design, the graphene printed AMC structures with circular-ring arrays are presented in this section to obtain a wider effective absorption bandwidth.

Similar with the foregoing design, the elementary unit cell of AMCs is composed of printed graphene resistive circular ring, two layers of dielectric substrates, and a metal ground plane. CST Microwave Studio has been used to optimize the elementary unit cell design.

Each elementary unit cell, as shown in Fig. 5.7 (a), is modelled as an infinite periodic structure by independently applying periodic boundary condition in x and y directions, and Floquet boundary condition in z direction. A perfect electric conductor (PEC) is assumed for the metal ground plane. The supporting dielectric substrate of 3 mm thickness is chosen to be silicone (Polymax, SILONA Translucent Silicone Sheet 60ShA FDA) with dielectric constant of 2.9. Silicone substrate is not only hydrophobic (not suitable for printing graphene on it) but also not

suitable for compressing process. Graphene rings are printed on hydrophilic paper with dielectric constant of 3.5 and thickness of 0.1 mm, which is placed on the top of the silicone substrate. The printed graphene patterns are simulated as ohmic sheet surfaces with specific resistances in the design.

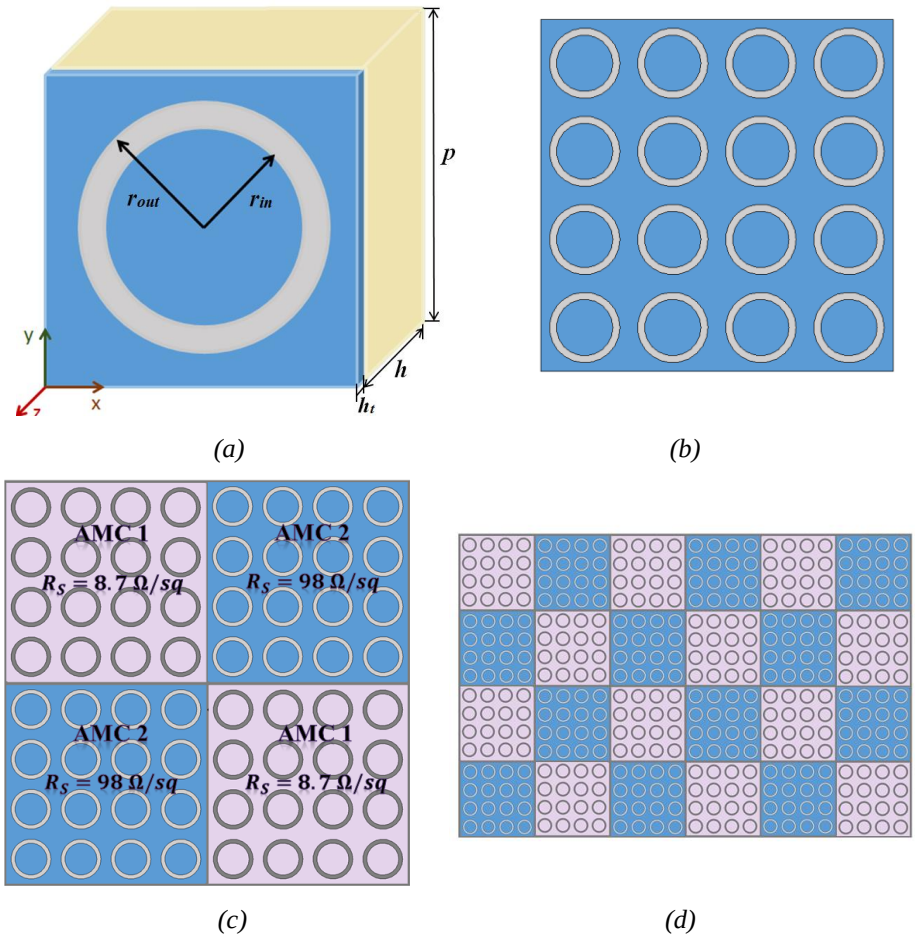

Fig. 5.7 (a) Elementary unit cell of the AMC radar absorber: p = 7.5, r_{out} = 3, r_{in} = 2.4, h = 3, h_t = 0.1 (unit: mm). (b) Unit AMC lattice of 4×4 elementary unit cell arrays. (c) Functional unit cell of 2×2 dual AMC lattices. (d) Chessboard configuration of periodically arranged AMCs of the proposed printed graphene radar absorber.

Fig. 5.7 (b) shows a 4 x 4 elementary unit cell array, which constitutes a unit AMC lattice. To investigate the effects of combination of AMC lattices with different sheet resistances, various combinations have been studied numerically. It is revealed that 2 x 2 dual AMC lattices, as shown in Fig. 5.7 (c), can provide much wider effective absorption bandwidth than if only uniform AMC lattices (i.e., all rings have the same sheet resistance) are used. Such 2 x 2 dual AMC lattices have been used to constitute a functional unit cell of the proposed radar absorber. To verify the novel

approach of achieving phase cancellation purely through different sheet resistances of two AMCs, the appropriate sheet resistances for AMC1 and AMC2 which can meet our design requirement were optimized to be 8.7 Ω/sq and 98 Ω/sq through numerical simulation, respectively. Fig. 5.7 (d) illustrates the bird's view of the absorber, which has a chessboard configuration composed of many functional unit cells.

The absorptivity of printed graphene AMC surface can be obtained through the formula $1 - T(\omega) - R(\omega)$, where $T(\omega)$ is the transmission and $R(\omega)$ is the reflection. Due to the metal ground plane on the back side of the metamaterial surfaces, the transmission is blocked, which means the absorptivity can be calculated by

$$A(\omega) = 1 - R(\omega) = 1 - |S_{11}|^2 \tag{5.2}$$

where S_{11} represents the reflection coefficient.

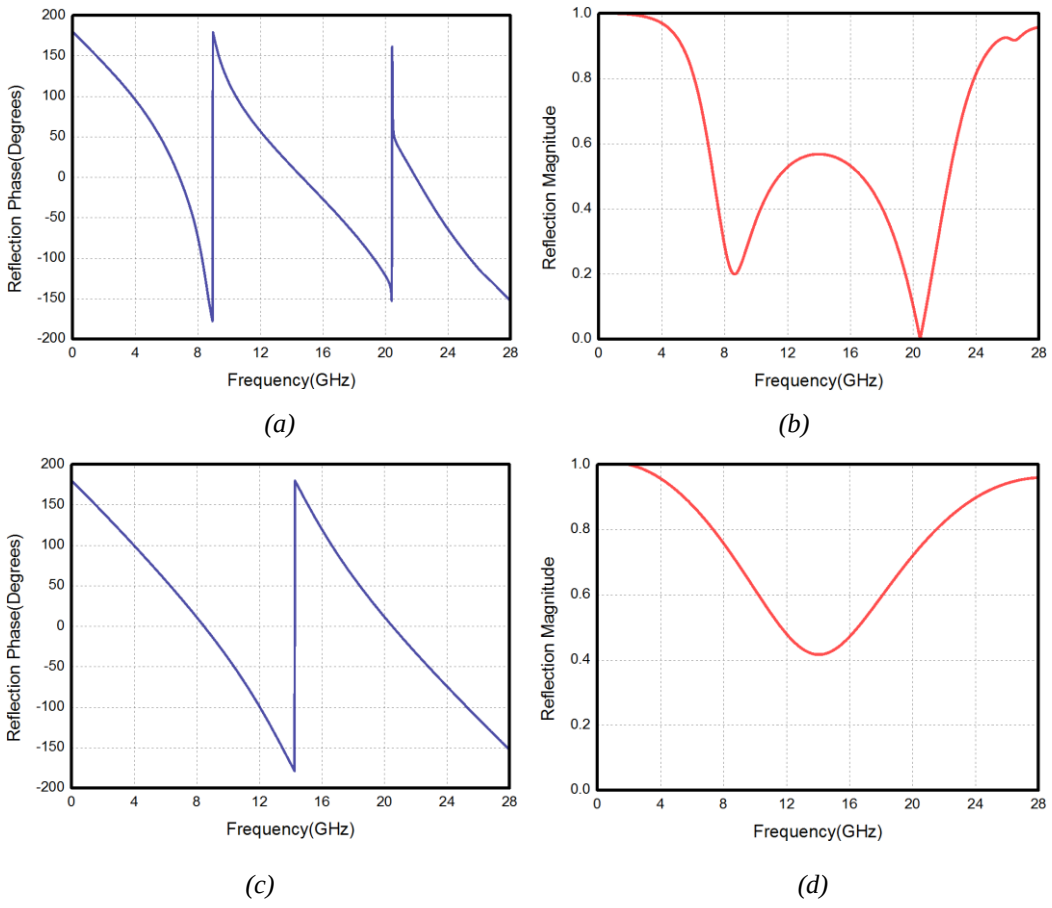

Fig. 5.8 (a) Reflection phase and (b) reflection magnitude of the AMC1 with sheet resistance of 8.7 Ω/sq. (c) Reflection phase and (d) reflection magnitude of the AMC2 with sheet resistance of 98 Ω/sq.

The reflection phase and magnitude of AMC1 (sheet resistance of 8.7 Ω/sq) are shown in Fig.5.8 (a) and (b), respectively. It resonates at 8.6 GHz and 20.4 GHz, with two narrow effective absorption bands. Fig. 5.8 (c) and (d) show that, on the other hand, AMC2 (sheet resistance of 98 Ω/sq) resonates at 14.8 GHz. Apparently, on its own, either AMC1 or AMC2 can absorb incident EM wave in some spectrums, but clearly neither of them can provide any phase cancellation which can lead to a wide-band effective absorption.

To achieve a wide-band effective absorption, AMCs with different sheet resistances and phase characteristics (AMC1 and AMC2) are arranged as 2 × 2 dual AMC lattices to form a functional unit cell (Fig. 5.7 (c)). The functional unit cells are then periodically placed in a chessboard configuration, as displayed in Fig. 5.7 (d). The absorption principle of the chessboard metasurface is based on the anti-phase reflection property. When the phase difference of the reflection coefficients between the two AMC lattices is around 180 °, the reflected fields interfere with each other destructively, which leads to cancellation of reflected waves. According to (5.2), the decrease of reflection magnitude results in the increase of absorptivity. Since the AMC structures consisting of printed graphene rings can be very lossy, the phase cancelling criteria of 180 ° ± 37 ° between two AMCs which was derived for lossless metal patterns with unity reflection magnitude is no longer appropriate for printed graphene surfaces [191]. Thus, a new design methodology or guideline is required based on the unique reflection property of printed graphene AMCs.

Here the concept of standard array theory [192], [211] is used to work out the required phase difference for printed graphene AMCs, which is an approximation approach but useful design guideline. The functional unit cell of the chessboard configuration, consisting of 2 × 2 dual AMC lattices (each lattice has 4 × 4 elementary unit cells), can be modelled as a 2 × 2 array composed of 2 types of lattices. Since the two lattices occupy the same area of the array surface, the incident power is distributed evenly to each other. Suppose that the incident electric field is E_{in} and there is no coupling between them, then the reflected electric field components can be expressed as

$$E_{rf\_1} = \Gamma_1 \cdot E_{in} = A_1 e^{j \cdot P_1} \cdot E_{in} \tag{5.3}$$

$$E_{rf\_2} = \Gamma_2 \cdot E_{in} = A_2 e^{j \cdot P_2} \cdot E_{in} \tag{5.4}$$

where $\Gamma_{1,2}$ represent reflection coefficients ($A_{1,2}$ and $P_{1,2}$ are the magnitudes and phases) of AMC1 and AMC2, respectively.

The total reflected electric field is then given by

$$E_{rf\_tatol} = AF_1 \cdot E_{rf\_1} + AF_2 \cdot E_{rf\_2} \tag{5.5}$$

where $AF_{1,2}$ represent the array factors and can be expressed as [211]

$$AF_i(\theta, \phi) = \sum_{n=1}^{N} W_n e^{jk_0 \sin\theta \cdot (x_n \cos\phi + y_n \sin\phi)} \tag{5.6}$$

where $i = 1\ or\ 2,\ x_n$ and y_n represent the coordinate of the *n*th element, and W_n is its complex excitation coefficient.

In the radar absorber design, infinite periodic structure is assumed and edge effects are neglected. Since two AMC lattices are arranged anti-symmetrically in the functional unit cell hence each of them occupies half area of the chessboard, the array factors from eq. (5.6) can be approximated to be $\frac{1}{2}$ for both AMCs, which means according to eq. (5.5), the reflection coefficient of the absorber surface can be approximated by the average reflection coefficients of two AMC structures [191]

$$S_{11} = \frac{A_1 e^{jP_1} + A_2 e^{jP_2}}{2} \tag{5.7}$$

In order to find the relationship between magnitude difference and required phase difference to achieve effective absorption for two printed graphene AMCs, i.e., lossy AMCs, the magnitude and phase differences between the two lossy AMCs based on the numerically simulated reflection coefficients of the individual AMC lattices were calculated and displayed in Fig. 5.9 (a) and (b), respectively.

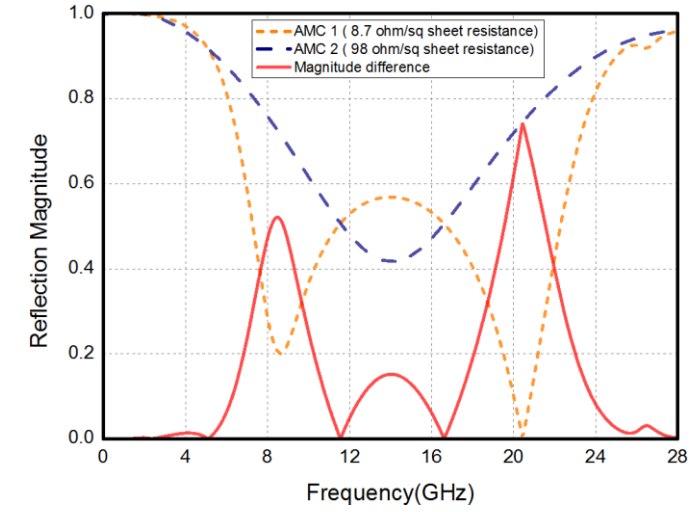

(a)

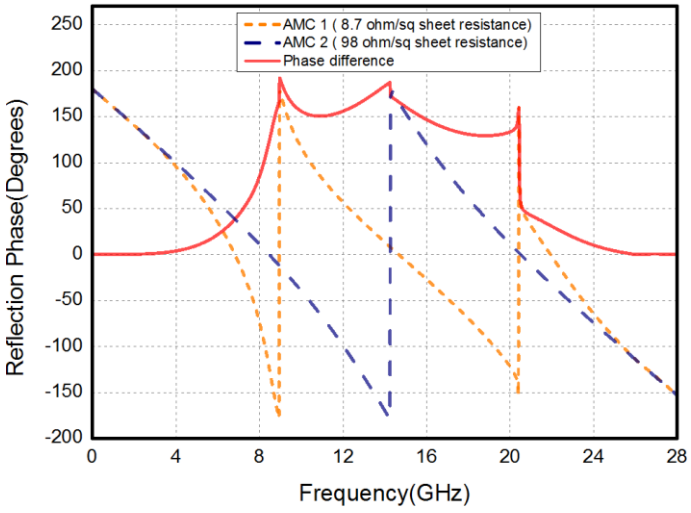

(b)

Fig. 5.9 (a) Reflection magnitudes of two lossy AMC lattices and the difference between them. (b) Reflection phases of two lossy AMC lattices and the difference between them.

5.2.3 Analysis of required reflection phase difference between two printed graphene AMCs

Since the effective absorption needed by a radar absorber is higher than 90%, we combine (5.2) and (5.7) and obtain the required absorption as,

$$A(\omega) = 1 - \frac{1}{4}\left[{A_1}^2 + {A_2}^2 + 2A_1A_2\cos(P_1 - P_2)\right] > 90\% \tag{5.8}$$

By calculating this inequality in MATLAB with the reflection magnitudes A_1 and A_2 obtained from CST full wave numerical simulation, the required phase difference $|P_1 - P_2|$ can be obtained and illustrated in Fig. 5.10.

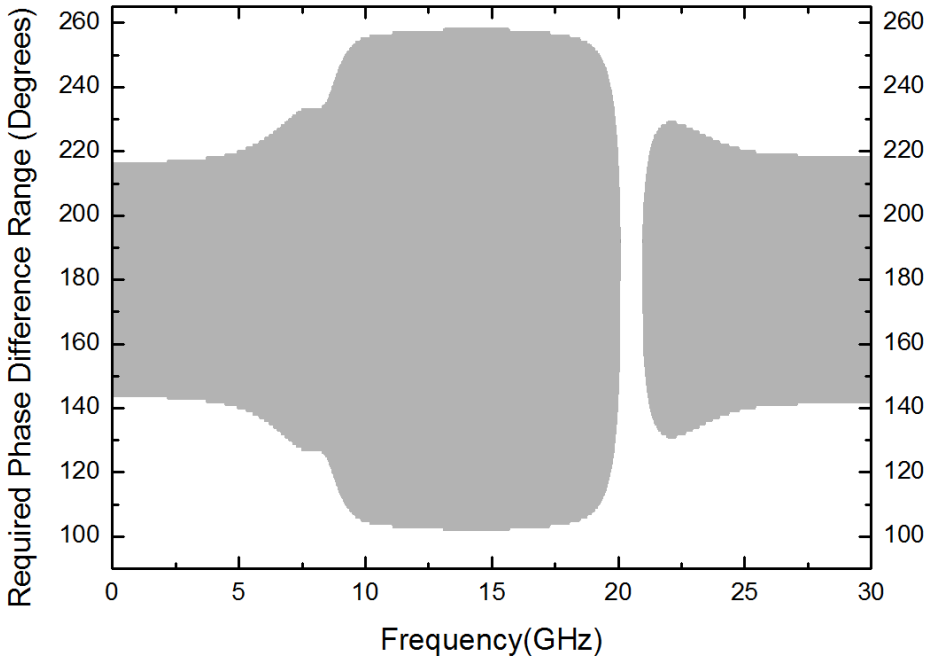

Fig. 5.10 The required phase difference range calculated through (5.8) with simulated reflection magnitudes to achieve 90% absorption.

In Fig. 5.10, the gray shaded area represents the region of phase differences that satisfy the requirement to achieve more than 90% absorption. It can be seen that the required phase difference changes over frequency. From 0 GHz to 5 GHz, due to the reflection magnitudes of the two AMC lattices are near unity, the required phase difference is around $180° \pm 37°$, which is consistent with that of metal AMC surfaces. From 5 GHz to 9.5 GHz, the reflection magnitudes of the AMC lattices as well as the difference between them change rapidly over frequency (as shown in Fig. 5.9 (a)), which lead to the steep edge of the gray shaded region. From 9.5 GHz to 19 GHz, the required phase difference is around $180° \pm 78°$, which has a broader range comparing with that of metal surfaces. This is because the absorption of printed graphene radar absorber counts on not only the cancellation effect of reflections due to the phase difference, but also the absorption of graphene AMC lattices. From 20 GHz to 21 GHz, there is a gap on the

required phase difference, which means no such values can satisfy (5.8). In other words, for the two presented AMCs with fixed dimensions and chosen sheet resistances, the effective absorption (>90%) cannot be achieved within this frequency range no matter how. This gap is caused by the large reflection magnitude difference between the two AMCs.

To further illustrate the effect of the reflection magnitude difference between two AMC lattices, an extreme condition that the two AMC lattices have absolutely opposite reflections can be considered, which means the phase difference is 180 °. Then (5.8) can be simplified as,

$$A(\omega) = 1 - \left|\frac{A_1 - A_2}{2}\right|^2 > 90\% \tag{5.9}$$

According to (5.9), when the magnitude difference $|A_1 - A_2|$ is 0.632, the absorption is 90%. When the magnitude difference $|A_1 - A_2|$ is greater than 0.632, the effective absorption cannot be achieved even with an absolutely opposite reflection phases. In Fig. 5.9 (a), it can be seen from the red solid line that the magnitude difference is greater than 0.632 from 20 GHz to 21 GHz, which leads to the gap in Fig.5.10.

5.3 Numerically Simulated Absorption Performance

Comparing the phase difference (red solid line) in Fig. 5.9 (b) with the required phase difference range (gray area) in Fig. 5.10, the phase difference between the two AMC lattices satisfies the requirement from 8.5 GHz to 19.8 GHz, which means the effective absorption can be obtained within this frequency band. As shown in Fig. 5.11, the simulated radar absorption at normal incident (the red line) indicates the proposed radar absorber can achieve a wide bandwidth from 7.94 GHz to 19.35 GHz. The discrepancies are due to the fact that the simulation results in Fig. 5.11 are based on the functional unit cell (2 × 2 dual AMC lattices, Fig. 5.7 (c)), whereas the results in Fig. 5.10 are based on two elementary unit cells of AMCs. The former has taken into account of mutual coupling between the different AMC lattices and the elementary unit cells, while the latter has only simulated coupling between the elementary unit cells.

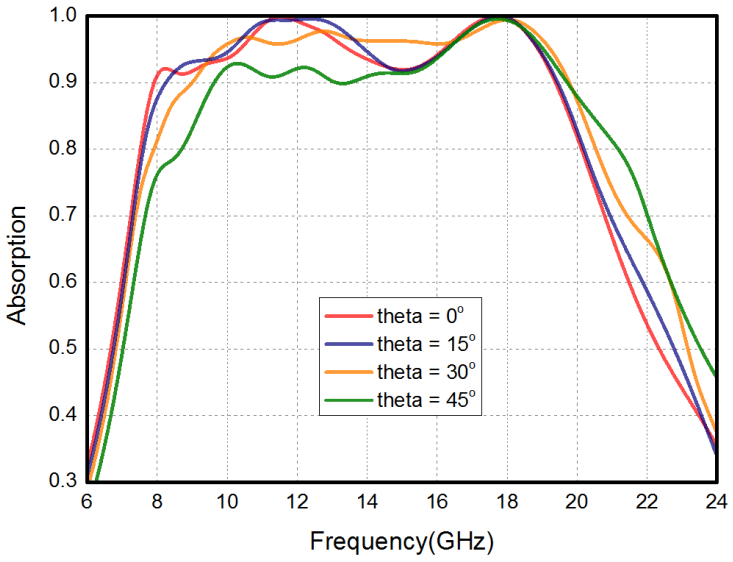

(a)

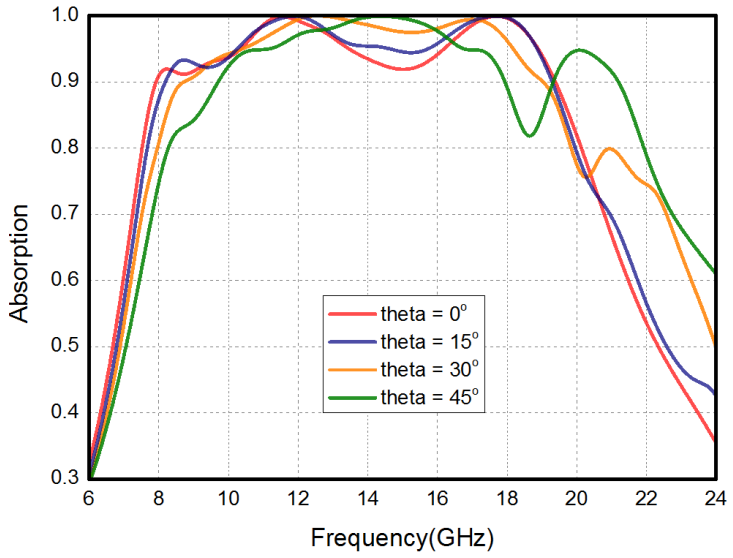

(b)

Fig. 5.11 (a) Simulated absorption at incident angles of 0 °, 15 °, 30 ° and 45 ° for the TE radiation and (b) TM radiation.

Radar absorbers with lossless AMC structures depend strictly on phase difference, therefore normally cannot provide wide bandwidth, especially when the incident angle becomes large [182], [183], [184]. To investigate the performances at various incident angles, the effective absorption bandwidth at different incident angles for transverse electric (TE) and transverse magnetic (TM) waves have been studied numerically, and the results are displayed in Fig. 5.11 (a) and (b), respectively. The data indicate that for both TE and TM waves, the absorption and bandwidth decrease gently as the incident angle increases from 0 ° to 45 °. Generally, unlike metal AMCs

chessboard absorbers, the printed graphene absorber shows comparatively good performance at wide incident angles for both TE and TM waves. A comparison of relative effective absorption bandwidth at normal and 30 ° incident angles for TE wave between the proposed radar absorber and other known wideband AMC chessboard ones is presented in Table 5.1.

Table 5.1 Comparison of Relative Effective Bandwidth (BW) at Normal and 30 ° Incident Angles for TE Wave between this Work and other Wideband AMC Chessboard Designs.

Reference	Relative effective BW (%) at normal incident	Relative effective BW (%) at 30 ° incident	Number of AMC types in the chessboard
[182]	40.2%	20%	2
[183]	63%	45%	2
[184]	91%	43%	4
This work	83.5%	77.3%	2

5.4 Fabrication of Printable and Flexible AMC Based Radar Absorber

The graphene absorber with overall dimension of 210 mm × 240 mm using home-made graphene ink was printed to experimentally demonstrate the simulation results. Limited by the screen printer, it is difficult to print two AMCs with different sheet resistances on the same paper. The two types of AMC lattices with sheet resistances of 98 Ω/sq and 8.7 Ω/sq (Sample 2 and Sample 3 in Fig. 5.2 and Fig. 5.3) were printed separately on normal A4 sized paper. The photo of printing screen used in fabrication is shown in Fig. 5.12 (a). This printing screen was patterned with capillary film (ULANO, EZ50-Orange) and could be used to print two AMC lattices each time. Since the dimension of the ring is too thin for 4-point probe station to measure, rectangles with dimension of 8 mm × 25 mm around the lattices were printed for sheet resistance measurement. The AMC lattices with desired sheet resistances were then cut out (as shown in Fig. 5.12 (b)) and spliced on silicone substrate with adhesive, arranged in chessboard configuration as designed. A thin copper plane with the same size of chessboard surface was placed at the back of the silicone substrate as ground. Fig. 5.12 (c) displays the printed graphene radar absorber.

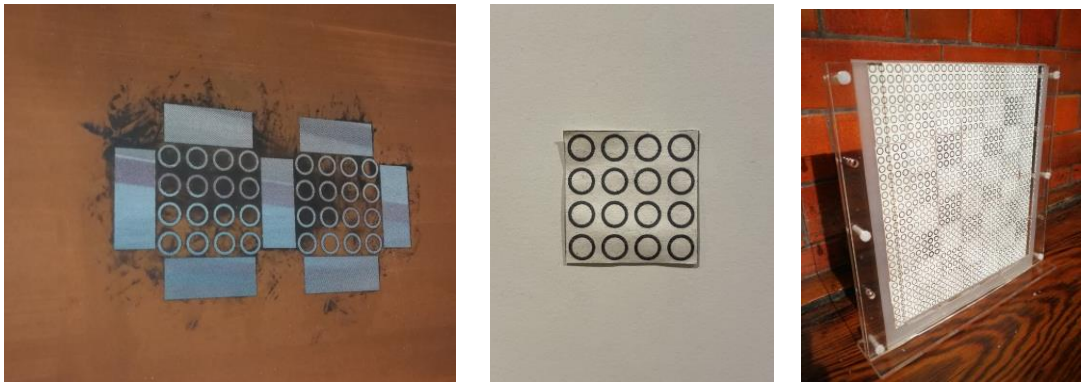

(a) *(b)* *(c)*

Fig. 5.12 (a) The printing screen patterned with capillary film (ULANO, EZ50-Orange). (b) Graphene printed unit AMC lattice sample. (c) Photo of the printed graphene AMC radar absorber.

5.5 Experimental Demonstrations of Absorption Performance and Flexibility

The printed graphene absorber was measured in the anechoic chamber with the experimental setup as displayed in Fig. 5.13. Two horn antennas (Aaronia AG, PowerLOG 70180) with frequency range of 700MHz – 18 GHz were connected to the HP8510 vector network analyzer (VNA) as transmitter and receiver, respectively. To obtain a 20 dBm source power from the VNA, power amplifier (5.9 – 18 GHz, Mini-Circuits, ZVE-3W-183+) was used during the measurement. The time gating function in the VNA was applied to eliminate the noise and the interference between the two horn antennas during the measurement.

In the measurement setup, a pair of horn antennas working as transmitter/receiver was connected to HP8510 VNA to measure the reflection from the sample. The sample and the antennas were supported by two height adjustable stands to make sure they were at the same height. According to the far field region formula $2 \times D^2/\lambda$, with the antenna dimension (D) of 17.5 cm and the highest measured frequency of 18 GHz, the required measurement distance for far field should be 3.675 m. Therefore, the sample was placed vertically and 1.9 m away from the antennas for normal incident case, and in this way the distance between the transmitter and the receiver was 3.8 m, which satisfied the far field measurement distance. For various incident angles measurement, one more stand was required, and a thick cotton string with a chalk tied on one end of it was used to draw an arc on the ground and mark specific locations for the

transmitter and receiver according to different measured incident angles. As illustrated by the schematic diagram in Fig. 5.13 (b), the cotton string was fixed to the bottom center of the stand used to support the sample, and a chalk was tied on the other end of it. The length of the cotton string between the stand bottom center and the chalk was kept to 1.9 m. With the stand bottom center as circle center and the cotton string as radius, a circular arc was draw by the chalk and the specific incident angles with accordingly reflective angles were marked on the arc for the transmitter and receiver. The full 2-port measurement calibration model, which could provide best magnitude and phase measurement accuracy in HP8510 but require measurement of all four S-paramenters of the two-port device, was chosen for the measurement, and a thru, an open circuit, a short circuit, and a sliding load were used to calibrate at Port 1 and Port 2. The HP8510 gating feature in the time domain measurement function was used to remove noise, unwanted mismatches, and responses of multiple transmission paths to provide smoother trace in the frequency domain plot.

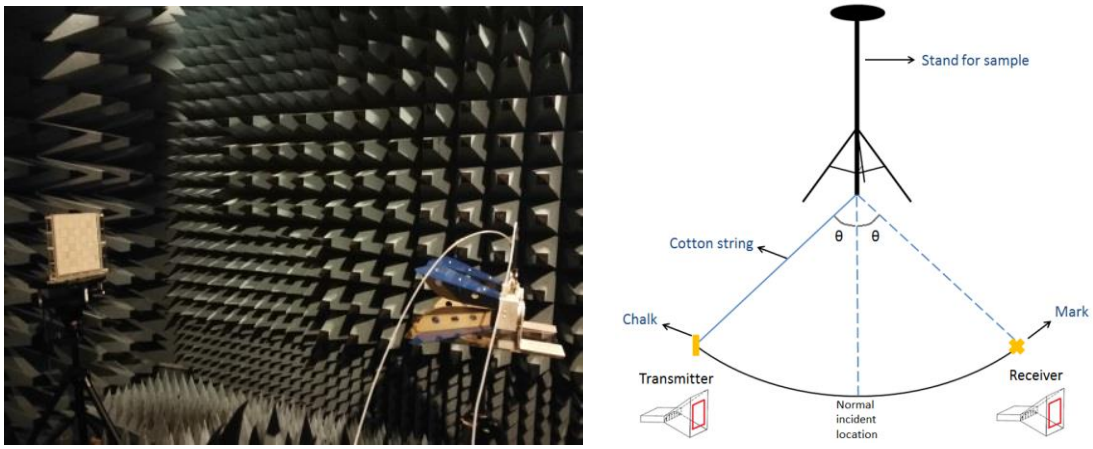

(a) *(b)*

Fig. 5.13 (a) Measurement setup in the anechoic chamber. (b) Schematic diagram for specific incident angle (θ) measurement.

The experimental results at normal incident are displayed in Fig. 5.14 (a) and (b). Due to the limitations of the experimental conditions, the measurement is conducted only in the range of 6 − 18 GHz. Fig. 5.14 (a) shows the measured reflection coefficient between two horn antennas for three cases (copper PCB board, silicone substrate attached on the copper PCB board with blank A4 paper and adhesive on it, printed graphene radar absorber).

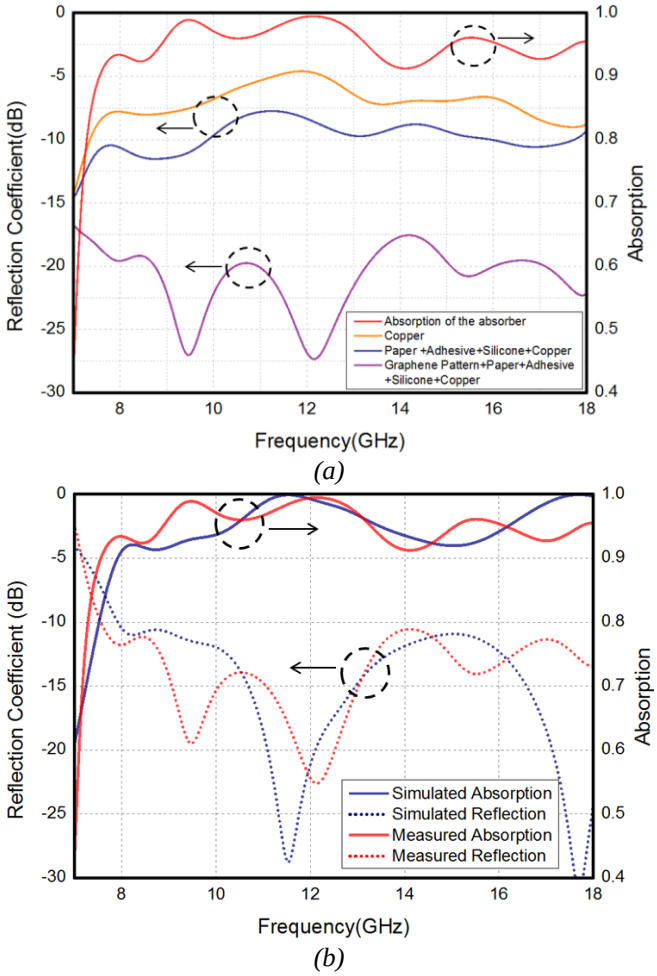

Fig. 5.14 (a) Reflection coefficient comparison of different samples and absorption of the absorber in measurement. (b) Comparison of simulation results and measurement results for normal incidence.

From Fig. 5.14 (a), it can be seen that the reflection coefficient of the printed graphene radar absorber is much lower than that of the other two cases, demonstrating high EM absorption of the absorber under normal incident. From Fig. 5.14 (b), it can be seen that within the measured frequency range, the radar absorber has an impressive performance with an effective absorption from 7.58 GHz to 18 GHz. The simulated data are in reasonably good agreement with the measured although discrepancy can be observed. There could be various reasons that have caused the discrepancy, such as, the variation of the printed sheet resistance deviations, geometric variation of the absorber, uneven surface due to adhesive between the paper and silicone substrates and etc.

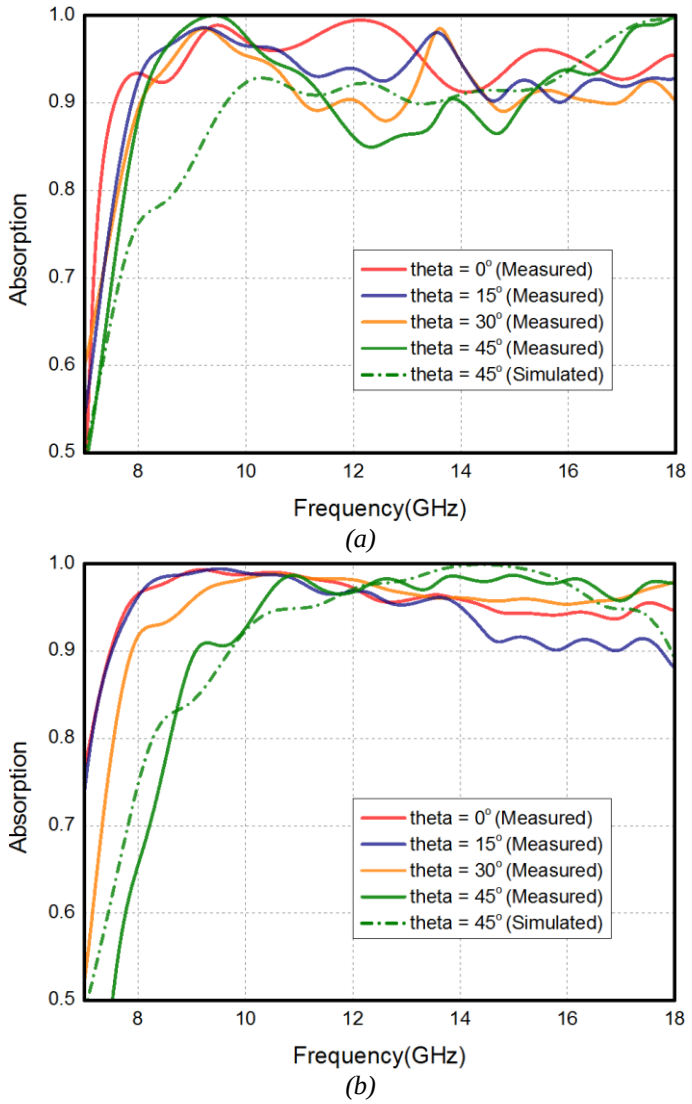

Fig. 5.15 (a) Measured absorption at incident angles of 0 °, 15 °, 30 ° and 45 °, with simulated absorption at 45 ° for the TE incidence and (b) TM incidence.

To further investigate the absorber performance, the absorption at 0 °, 15 °, 30 °, and 45 ° incident angles for TE and TM modes were measured and illustrated in Fig. 5.15 (a) and (b), together with the comparison between measured and simulated results at 45 °. For both TE and TM waves, when the incident angle increases up to 45°, the absorber can still provide >85% absorption within the measured frequency range. The results indicate a very good absorption performance at wide incident angles.

Fig. 5.16 Two bending cases with bending angular of 148 °and 200 °, respectively.

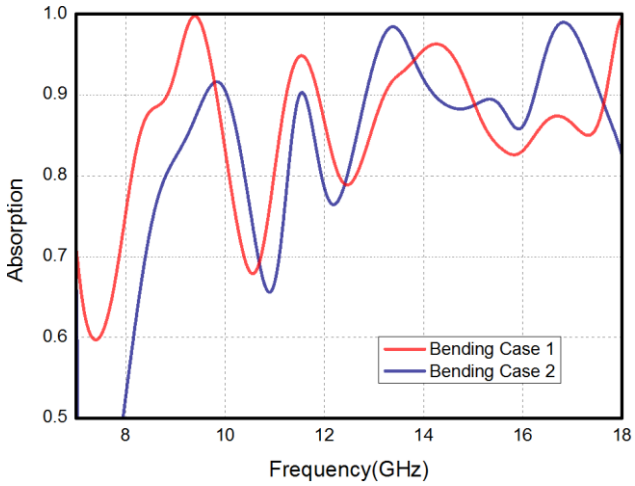

Fig. 5.17 Measured absorption results for different bending cases.

Measurements for two different bending cases were carried out to investigate the effects of bending of the absorber. The cylinders used in the measurement were wrapped up by foils and have different circumferences of 583 mm and 432 mm, respectively. During measurement, the transmission coefficient of the cylinder wrapped by foils was measured first. Then the printed graphene radar absorber was attached to the cylinder wrapped by foils to be measured, as shown in Fig. 5.16. According to the circumferences of the cylinders, two bending cases have bending angle of 148 ° and 200 °, respectively. The measurement results are illustrated in Fig. 5.17. The absorber in bending case 1 (bending angle of 148 °) provides four effective absorption peaks located at 9.4 GHz, 11.5 GHz, 14.3 GHz, and 18 GHz, respectively, whereas in bending case 2 (bending angle of 200 °), the absorber can still achieve four effective absorption peaks at 9.8 GHz, 11.5 GHz, 13.3 GHz, and 16.8 GHz, respectively. The measurement results demonstrate that even

though a single wideband effective absorption (> 90%) cannot be provided in these two bending cases, the printed graphene radar absorber can still achieve absorption greater than 70% within most parts of the spectrum from 8 GHz to 18 GHz and greater than 90% in some discrete bands.

5.6 Investigation of the Discrepancy between Simulation and Experimental Results

To understand the causes of the discrepancy, uneven distribution of adhesive used to fix the paper on top of silicone substrate and geometric variation are further investigated. Fig. 5.18 (a) illustrates a kind of air layer induced by the uneven distribution of adhesive. The fabrication deviations in dimensions of AMC lattices vary randomly. The inner diameter of the circular rings is measured to be around 4.7 ± 0.1 mm, while the outer diameter is around 6.12 ± 0.12 mm, such as the one shown in Fig. 5.18 (b), which should be 6 mm according to the design. The compressing procedure is the main reason which leads to the wider circular rings in fabrication sample.

(a) *(b)*

Fig. 5.18 (a) The air layer (surrounded by red dash line) due to the uneven distribution of adhesive. (b) Measured diameter of circular ring on the fabricated sample.

A better match between the simulation results and measurement results is tried to be dug out by varying the values of different parameters in simulation. However, even one or two valleys or peaks (of the simulation and measurement results) can be better matched separately by modifying certain parameters of the unit cell model; it is difficult to match all valleys and peaks at the same time. This is because the fabrication deviations are not unified or periodic while the functional

unit cell model in simulation is periodic. It's hard to simulate those complex and random deviations with periodic unit cells.

Four parameters of the model are mainly considered. The first one is the diameter of circular rings as mentioned previously. The compressing procedure is the main reason which leads to the wider circular rings in fabrication. The second one is the thickness of silicone substrate (with a tolerance allowance given by POLYMAX is $\pm$ 0.3 mm [212]), which is about 3 $\pm$ 0.15 mm according to the measurement. The thickness of the silicone substrate is thicker than 3 mm at the outside edges and thinner than 3 mm at the middle part. The third one is the sheet resistance of graphene patterns, which are about 8.7 $\pm$ 0.7 Ω/sq and 98 $\pm$ 5 Ω/sq for two AMCs. The fourth one is the air gap induced by the uneven distribution of adhesive, as shown in Fig. 5.18 (a).

The detailed investigation of parameters is introduced in the following paragraph according to the simulation results in Fig. 5.19 (with the matched valleys or peaks marked in circle). The parameter modifications are summarized in Table 5.2 (with the modifications highlighted).

For Fig. 5.19 (a), the outer diameter is modified to 6.2 mm, and the sheet resistance of AMC1 is modified to 9.5 Ω/sq. It can be seen that the low frequency boundary of -10 dB bandwidth is matched at about 7.6 GHz.

For Fig. 5.19 (b), the sheet resistances are modified to 8 Ω/sq and 103 Ω/sq, respectively. The thickness of silicone substrate is modified to 2.85 mm. A 0.1 mm air layer is added to one AMC1 lattice in the functional unit cell. Compared with the original one, the modified simulation has a better match in the absorption peak at around 12 GHz.

For Fig. 5.19 (c), the outer diameter is 6.2 mm; with the sheet resistance of AMC1 is 8 Ω/sq and the thickness of silicone substrate is 2.85 mm. An air layer is added to one AMC1 lattice. As the air layer becomes thicker, two absorption peaks appear at about 8.5 GHz and 15.6 GHz, which might lead to the two more absorption peaks in measurement results.

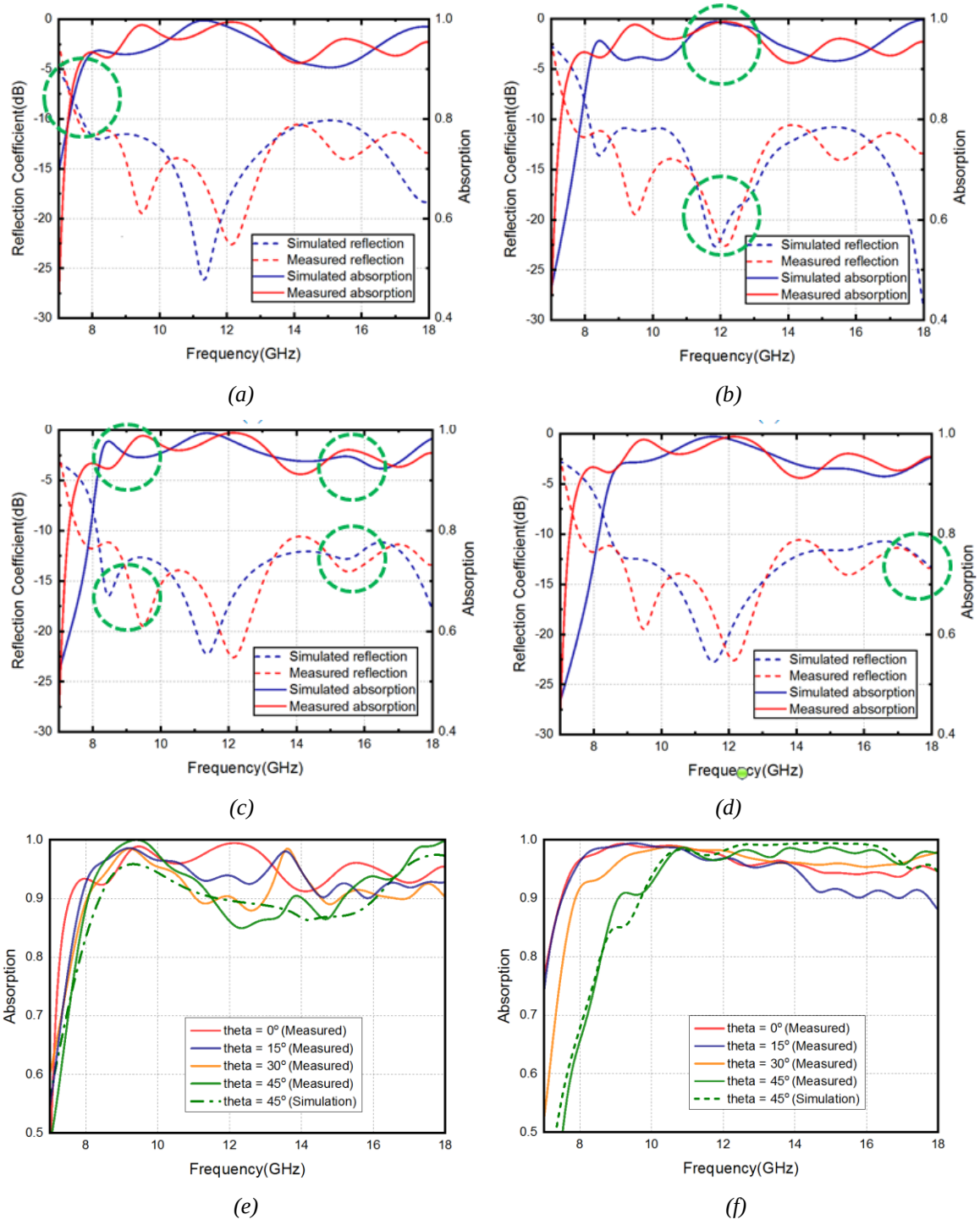

Fig. 5.19 (a)–(d) Comparison of measurement results and simulation results with different modified parameters. (e) Measured absorption at various incident angles, with simulated absorption at 45 ° for TE Mode and (f) TM Mode.

For Fig. 5.19 (d), the inner diameter is 4.6 mm, while the thickness of silicone substrate is modified to 2.85 mm. An air layer of 0.3 mm is added to one of AMC1 lattice and one of AMC2 lattice. It is clear that the results match better at 18GHz with absorption of 95%.

For Fig. 5.19 (e), the inner diameter is 4.6 mm, the outer one is 6.2 mm, and the thickness of silicone substrate is 3.1 mm. For Fig. 5.19 (f), the outer diameter is 6.2 mm, the thickness of substrate is 2.85 mm, and a thicker air layer is added to one of AMC1 lattices. With these modifications, the TE mode and TM mode results achieve better matches, respectively.

Table 5.2 Summarized Parameter Modifications According to Different Simulation Results Displayed in Fig.5.19.

	Inner diameter (mm)	Outer diameter (mm)	Sheet resistance of AMC1 (Ω/sq)	Sheet resistance of AMC2 (Ω/sq)	Thickness of silicone (mm)	Air layer added to AMC1	Air layer added to AMC2
Original	4.8	6	8.7	98	3	No	No
Fig. 2. (a)	4.8	6.2	9.5	98	3	No	No
Fig. 2. (b)	4.8	6	8	103	2.85	Yes	No
Fig. 2. (c)	4.8	6.2	8	98	2.85	Yes	No
Fig. 2. (d)	4.6	6	8.7	98	2.85	Yes	Yes
Fig. 2. (e)	4.6	6.2	8.7	98	3.1	No	No
Fig. 2. (f)	4.8	6.2	8.7	98	2.85	Yes	No

5.7 Chapter Summary

In this chapter, novel graphene AMC radar absorber with specific sheet resistances is designed and screen printed. By properly arranging two printed graphene AMC lattices in a chessboard configuration and controlling the sheet resistances of the patterns, a desirable printed graphene radar absorber is obtained, which has achieved broad effective absorption bandwidth. The absorption mechanism of this new approach relies not only on the reflection cancellation between two AMCs but also on the absorption of the printed graphene patterns. The relationship between reflection magnitude difference and required phase difference of the two AMC lattices to achieve effective absorption has also been investigated thoroughly.

Both simulation and measurement results indicate that the absorption frequency band covers X band (8 – 12 GHz) and K_u band (12 – 18 GHz). Meanwhile, unlike other previously reported

AMC based absorbers, the absorber in this work is much less sensitive to incident angles and performs well under various incident angles for both TE and TM waves.

The printed graphene radar absorber also has reasonably good mechanical flexibility and can still provide greater than 70% absorption within most parts of the X and K_u bands in two bending cases. In a word, not only novel screen printed graphene radar absorber based on phase cancellation as well as absorption has been achieved, but new methodology of radar absorber designs applying dual lossy AMCs with different sheet resistances has also been demonstrated analytically, numerically and experimentally. This approach could have a wider application as it has provided more degree of freedom in radar absorber designs, i.e., not only the unit cell shapes but also the sheet resistances of the shapes can play a significant part in the design metric.

Chapter 6: Optimization of AMC Based Coding Metamaterial Absorbers: Genetic Algorithm

In Chapter 5, a printed graphene AMC based flexible and broadband radar absorber is designed, investigated and experimentally demonstrated. In this chapter, the printed graphene AMC based radar absorber will be further investigated and optimized through genetic algorithm to obtain a broader absorption bandwidth. The previous design is based on the functional unit cell composed of 2×2 AMC lattices which are arranged in the chessboard configuration. The two AMCs (with 8.7 Ω/sq and 98 Ω/sq) occupy the same area of the surface, with incident power distributed evenly to each other. In order to find a better solution, a novel functional unit cell is required. Therefore, the AMC based coding metamaterial absorbers with novel functional unit cells are introduced. Within the novel functional unit cells, the previously mentioned distribution of AMCs is disturbed. AMCs with different sheet resistances are re-arranged in the chessboard configuration according to genetic algorithm, and different AMCs no longer occupy the same area of the surface.

6.1 The Genetic Algorithm Program Outline

To begin with, a functional unit cell with relatively smaller size is chosen to be optimized. Since the previously designed distribution of AMCs needs to be disturbed, the AMC lattices are no longer required. As shown in Fig. 6.1, the new functional unit cell is made out of 4×4 arrays, which are exactly 4×4 elementary unit cells. The unit cell design stays unchanged as the one in Fig. 5.7 (a). The sheet resistances of two AMCs remain to be 8.7 Ω/sq and 98 Ω/sq, respectively.

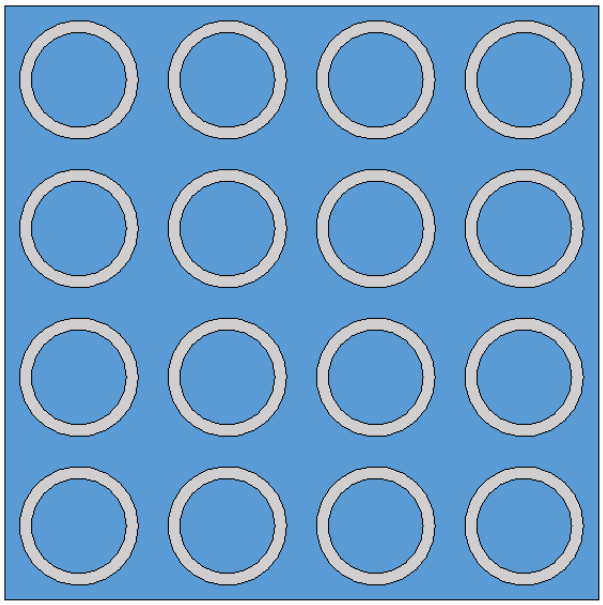

Fig. 6.1 Schematic of functional unit cell with 4 × 4 arrays of elementary unit cells.

The general outline of the genetic algorithm program for this optimization is illustrated through the flow chart in Fig. 6.2. The program begins by randomly generating a series of DNA sequence which defines the genetic code of the functional unit cell. Each DNA sequence represents an individual and consists of a string of 0 and 1, created by the pseudorandom scalar integer generation function in MATLAB. The length of the string is 16 bits, which means every sequence contains 16 DNA, representing the 16 elementary unit cells. The size of population is set to be 30, which means 30 randomly generated 16-bit DNA sequences form the original generation. After the initialization, the program triggers CST and manipulates it to open the target file, in which the structure contains the designed functional unit cell. Then CST can set the values of sheet resistances of 16 circular rings one by one according to the previously generated DNA sequence (DNA with a binary 0 will be converted into 8.7 Ω/sq while DNA with a binary 1 will be converted into 98 Ω/sq). Once a 16-bit sequence is read completely, CST updates the structure and runs the simulation. The absorption is calculated in CST through S_{11} and the results are exported as .txt file which can be read and analyzed by MATLAB. The program in MATLAB uses the results to calculate the effective absorption bandwidth and stores the value of bandwidth into a two-dimensional array. The two-dimensional array defines a 20-by-30 matrix, representing

the 20 generations with each generation containing 30 individuals (the population size). The matrix can be used to store the bandwidth provided by every individual. After 30 sequences are simulated, the best individual with broadest absorption bandwidth in this generation will be selected and compared with 11.41 GHz.

The absorption bandwidth reference of 11.41 GHz is given by the design in Chapter 5. Once the program finds an individual with the DNA sequence which can provide an absorption bandwidth larger than 11.41 GHz, the termination condition is reached and the program will end. However, it was found this termination condition can be achieved easily during the program testing. Therefore, the termination condition was changed to be 20 generations to search for a better solution. The program will not end until the original population completes the 20 generations' evolution.

Back to the flow chart, the 30 individuals will then be evaluated according to the fitness function. The values of effective absorption bandwidth of 30 individuals are used as weights for selection. In this way, the individuals with broader absorption bandwidth are more likely to be selected as parents. The size of parents remains the same as original population size, meaning the "parents" are still made up of 30 DNA sequences. 3 copies (10% of the population size) of the previously selected best individual's DNA sequence are added into parents group and replace the first three individuals in parents. Then the crossover process takes place in parents. For each individual as "mother", another individual is randomly selected from parents to be the "father". The crossover points between "mother" and "father" are randomly generated 16-bit one-dimensional array containing zeros and ones. For each bit in the DNA sequence of "child", if the value reads 1, the corresponding DNA from "mother" will be selected; otherwise it will be the one from "father". After the "child" is built up, it will be mutated. During testing, it was found that a lower mutation rate might have a better effect. Hence, the mutation rate in this program is set to be 2%. The crossover and mutation are repeated for 30 times to build 30 children which are used to form the next generation.

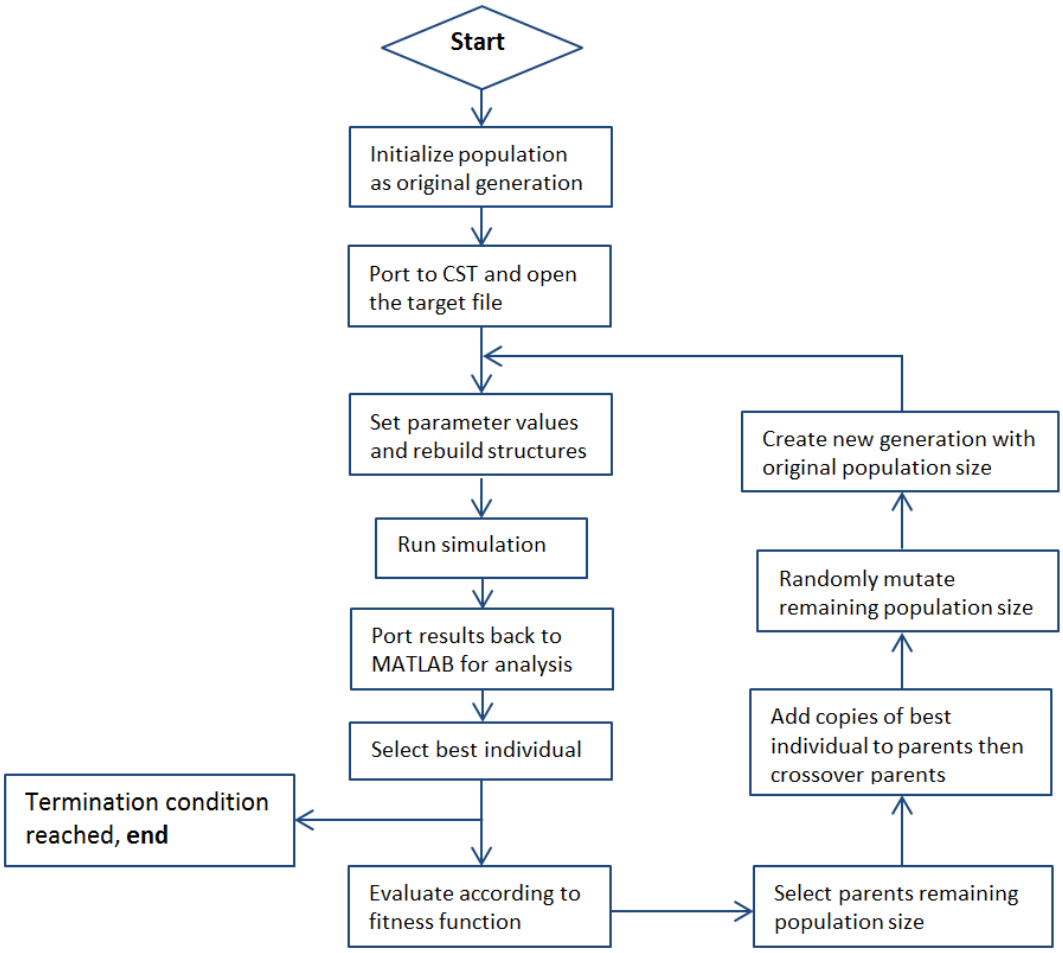

Fig. 6.2 Flow chart detailing Genetic Algorithm run procedure.

6.2 Comparison of Absorption Bandwidth in Different Generations

When designing a genetic algorithm program, there are a lot of details have to be considered; how large a population to use, what is the value of crossover rate or mutation rate; how to set an appropriate termination condition. Since the purpose of this program is to optimize the absorption bandwidth of the AMC based absorber introduced in Chapter 5, the original termination condition of this program was the achievement of an absorption bandwidth lager than 11.41 GHz (the simulation results of the AMC based absorber in Chapter 5). After testing the program, it was found this termination condition can be achieved within no more than 10 generations, with the solution providing an absorption bandwidth ranging from 11.4 GHz to 11.8 GHz. To investigate whether this program can give a better solution with broader absorption bandwidth or not, the

termination condition is set according to the evolution generations. The program will end automatically after the targeted evolution generation.

To begin with, the number of generation is set to be 10. Fig. 6.3 illustrates the structure which has the DNA sequence of the best individual in the 10th generation, along with the absorption results provided by this generated structure. The 16 elementary unit cells in the functional unit cell are numbered from left to right and top to bottom. The number of each elementary unit cell corresponds to the bit position of the DNA sequence. The value of the bit corresponds to the sheet resistances, with "0" representing 8.7 Ω/sq and "1" representing 98 Ω/sq. In this way, the distribution of the different elementary unit cells can be translated from the DNA sequence map (Fig. 6.3 (c)) of the best individual given in Table 6.1. From Fig. 6.3 (b), the effective absorption bandwidth is 11.825 GHz (from 8.75 GHz to 20.575 GHz).

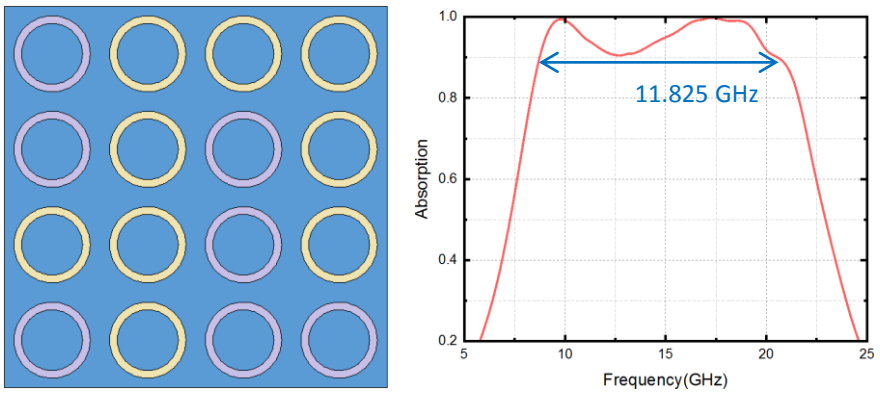

(a) *(b)*

1	0	0	0
1	0	1	0
0	0	1	0
1	0	1	1

98	8.7	8.7	8.7
98	8.7	98	8.7
8.7	8.7	98	8.7
98	8.7	98	98

(c) *(d)*

Fig. 6.3 (a) Schematic of generated functional unit cell after 10th evolution generation (rings in gold have sheet resistance of 8.7 Ω/sq while rings in lilac have sheet resistance of 98 Ω/sq). (b) The numerically simulated absorption results of the generated structure. (c) The DNA sequence map of the best individual in 10th generation. (d) The translated distribution of different elementary unit cells.

Table 6.1 DNA Sequence of the Best Individual in the 10th Evolution Generation.

Bit Position	1	2	3	4	5	6	7	8	9	10	11	12	13	14	15	16
Bit Value	1	0	0	0	1	0	1	0	0	0	1	0	1	0	1	1

The number of generation is then set to be 20 for the termination condition for further investigation. The generated DNA sequence map of the best individual in 20th generation and the correspondingly converted structure schematic are displayed in Fig. 6.4. From the DNA sequence map, there are three different bits compared with the one of 10th generation, locating at the 1st, 5th, and 14th elementary unit cell. The arrangement of the elementary unit cells translated from this DNA sequence provides a broader effective absorption bandwidth of 12.375 GHz, ranging from 8.45 GHz to 20.825 GHz, with a relative absorption bandwidth of 84.5%, which is increased comparing with the functional unit cell design with evenly distributed AMCs which has an effective absorption bandwidth of 11.41 GHz and a relative absorption bandwidth of 83.5%.

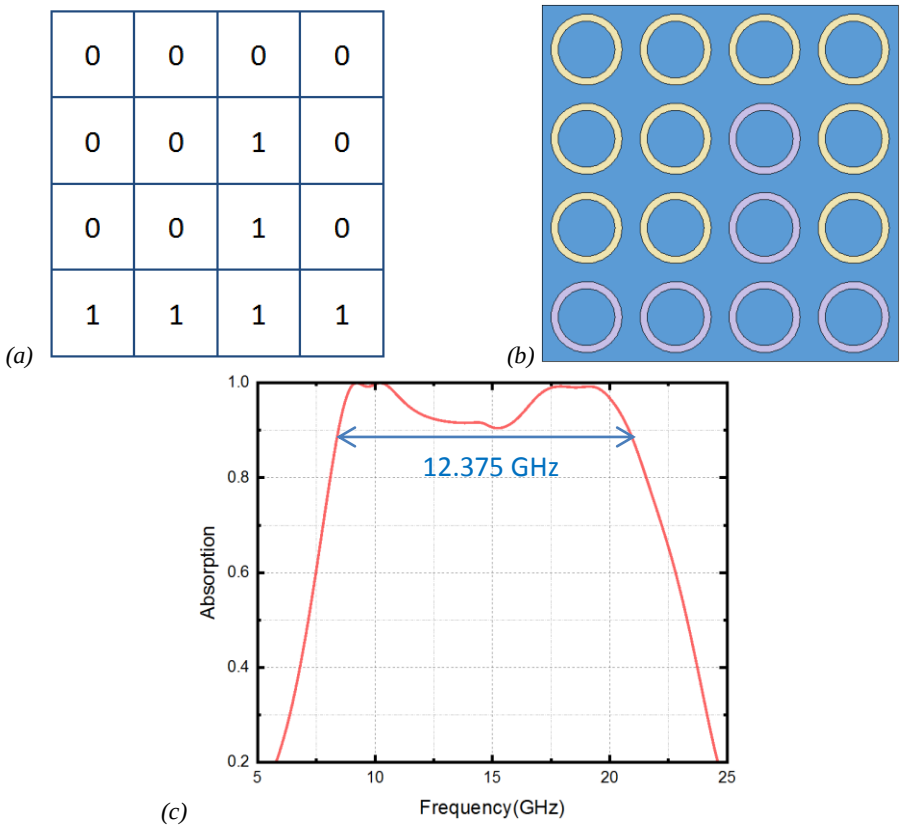

Fig. 6.4 (a) The DNA sequence map of the best individual in 20th generation. (b) Schematic of generated functional unit cell (rings in gold have sheet resistance of 8.7 Ω/sq while rings in lilac have sheet resistance of 98 Ω/sq). (c) The simulated absorption results of the generated structure.

In order to better understand the evolutionary process, the values of effective absorption bandwidth achieved by all individuals from the 1st, 2nd, 7th, 13th, and 20th generations are recorded and displayed in Table 6.2, with top three best individuals are highlighted in red and worst three individuals are highlighted in green for each generation. Through comparing the top three best individuals over these generations, it can be seen that the individuals of best fitness in each generation are well reserved as the first three individuals in the next generation. Based on this precondition, individuals with better fitness (which means broader absorption bandwidth) are produced from generation to generation through the evolution. For example, the first and second individuals in the 7th generation indicate the best solution from the 6th generation could provide an absorption bandwidth of 11.45 GHz. Hence the third individual should also have 11.45 GHz bandwidth before evolution. However, the third one in fact provides a wider bandwidth of 11.525 GHz, which means the crossover and mutation processes result in a good evolution and build a better individual. The same situation arises in the 13th generation with two kinds of good evolution cases leading to a wider bandwidth of 12.375 GHz and 11.825 GHz, respectively. In conclusion, the increasing of evolution generations can lead to better individuals with broader absorption bandwidth. However, as the number of evolution generation increases to 20, no one can exceed the absorption bandwidth of 12.375 GHz. On the other hand, the individuals with bandwidth of 12.375 GHz increase in number as generation evolves. The individual with bandwidth of 12.375 GHz first arises in the 13th generation, and there is only one individual could provide this wide bandwidth, while in the 20th generation most individuals can provide the bandwidth of 12.375 GHz, which indicates the program is converging on this solution.

Additionally, the worst 3 individuals in the selected 5 generations are highlighted in green for comparison. From the 1st to the 13th generation, it can be seen from Table 6.2 that the individuals with narrow absorption bandwidth are dying out. The worst solution of the 1st generation is 0.05 GHz, while it is 8.25 GHz for the 2nd generation; 9.175 GHz for the 7th generation; and 9.525 GHz for the 13th generation. This trend of the worst individual is a result of natural selection by the fitness function. However, the trend changes in the 20th generation. The worst 3 solutions in

20th generation are worse than that of the 13th generation. Through the investigation of the data, it is found that a bad kind of mutation occurs in the 16th generation (due to the limitation of space for Table 6.2, the data of 16th generation is not included). The second individual in the 16th generation should have provided a bandwidth of 12.375 GHz, but it turns out to be 3.275 GHz. As the generation evolves, the introducing of that bad seed (the mutated solution with 3.275 GHz) results in the existence of the solutions with bandwidth of 3.825 GHz, 4.7 GHz, and 6.2 GHz.

Table 6.2 Comparison of Absorption Bandwidth in the 1st, 2nd, 7th, 13th, and 20th Generations.

Generation / Individual	1st Generation	2nd Generation	7th Generation	13th Generation	20th Generation
1	3.775	11.45	11.45	11.45	12.375
2	9.15	11.45	11.45	12.375	12.375
3	8.25	11.45	11.525	11.825	12.375
4	10.75	10.7	11.45	9.525	12.375
5	9.975	11.225	10.55	10.75	12.375
6	11.35	10.425	11.45	10.725	9.525
7	10.175	9.55	11.025	11.45	11.45
8	10.7	10.8	9.175	11.45	12.375
9	10.8	8.25	11.45	10.8	6.2
10	8.775	8.25	11.375	11.625	12.375
11	11.45	10.575	11.525	11.625	12.375
12	10.325	10.8	11.625	11.025	8.975
13	11.45	10.175	9.85	10.8	12.375
14	9.725	9.5	10.975	10.8	11.625
15	0.05	9.725	11.025	12.175	12.375
16	3.75	9.725	10.725	10.45	12.375
17	10.575	10.925	11.025	9.775	12.375
18	2.55	11.45	9.85	10.4	9.525
19	9.5	9.5	9.85	11.825	12.175
20	10.8	10.4	10.725	11.825	11.625
21	9.85	10.75	10.725	9.775	8.975
22	3.35	10.8	11.45	10.725	12.375
23	10	9.15	10.45	11.625	12.375
24	10.45	11.45	11.45	10.75	3.825
25	6.7	8.25	11.45	10.4	12.375
26	8.7	10.7	10.725	11.825	10.525
27	10.85	10.175	11.45	11.625	4.7
28	4.325	9.85	9.175	9.975	12.375
29	2.925	9.85	10.475	9.775	11.625
30	11.225	9.85	9.175	11.825	12.175

6.3 Optimization of Dual AMCs Functional Unit Cell with 6 × 6 Arrays

The aforementioned analysis verifies the effect of number of generations on the better solution. With a population size of 30, 20 generations are almost sufficient for the convergence of this program. In this section, the size of the functional unit cell is enlarged to search for a broader absorption bandwidth compared with the one of 12.375 GHz. The enlarged functional unit cell consists of 36 elementary unit cells, which means a DNA sequence of 36 bits is required by each individual. In general, the Genetic Algorithm program with a longer DNA sequence needs lager population size and more generations to converge. However, CST requires more time to run the structure due to the larger functional unit cell, leading to a much more running time required by the whole program. Therefore, while the number of generation remains 20, the population size is reduced to 20.

Fig. 6.5 illustrates the generated DNA sequence map of the best individual in 20^{th} generation and the schematic of the correspondingly converted functional unit cell. From Fig. 6.5 (c), the effective absorption bandwidth of the generated functional unit cell is 12.465 GHz (from 8.52 GHz to 20.985 GHz), which is broader than that of the functional unit cell with 16 elementary unit cells. Through analyzing the data of 20 generations, it is found a broader absorption bandwidth of 12.39 GHz arises firstly in the 14^{th} generation. After evolved, the absorption bandwidth of 12.465 GHz is achieved in the 20^{th} generation. Since the solution of 12.465 GHz arises for the first time in the 19^{th} generation, it is obvious that this program is not converged with 20 generations. A larger size of population or more generations might be required for the convergence of the program. However, the better solution has already been achieved even without the convergence, which means an absorption bandwidth broader than 12.465 GHz can be expected with a larger population size, more generations, or a larger size of functional unit cell.

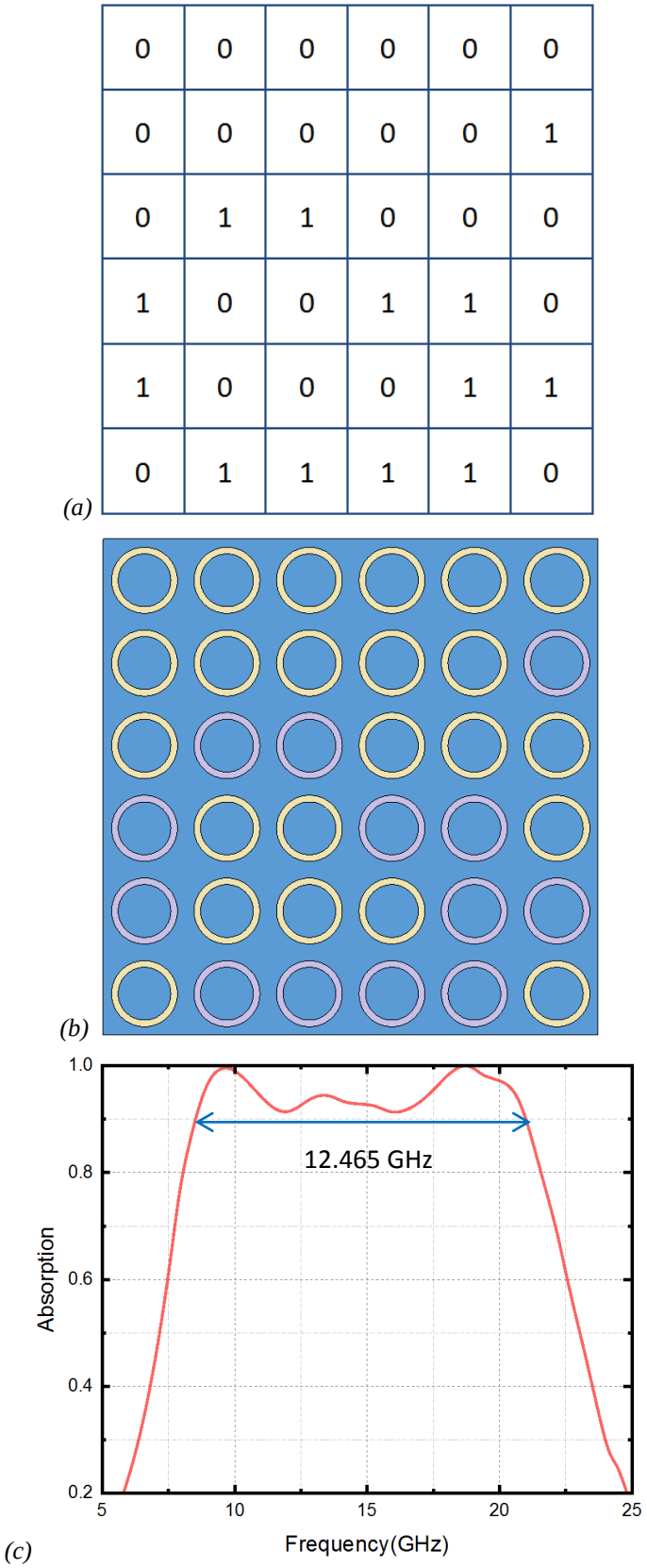

Fig. 6.5 (a) The DNA sequence map of the best individual in 20th generation. (b) Schematic of generated functional unit cell after 20th evolution generation (rings in gold have sheet resistance of 8.7 Ω/sq while rings in lilac have sheet resistance of 98 Ω/sq). (c) The numerically simulated absorption results of the generated structure.

6.4 Chapter Summary

This chapter concerns the optimization of printed graphene AMC based metamaterial absorber with genetic algorithm. Firstly, the program outline is introduced through the flow chart. Next, the functional unit cell composed of 4×4 elementary unit cells is optimized through the program. Comparing to the original functional unit cell with operation bandwidth of 11.41 GHz, a broader effective bandwidth of 12.375 GHz is achieved. Finally, an enlarged functional unit cell with 6×6 elementary unit cells is optimized and a broader effective bandwidth of 12.465 GHz is achieved. With the smaller size of functional unit cell, the convergence of the program has been realized. However, the convergence is not achieved for the later one with larger size of functional unit cell due to the limited population size and generations of the program, which means the better solution of 12.465 GHz is achieved even without the convergence. It can be expected that with a larger function unit cell, which should be composed of 8×8 elementary unit cells as the one in the previous design, a better optimized solution with absorption bandwidth broader than 12.465 GHz can be achieved with the convergence of this program.

The data derived from the program is analyzed to discuss about the convergence and drawbacks of the program for further improvement. With the development of machine learning, the genetic algorithm program has invaluable potential for future development of coding metamaterial absorbers.

Chapter 7: Monolayer Graphene Tunable Terahertz Absorber: Pattern Engraving Approach

In this chapter, a polarization-independent and angle-insensitive broadband tunable metamaterial absorber in THz regime is designed and simulated based on a single-layer graphene pattern with two hollow square-ring gaps and topped with a wide-angle impedance matching (WAIM) layer. To generate extra contiguous resonances and obtain a broadband absorption, unlike conventional method of adding multiple different geometry patterned resonators which result in a large unit cell size, the proposed graphene pattern is designed by engraving two square-ring gaps on a conventional square graphene patch. The utilization of WAIM layer on top of the structure not only improves the absorption under normal incidence, but also guarantees the wide-angle performance.

7.1 Modelling of Graphene (Kubo Formula) in Terahertz Regime

As graphene is a single layer of carbon atom material, the patterned graphene in the proposed design is modelled as a 2D tabulated surface impedance layer with optical conductivity. The surface conductivity of graphene can be derived from Kubo formula [213] as follows [214],

$$\sigma(\omega,\mu_c,\Gamma,T)=\sigma_{intra}(\omega,\mu_c,\Gamma,T)+\sigma_{inter}(\omega,\mu_c,\Gamma,T) \tag{7.1}$$

$$\sigma_{intra}(\omega,\mu_c,\Gamma,T)=\frac{je^2}{\pi\hbar^2(\omega-j2\Gamma)}\int_0^\infty \zeta\left(\frac{\partial f(\zeta)}{\partial\zeta}-\frac{\partial f(-\zeta)}{\partial\zeta}\right)d\zeta \tag{7.2}$$

$$\sigma_{inter}(\omega,\mu_c,\Gamma,T)=-\frac{je^2(\omega-j2\Gamma)}{\pi\hbar^2}\int_0^\infty \frac{f(-\zeta)-f(\zeta)}{(\omega-j2\Gamma)^2-4(\zeta/\hbar)^2}d\zeta \tag{7.3}$$

$$f(\varepsilon)=\frac{1}{e^{(\zeta-\mu_c)/k_BT}+1} \tag{7.4}$$

where ω is angular frequency, μ_c is chemical potential, Γ is a phenomenological scattering rate which is assumed to be independent of energy ζ, T is temperature of Kelvin, e is the electron charge, $\hbar$ is the reduced Planck's constant, k_B is Boltzmann's constant, and $f(\zeta)$ is the Fermi-Dirac

distribution. The two terms σ_{intra} and σ_{inter} are due to intraband contributions and interband contributions, respectively [214].

The chemical potential μ_c is determined by the carrier density n_s [214],

$$n_s = \frac{2}{\pi\hbar^2 {v_F}^2}\int_0^\infty \zeta[f(\zeta) - f(\zeta + 2\mu_c)]d\zeta \tag{7.5}$$

where $v_F \simeq 9.5\times10^5$ m/s is the Fermi velocity. Through chemical doping or applying a bias voltage, the carrier density can be changed, leading to the change of chemical potential, which governs the surface conductivity of graphene.

The carrier relaxation time τ is an important parameter required to calculate the scattering rate Γ, which determines the conductivity of graphene. The carrier relaxation time is mainly related to carrier mobility and the quality of graphene, therefore can be controlled through chemical doping or changing the mobility of carriers. Since graphene has an ultra-fast response rate to photons, the relaxation time is generally very short [215]. In this design, the chemical potential and relaxation time are set to be 1.0 eV and 0.1 ps, respectively.

7.2 Design with Graphene Pattern Engraving Approach

The numerical simulations of the tunable absorber are performed with frequency domain solver in the full-wave software CST Microwave Studio. The unit cell is modelled as an infinite periodic structure through independently applying periodic boundary condition in X and Y directions, and Floquet boundary condition in Z direction.

A schematic of the designed unit cell is illustrated in Fig. 7.1. It can be seen from the schematic that the proposed absorber is composed of a single WAIM layer at top, a single-layer patterned graphene with the dielectric substrate, and a ground plane at the bottom. For the WAIM layer and dielectric substrate, the TOPAS polymer with a relative permittivity ε of 2.35 is utilized. A reflective layer of gold with conductivity σ of 4.56×10^7 *S/m* and thickness of 0.2 *μm* is applied as ground plane. The periodic graphene patterns are obtained through cutting off two square-ring gaps with different size from the conventional square arrays.

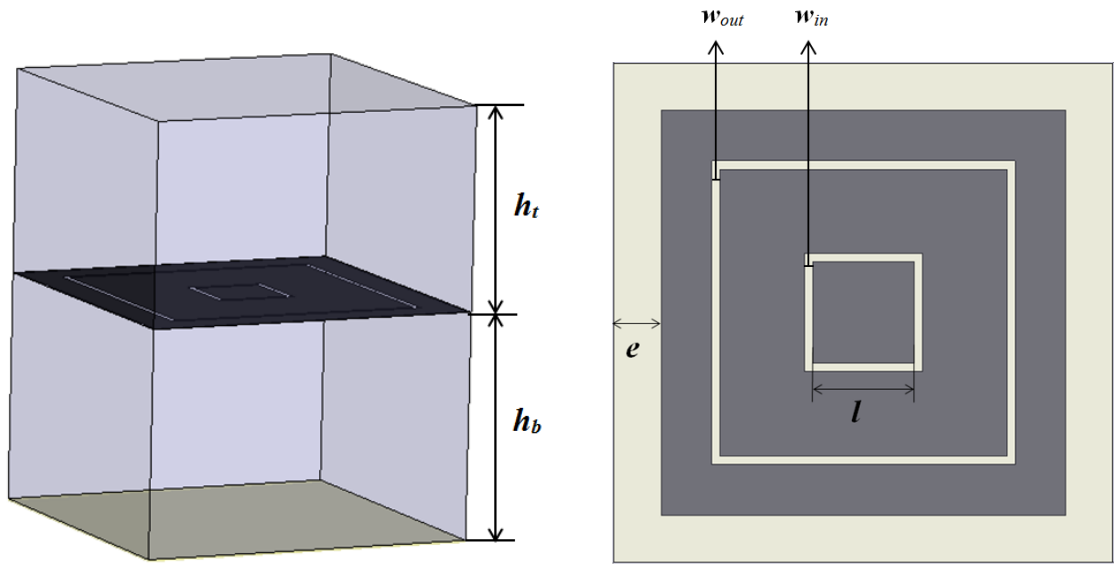

Fig.7.1 (a) Schematic of the broadband tunable metamaterial absorber. (b) Top view of the patterned graphene layer. The geometry parameters of the structure are set as (unit:μm): h_t = 18, h_b = 20, l = 6, e = 3.

With the WAIM layer topped, the conventional periodic array made up of single kind of intact square graphene patches (as displayed in Fig. 7.2 (a)) is simulated firstly. The red line in Fig. 7.3 indicates that the absorption of periodic square patterns fluctuates around 80% within a wide bandwidth. However, the over 90% absorptivity can only be achieved at about 3.93 THz. Next, the inner square-ring gap is cut off from the square patch and the absorption performance is shown by the blue line in Fig. 7.3. With the inner square-ring engraved, the absorption is improved within a broadband. Except for the absorption peak at 3.93 THz, the over 90% absorptivity can be obtained within a range of frequencies between 1.78 THz to 3.05 THz. On the other hand, when the outer square-ring gap is engraved from the square patch, the over 90% absorptivity can be obtained at lower frequencies within a range of between 0.91 THz to 2.77 THz.

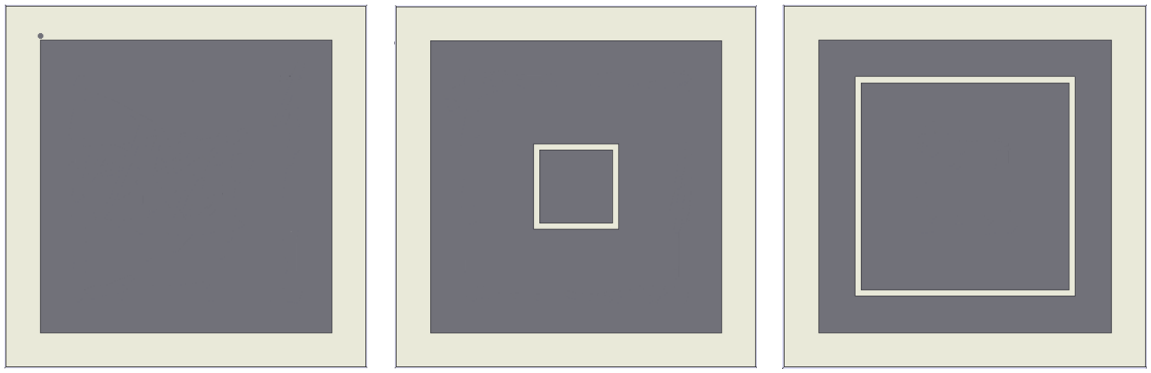

(a) *(b)* *(c)*

Fig.7.2 Unit cell with (a) conventianl graphene patch, (b) graphene patch with inner square-ring gap, (c) graphene patch with outer square-ring gap.

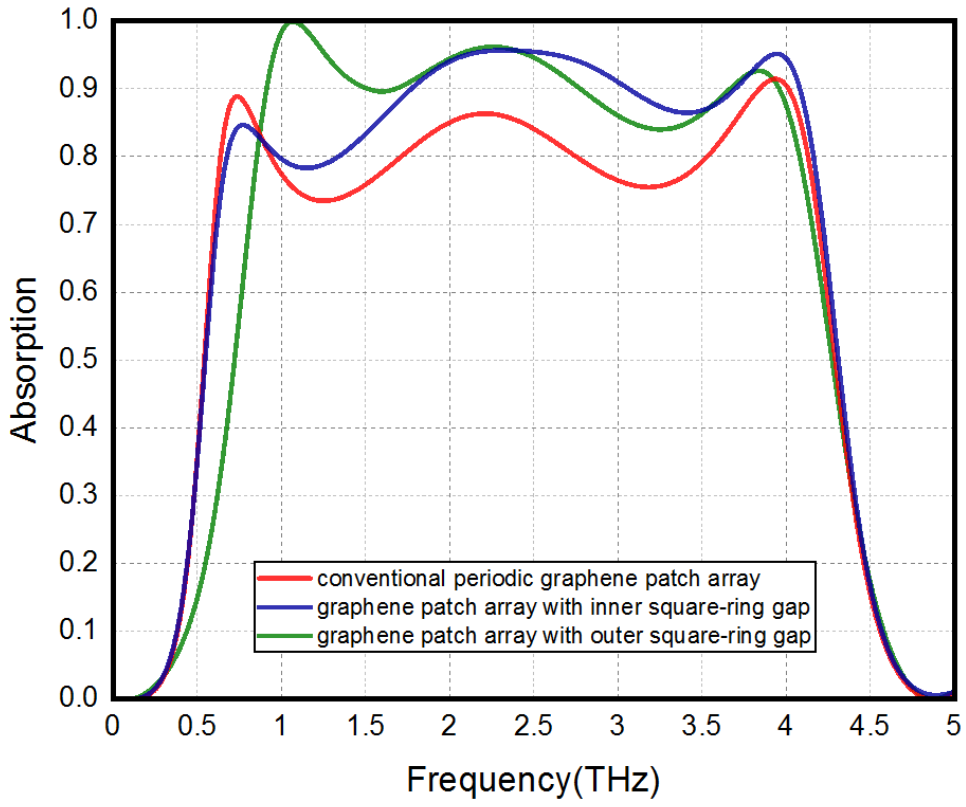

Fig.7.3 Absorption performance of the structure with different kinds of patterns.

When the inner and outer square-ring gaps are cut off from the square graphene patch at the same time, the broadband effective absorption with over 90% absorptivity is achieved from 0.93 THz to 4.06 THz with a bandwidth of 3.13 THz and a fractional bandwidth of 125%. As shown in Fig. 7.4, the numerical simulation results show a high consistency as the polarization angles vary

from 0 ° to 90 ° with a step width of 30 °, illustrating the polarization-independent property of the designed tunable absorber. The simulation results indicate that within the operating frequency band (from 0.93 THz to 4.06 THz) of the tunable absorber, the outer square-ring gap mainly contributes the high absorption at lower frequencies while the inner one mainly contributes at relatively higher frequencies. Consequently, the two gaps together provide an ultra-wideband effective absorption (>90% absorptivity).

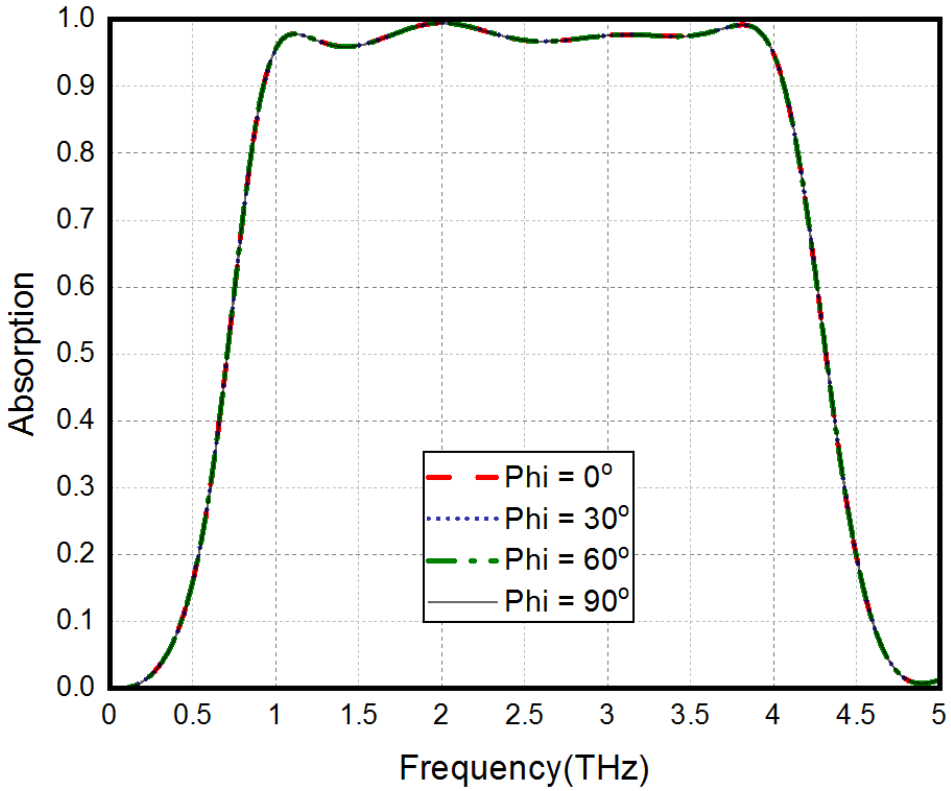

Fig.7.4 Absorption performance with various polarization angles under normal incidence.

7.3 Analysis and Discussion

To elucidate the absorption mechanism, the electric field distribution and the surface current distribution of four absorption peaks (located at 1.1 THz, 2 THz, 3 THz, and 3.8 THz) under TE mode are investigated and illustrated in Fig. 7.5. As shown in Fig. 7.5 (a), the electric field, surface currents on the graphene layer, and surface currents on the ground layer at 1.1 THz are displayed by the figures from left to right, respectively. As observed in the surface currents at 1.1 THz, the electric resonance is mainly excited by the inner gap on its top side. Then the oscillating

currents flow along the graphene pattern, while the flowing currents on the golden ground layer are in the inversed direction, arousing strongly magnetic resonance. These electromagnetic resonances lead to the absorption peak at 1.1 THz. At 2 THz, the electric resonance is mainly excited by the inner gap on its bottom side. Compared with the electric field which spreads almost the entire pattern at 1.1 THz, the electric field at 2 THz concentrates on the top and bottom sides of both inner and outer gaps. Unlike the magnetic resonance shown at 1.1 THz, the surface currents on the graphene layer mainly flow in the same direction with the currents on the ground layer. When it comes to 3 THz, the electric field distribution has another different contour with the intensive electric field locating at four corners of outer gap. The relatively uniform electric field spreads almost the entire pattern like that of 1.1 THz. The surface currents on the graphene layer emit from the bottom of the pattern and flow to the top, which are in the inverse direction of the currents on the ground layer. Intensive currents converge at the center small square surrounded by the inner square-ring gap. For the situation at 3.8 THz, the electric field concentrates around the midline of the pattern. The surface currents on the graphene layer emit from top and flow to bottom, keeping the same flow direction with the currents on the ground layer.

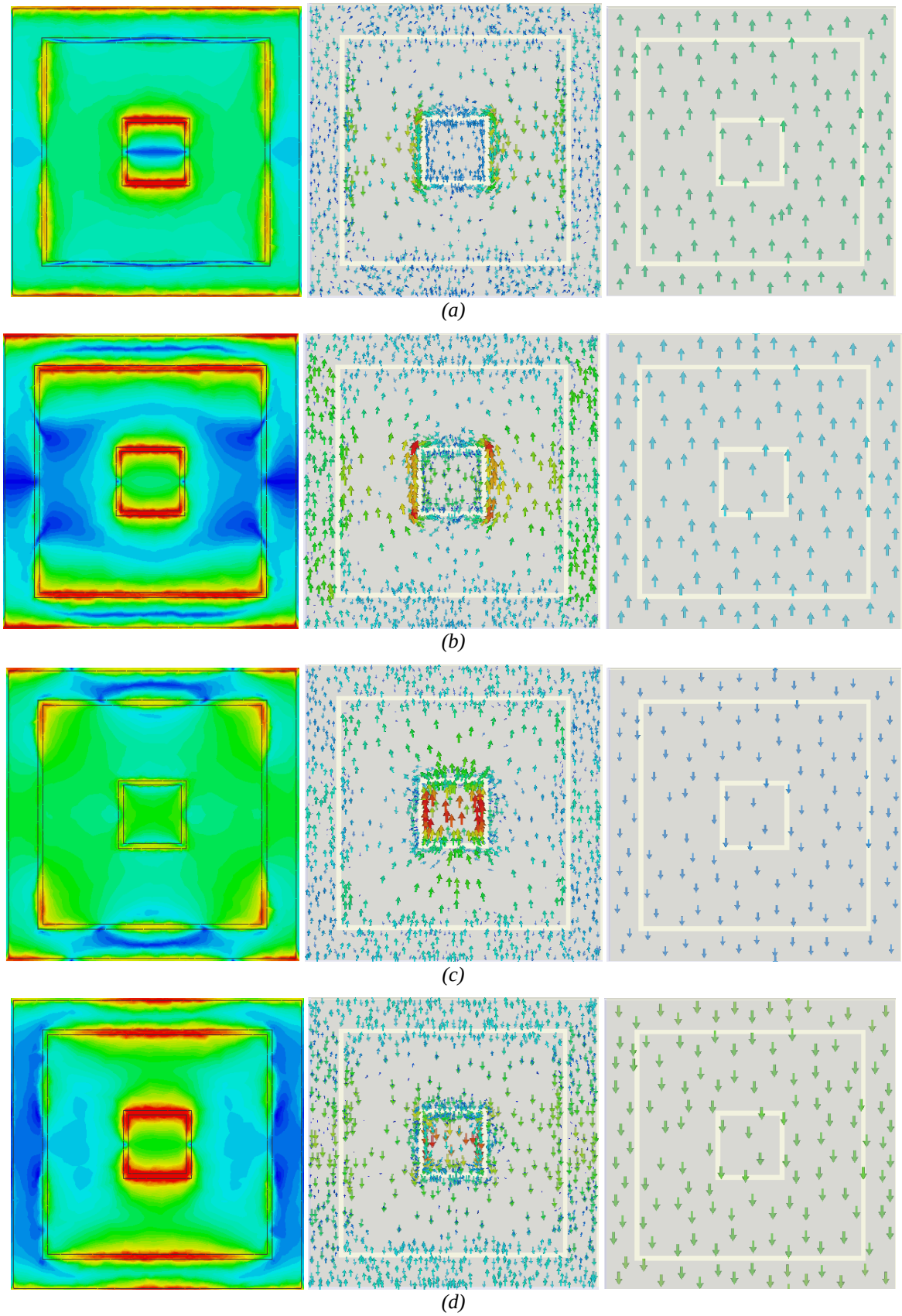

Fig.7.5 (TE mode) Electric field distribution and surface current distribution in the graphene layer and the bottom ground plane under normal incidence at (a) 1.1 THz, (b) 2 THz, (c) 3 THz, and (d) 3.8 THz.

The parameters related to the two square-ring gaps are changed to investigate the different effects of the size, location and width of the gaps on the absorption. Fig. 7.6 (a) shows the simulation results of the structure with various sizes and locations of inner gap. When l = 2 um, the inner gap has relatively smaller size and locates at a position closer to the center of graphene pattern. With this geometry, the structure achieves over 90% absorptivity within a limited frequency band from 0.93 THz to 2.8 THz as shown by the green line in Fig. 7.6 (a). As the value of l increases, the inner gap becomes larger and moves away from the center. The over 90% absorptivity can be obtained in a broader frequency band compared with the bandwidth when l = 2 um. Meanwhile, the absorptivity at 1.5 THz and 2.6 THz increases while that of 2 THz decreases. On the other hand, the absorptivity around 3.3 THz increases at first, reaching the maximum value of 97.5% when l is set to be 6 um, then decreases. Adhering to the principle of smooth effective absorption in a broad continuous frequency band, the most appropriate value for l is 6 um. Fig. 7.6 (b) displays the absorption results with different sizes and locations of outer gap. As e increases from 1 um to 5 um, the outer gap gets smaller size and locates at a position closer to the inner gap. The results indicate that the size and location of outer gap mainly affect the lower frequency bound of the effective absorption (>90%) band. The increasing of e results in a blue shift of the lower frequency bound, while the higher frequency bound almost stays unchanged, leading to a shrinking of effective absorption bandwidth. Although e with smaller values can provide wider effective absorption bandwidth, the price is the fluctuation of absorptivity. After weighing the pros and cons, the value of e is set as 3 um.

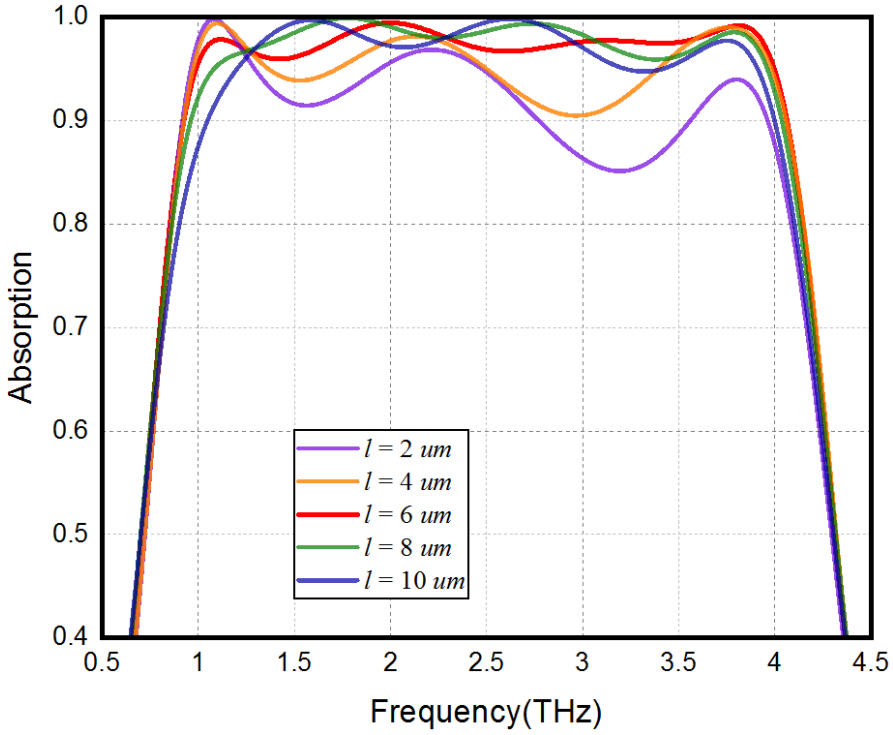

(a)

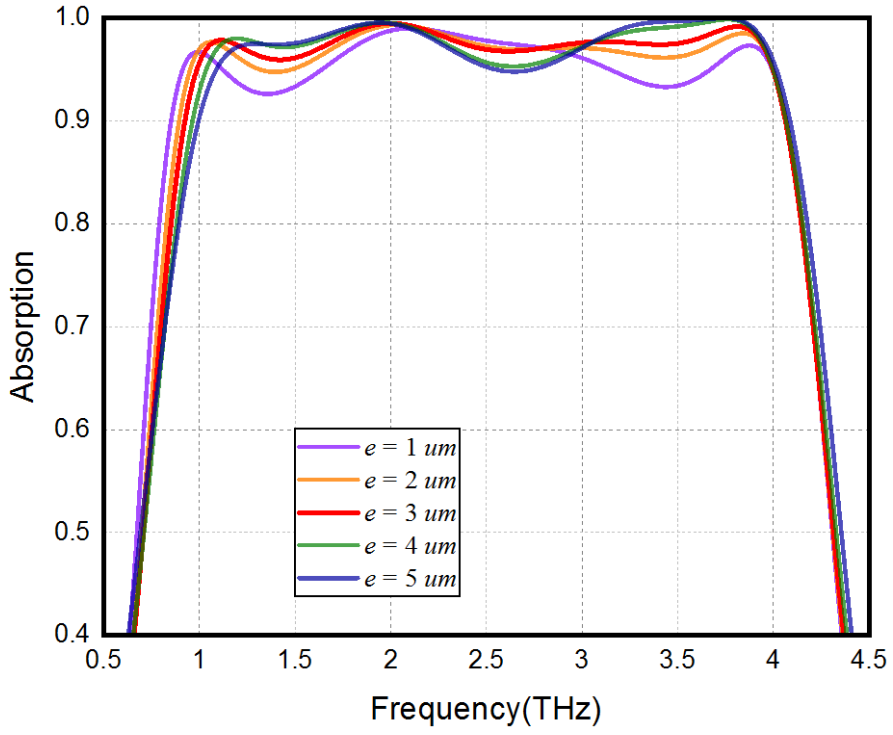

(b)

Fig.7.6 Absorption performance of the absorber with different size and location of the (a) inner gap and (b) outer gap, respectively.

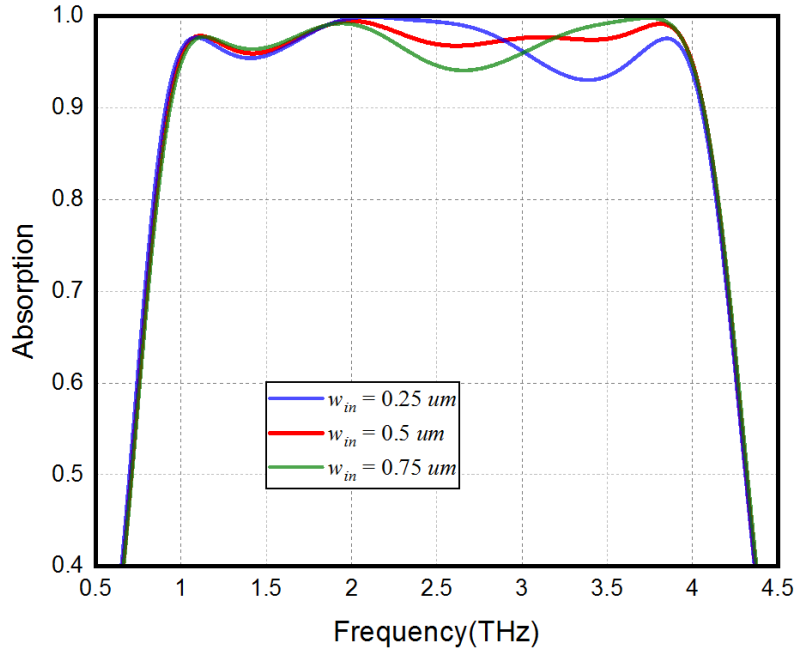

(a)

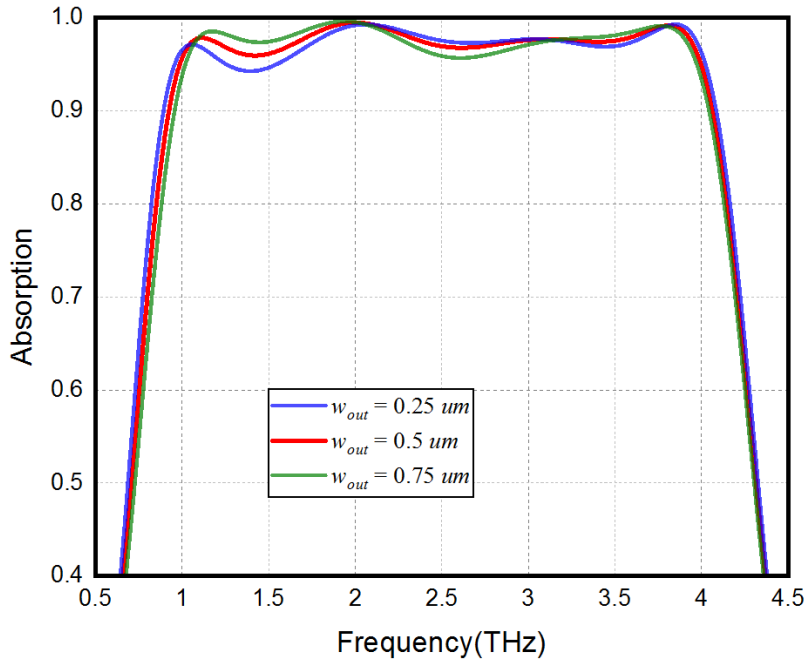

(b)

Fig.7.7 Absorption performance of the absorber with different width of the (a) inner gap and (b) outer gap, respectively.

Fig. 7.7 (a) and (b) illustrate the numerical simulation results with different inner gap width w_{in} and outer gap width w_{out}, respectively. The analysis of these two parameters is similar with that of *e*. By changing the values of w_{in} and w_{out}, broader effective absorption bandwidth can be obtained at the cost of absorptivity fluctuation. For the purpose of obtaining a smoother

absorption curve in a broad continuous bandwidth, the optimized value is 0.5 um for both w_{in} and w_{out}.

The influence of the thickness of the WAIM layer on the absorption is illustrated in Fig. 7.8. Without the WAIM layer, the structure provides two narrow effective absorption (>90% absorptivity) bandwidth with the center frequency located at 1.3 THz and 3 THz, respectively. As the thickness of the WAIM layer increases from 0 to 18 μm, the bandwidth of effective absorption keeps extending. The ultra-broadband effective absorption from 0.93 THz to 4.06 THz is obtained with the 18 μm thickness of the WAIM layer. When the thickness increases to 27 μm, the structure provides near-unity absorption from 1 THz to 1.5 THz. However, the continuous bandwidth of effective absorption is interrupted at around 2.3 THz. From the numerical results, we choose the thickness of 18 μm as the optimized value.

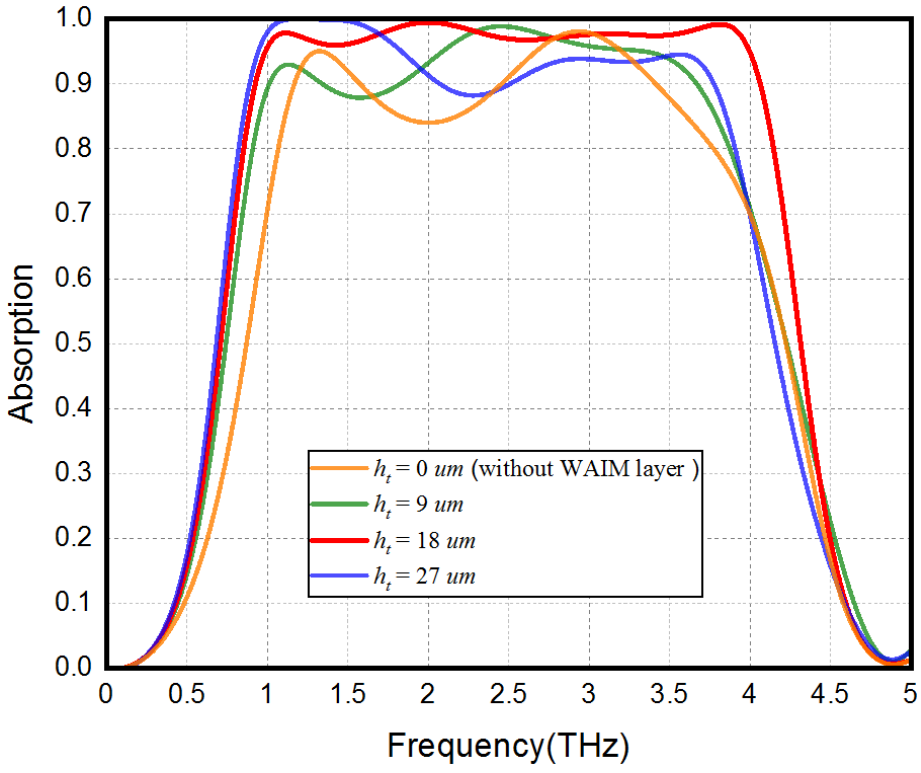

Fig.7.8 Absorption performance of the absorber with different thickness of the WAIM layer.

7.4 Valuable Properties of Tunable Absorbers

7.4.1 Switchable broadband Terahertz absorber/reflector

Due to the tunable property of graphene, the absorption of the proposed absorber can be tuned by changing the surface conductivity of graphene sheet. According to (5), the chemical potential, which governs the surface conductivity of graphene, can be controlled dynamically through chemical doping or applying bias voltage. Here, through varying the chemical potential μ_c from 0 eV to 0.4 eV, the absorber shows a switchable property. The numerical simulation results illustrated in Fig. 7.9 indicate the proposed structure can operate as a switch with corresponding off and on states controlled by the chemical potential. For the chemical potential of 0 eV, even the absorption peak can only provide around 19% absorptivity, whereas over 90% absorptivity can be obtained when the chemical potential increases to 0.4 eV.

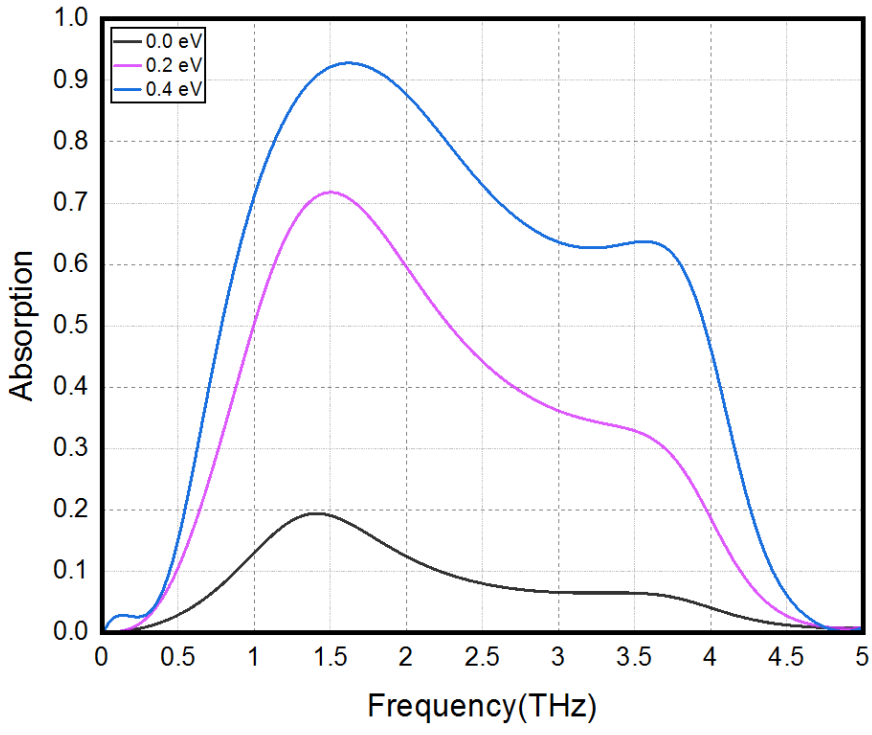

Fig.7.9 Absorption performance of the absorber with chemical potential tuned from 0 eV to 0.4 eV.

7.4.2 Tunable broadband absorbers

Additionally, the effective absorption (>90% absorptivity) band of the proposed structure can also be tuned by changing the chemical potential. With a chemical potential of 0.4 eV, the effective absorption has a fractional bandwidth of 30.5%. The fractional bandwidth extends to 125% and 129% when the chemical potential is set to be 1.0 eV and 1.2 eV, respectively. It can be seen from Fig. 7.10 that as the chemical potential increases, the proposed absorber achieves a broader effective absorption bandwidth and a larger fractional bandwidth. However, when the chemical potential increases from 1 eV, the extension of fractional bandwidth is at the cost of absorptivity fluctuation, especially the absorptivity at around 1.5 THz, which drops below 90% when the chemical potential increases to 1.4 eV.

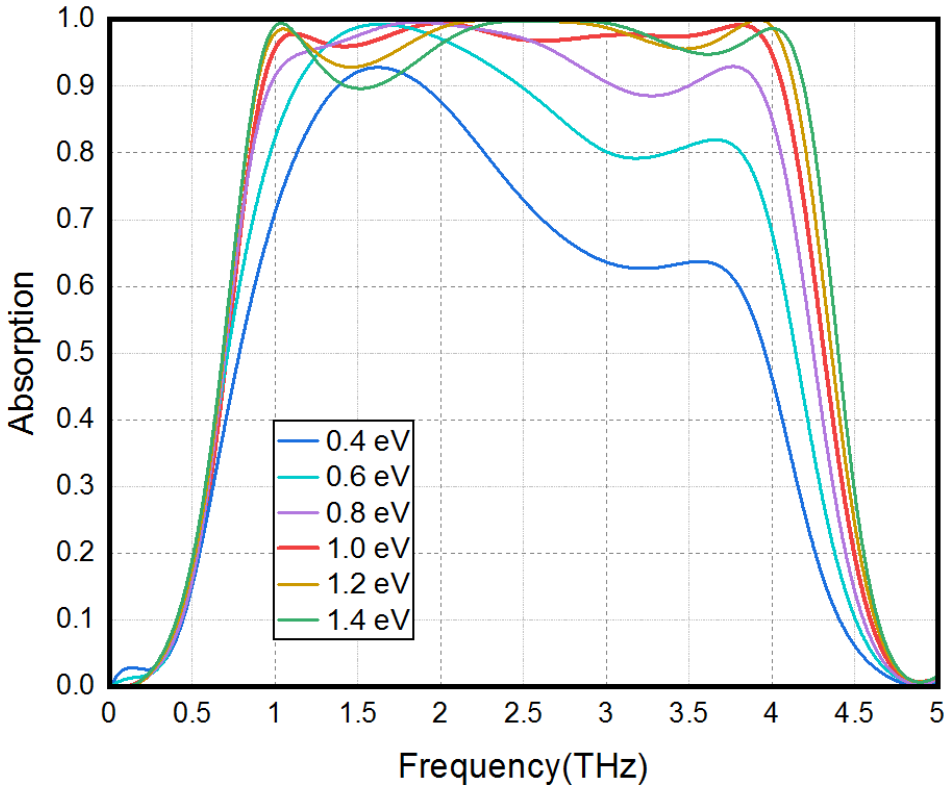

Fig.7.10 Absorption performance of the absorber with chemical potential tuned from 0.4 eV to 1.4 eV.

7.4.3 Ultra-wide-angle performance

The efficacy of the WAIM layer on the sensitivity of absorption to incident angle is further investigated through wide-angle performance of the absorber. Fig. 7.11 shows the absorption

contour maps which illustrate the numerical simulation results under oblique incident angles from $0°$ to $80°$ with the step of $10°$ for transverse electric (TE) wave and transverse magnetic (TM) wave, respectively. From the absorption contour maps, the absorption peak keeps over 90% absorptivity up to $70°$ incident angle for TE mode and $80°$ incident angle for TM mode, respectively. Although the absorption spectra has a blue shift over the operating frequency as the incident angle becomes larger, the over 80% absorptivity can be achieved within a broad frequency band over a wide range of incident angles up to $70°$ for both TE mode (with a bandwidth of 1.5 THz) and TM mode (with a bandwidth of 2 THz). The performance under various incident angles indicates the proposed structure is an ultra-wide-angle absorber, verifying the efficacy of the WAIM layer. The comparison of incident angle sensitivity between the proposed absorber which applies the WAIM layer and previous reported tunable broadband absorbers without WAIM layer emphasizes the effect of the WAIM layer on broadening the operation angles of absorber.

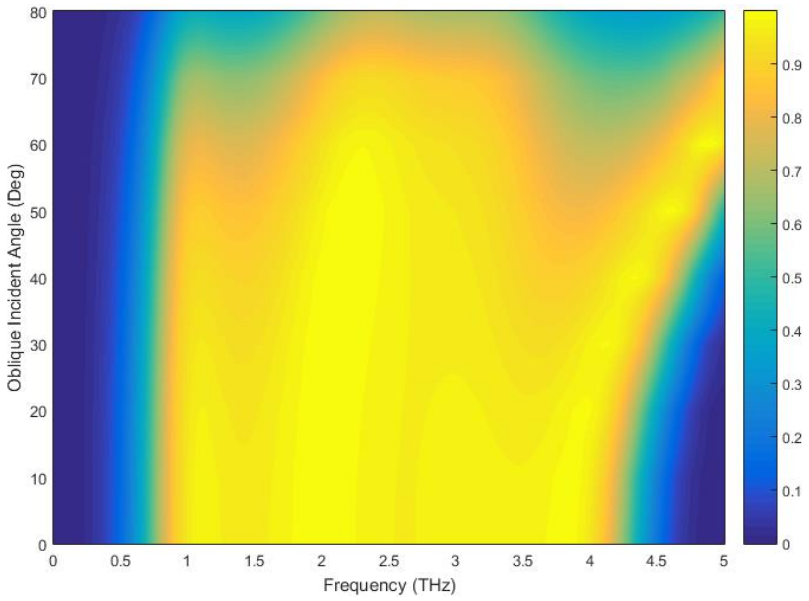

(a)

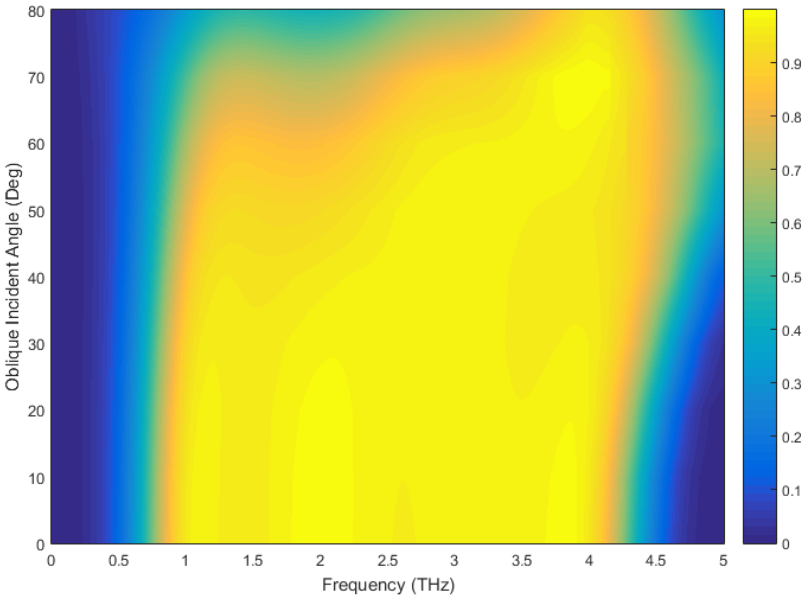

(b)

Fig. 7.11 Absorption contour map of the absorber with under oblique incident angles from 0 °to 80 °with the step of 10 °for (a) transverse electric (TE) wave and (b) transverse magnetic (TM) wave, respectively.

7.5 Chapter Summary

In this chapter, the tunability of monolayer graphene is applied to metamaterial absorber. A broadband tunable metamaterial absorber based on single-layer of graphene pattern and topped with a WAIM layer is designed and investigated to numerically demonstrate the pattern engraving approach. The design starts from a unit cell covered by a layer of graphene patch, and

then two different square-ring gaps are engraved from the intact graphene patch one by one. The influence of two square-ring gaps on the absorption is investigated through changing the geometry parameters of both gaps.

This absorber can provide over 90% absorptivity with a broad bandwidth of 3.13 THz and a fractional bandwidth of 125% under normal incident when the chemical potential of the graphene is set as 1.0 eV. The electric field distribution and surface current distribution are analyzed to elucidate the mechanism of broadband absorption. The numerical simulation results of the proposed absorber indicate the polarization-independent and angle-insensitivity properties. Due to the WAIM layer, the broadband absorption with over 80% absorptivity can be achieved within a wide range of incident angles up to 70 °for both TE mode and TM mode.

The tunable property of the absorber is also investigated by varying the chemical potential of the graphene sheet. The absorber can be used for switching applications with the on and off states are controlled by the values of chemical potential. Besides, the fractional bandwidth of the proposed absorber can be tuned from 30.5% to 129% by changing the chemical potential from 0.4 eV to 1.2 eV. With these valuable properties, this absorber is appropriate to be scaled to the infrared and visible frequencies and applied to identification, sensing, detecting, and imaging applications.

Chapter 8: Conclusions and Future Works

This thesis focuses on the study of printed graphene and graphene monolayer metamaterial absorbers with broadband effective absorption. Novel and combed design approaches are investigated and demonstrated through several correspondingly designed metamaterial absorbers with broad effective absorption bandwidth, angle-insensitive and polarization-independent properties, and relatively small unit cell and thickness.

To begin with, a triple-layer microwave absorber is designed through multilayer structure approach and its equivalent circuit model is investigated thoroughly. The operation frequency ranges from 6 GHz to 50 GHz, covering from C band to Ka band of the microwave band of electromagnetic spectrum. In order to design an absorber which can work at lower frequency and cover the S band, a similar but different microwave absorber with two layers of printed graphene patterns is designed and analyzed through the same approach. With the introduction of a WAIM layer on top of the structure, this absorber can operate at lower frequency ranging from 2.2 GHz to 18.4 GHz and remain the relative absorption bandwidth of 157%. Besides, the broadband absorption performance at various incident angles is guaranteed owing to the WAIM layer.

The novel design approach based on ohmic contact excited eddy currents is proposed and numerically demonstrated through the design and simulation of an ultra-thin broadband metamaterial radar absorber. According to the mechanism of the eddy current, as the thickness of the dielectric substrate becomes thin enough to be omitted, the anti-parallel surface currents in the front and back surfaces of the substrate constitute current loops like eddy currents flowing in closed loops within conductors, and lead to strong magnetic resonances and energy loss, which in another word is that the absorber with smaller thickness should be able to achieve better absorption performance. Therefore, the influence of the thickness on the absorption performance is investigated, and the results are as expected. Eventually, the ultra-thin absorber with 0.3 mm dielectric substrate is designed and numerically simulated to provide an effective absorption from 1.15 GHz to 20 GHz, with a relative absorption bandwidth of 178%. However, the fabrication

and experimental measurement are required for further investigation and demonstration of this approach.

The thesis also demonstrates the novel printed graphene AMC based radar absorber. The printed graphene AMCs with specific sheet resistances (8.7 Ω/sq and 98 Ω/sq) are designed and fully screen printed. The specific sheet resistances of printed samples are obtained through controlling the screen printing and compression processes. During the fabrication, controlling the sheet resistance wasn't easy as the semi-automatic screen printer (YICAI4060PV) and manual roller compressor were used. The settings of parameters, such as printing speed, type of squeegees, squeegee pressure and squeegee angle, can have different kinds of influence on the final printed samples. Therefore, the controlling very much depends on experience. Due to the aforementioned reasons, it is unsurprised that the printed samples have several types of fabrication deviations. However, a reasonable good match between the measurement and simulation results is still achieved even with these fabrication deviations, demonstrating the feasibility of printed graphene AMC approach. In addition to that, the experimental measurement results indicate the printed graphene AMC based radar absorber also has a good mechanical flexibility and can provide greater than 70% absorption within most parts of the X and K_u bands in different bending cases. Meanwhile, the angle-insensitive property of AMC based absorbers can also be improved through the novel printed graphene AMCs. This approach could have a wider application as it has provided more degree of freedom in radar absorber designs.

To explore the potential of metamaterial absorbers with different sheet resistances on a single surface, genetic algorithm programming is applied to optimize the printed graphene AMC based radar absorber. The original arrangement of dual AMCs in the chessboard configuration is distributed and new arrangement is found through the genetic algorithm. With the functional unit cell of 4×4 arrays, the optimized absorber can provide an effective bandwidth of 12.375 GHz, which is broader than the original designed absorber with a larger functional unit cell of 8×8 arrays. Further investigation is taken place on the functional unit cell of 6×6 arrays, and a better effective bandwidth of 12.465 GHz is achieved even without the convergence of program. It can

be expected that with further improvement, the genetic algorithm program has invaluable potential for future development of coding metamaterial absorbers.

The tunable conductivity of monolayer graphene is utilized to design the tunable THz metamaterial absorber. The tunability comes from the varying conductivity of graphene tuned by changing the chemical potential through external voltage. The absorption peak varies more than 70% when the chemical potential is changed in the range 0 – 0.4 eV. This gives the idea of applying the absorber in switching applications with the on and off states controlled by an external voltage. Additionally, the relative absorption bandwidth of the absorber can be tuned from 30.5% to 129% by changing the chemical potential from 0.4 eV to 1.2 eV which means not only the absorption performance but also the effective absorption bandwidth of the absorber can be tuned according to the demands. The flexibility of tunability makes the absorber appropriate to be applied to identification, sensing, detecting, and imaging applications.

In summary, this thesis has proposed several novel design approaches which have potential value for the future development of metamaterial absorbers. It also has covered various types of metamaterial absorbers with broad effective absorption bandwidth. The possible future steps and improvements for the related work are listed as followed.

1. The multilayer structures with different printed graphene sheet resistances in Chapter 3 and Chapter 4 are difficult to fabricate at the time, especially the resistive sheet with 1600 Ω/sq sheet resistance in Chapter 4. However, the fabrication techniques of printed graphene based applications have improved greatly over the years. The fabrication and experimental measurements of these designs can be expected in the near future. The experimental demonstration of the ohmic contact excited eddy currents approach in Chapter 4 is of vital importance and might lead to a major breakthrough in metamaterial absorber research area.

2. The design and fabrication of the novel printed graphene AMC based radar absorber in Chapter 5 can be improved. The paper-silicone interface would create unwanted reflection because the refractive indices of the materials are slightly different and the index mismatch

results in the unwanted reflections. The reason that the graphene patterns are printed on paper is not only because the silicone substrate is hydrophobic but most importantly the printed patterns need to be compressed to control the sheet resistance. It is impossible to do the compression on silicone. Although the effects of unwanted reflections have been considered in the design by the paper layer in numerical simulations, yet some other fabrication deviations are induced by the paper-silicone interface, such as the air gap induced by the uneven distribution of adhesive between the paper and silicone. Therefore, the experiments can be improved through printing the graphene ink patterns on a single material that is suitable for graphene ink printing and compression. Kapton might be a candidate for the improvement.

3. Since the novel printed graphene AMC approach in Chapter 5 has been experimentally demonstrated, more printed graphene AMC based metamaterial absorbers can be designed and fabricated to explore the potential of printed graphene AMCs with different sheet resistances. By combining the various sheet resistances with different shapes or sizes of printed graphene AMCs, broader effective absorption bandwidth can be expected.

4. The genetic algorithm program in Chapter 6 achieves an optimized broader effective absorption bandwidth successfully even without the convergence of the program. By investigating the data derived from the program, some drawbacks or problems are discovered. Firstly, the program might take a lot of time to realize the convergence. Secondly, the mutation process could lead the structures mutate to unwanted direction, inducing worthless solutions to the population, which results in a prohibitively long time for the program to achieve convergence. To some degree, the first drawback is caused by the second problem partially. Thirdly, the program might pass the less optimal designs which have the possibility to provide greater global optimum because the algorithm cannot backtrack. This issue has a few solutions that can be implemented to combat it. The widely used method is to inject more randomized solutions into the algorithm in order to promote a greater diversity in the population. However, this method might lead to more time required for convergence. There is another method provided here, which hopefully can solve the three aforementioned problems to some extent at the same time. The

solution relies on controlling the mutation direction. A selection function can be added to mutation process to weed out unwanted mutation and keep the good ones. In this way, by increasing the mutation rate and adding the selection function to the mutation process, a greater diversity in the population can be achieved, and meanwhile less bad or worthless mutation can take place during the evolution, and thus reducing the time required for convergence. With the improvement of the genetic algorithm program, it can be further used for coding metamaterial absorbers in the future.

5. So far the functional unit cells designed in Chapter 5 and Chapter 6 are all composed of two AMCs with different sheet resistances. With the successful demonstrations in both approaches mentioned in Chapter 5 and Chapter 6, a functional unit cell with more different sheet resistances on the single surface can be designed and optimized to investigate the potential of multi-(sheet)resistance approach for broader effective absorption bandwidth.

6. The pattern engraving approach demonstrated in Chapter 7 can be further used or investigated to design transparent metamaterial absorbers. As more engraved gaps added to the original intact monolayer graphene patch, the transparency rate can be improved. Therefore, this approach might be potential for the future development of transparent metamaterial absorbers.

References List

[1] Naamlooze Vennootschap Machinerieen, French Patent 802 728, 1936.

[2] Schade, H.A. Schornsteinfeger. U.S. Tech. Mission to Europe, Tech. Rep. 90-45 AD-47746, 1945.

[3] O. Halpren and M. J. Johnson, Jr., "Radar: summary report of HARP project," *OSRD Div.14*, vol.1, 1946.

[4] W. H. Emerson, "Electromagnetic wave absorbers and anechoic chambers through the years," *IEEE Trans. Antennas Propag*. vol. 21, pp. 484–490, 1973.

[5] R. S. Kshetrimayum, "A Brief intro to metamaterials," *IEEE Potentials*, vol.23, pp.44–46, 2004.

[6] C. M. Watts, X. Liu, and W. J. Padilla, "Metamaterial electromagnetic wave absorbers," *Adv. Mater*. vol. 24, pp.98–120, 2012.

[7] N. Engheta,"Thin absorbing screens using metamaterial surfaces," In *IEEE Antennas and Propagation Society International Symposium (IEEE Cat. No.02CH37313)*, vol.2, pp. 392–395, 2002.

[8] N. I. Landy, et al., "Perfect metamaterial absorber," *Phys. Rev. Lett.*, vol**.** 100, p.207402, 2008.

[9] Y. Kotsuka, Electromagnetic wave absorbers: detailed theories and applications. Hoboken, New Jersey: John Wiley & Sons, Inc, 2019.

[10] K. S. Novoselov, A. K. Geim, S. V. Morozov, D. Jiang, Y. Zhang, S. V. Dubonos, I. V. Grigorieva, and A. A. Firsov, "Electric field effect in atomically thin carbon films," *Science*, vol.306, pp.666–669, 2004.

[11] A. M. Turing, "Computing Machinery and Intelligence", *A Quarterly Review of Psychology and Philosophy*, VOL. LIX. No.236. October, 1950.

[12] N. Barricelli, "Numerical examples of evolution processes", *Methodos*, pp.45-68, 1954.

[13] E. Calabrò, "Introduction to the special issue 'Electromagnetic Waves Pollution'," *Sustainability*, vol.10, p.3326, 2018.

[14] G. Redlarski, *et al.*, "The influence of electromagnetic pollution on living organisms: historical trends and forecasting changes," *BioMed Research International*, Article ID 234098, 2015.

[15] R. C. Beasond and P. Semm, "Responses of neurons to an amplitude modulated microwave stimulus," *Neurosci. Lett.*, vol.333, pp.175–178, 2002.

[16] H. Lai, A. Horita, C. K. Chou, and A. W. Guy, "Low-level microwave irradiations affect central cholinergic activity in the rat," *J. Neurochem*, vol.48, pp.40–45, 1987.

[17] K. Fritze, *et al.*, "Effect of global system for mobile communication (GSM) microwave exposure on blood-brain barrier permeability in rat," *Acta Neuropathol*, vol.94, pp.465–470, 1997.

[18] E. K. Balcer-Kubiczek and G. H. Harrison, "Neoplastic transformation of C3H/10T1/2 cells following exposure to 120 Hz modulated 2.45 GHz microwaves and phorbol ester tumour promoter," *Radiat. Res*., vol.126, pp.65–72, 1991.

[19] Garaj-Vrhovac, V.; Horvat, D.; Koren, Z. "The effect of microwave radiation on the cell genome," *Mutat. Res*., vol.243, pp.87–93, 1990.

[20] E. Diem, C. Schwarz, F. Adlkofer, O. Jahn, and H. Rüdiger, "Non-thermal DNA Breakage by Mobile-Phone Radiation (1800 MHz) in Human Fibroblasts and in Transformed GFSH-R17 Rat Granulosa Cells in Vitro," *Mutat. Res*., vol.583, pp.178–183, 2005.

[21] Resolving Interference Issues at Satellite Ground Stations. Anritsu Company, 2020.

[22] W. W. Salisbury, "Absorbent body for electromagnetic waves," U.S. Patent 2599944, 1952.

[23] E. McMillan, "Microwave radiation absorber," U.S. Patent 2822539A, 1958.

[24] H. A. Tanner, "Fibrous microwave absorber," U.S. Patent 2977591A, 1961.

[25] F. Ding, Y. X. Cai, X. C. Ge, Y. Jin, and S. L. He, "Ultra-broadband microwave metamaterial absorber," *Appl. Phys. Lett*., vol.100, p.103506, 2012.

[26] G. Dash, "How RF anechoic chambers work," Ampyx LLC, 2005.

[27] R. Jamal, R. K. Singh, and I. K. Singh, "A basic concept to anechoic chamber and determination of highly selective absorber material with respect to insertion loss and refection coefficient," *International Journal of Applied Engineering Research*, vol.14(2), 2019.

[28] D. Maystre and R. Petit, "Brewster incidence for metallic gratings," *Opt. Comm.*, vol.17, pp.196–200, 1976.

[29] M. C. Hutley and D. Maystre, "The total absorption of light by a diffraction grating," *Opt. Comm.*, vol.19, pp.431–436, 1976.

[30] J. L. Roumiguieres, D. Maystre, and R. Petit, "On the efficiencies of rectangular-groove gratings," J*ournal of the Optical Society of America*, vol.66, p.772, 1976.

[31] R. W. Wood, "On a remarkable case of uneven distribution of light in a diffraction grating spectrum," *Proc. Phys. Soc. London*, 18, 269, 1902.

[32] J. B. Pendry, A. J. Holden, W. J. Stewart, and I. Youngs, "Extremely low frequency plasmons in metallic mesostructures," *Phys. Rev. Lett.*, vol.76, pp.4773–4776, 1996.

[33] J. B. Pendry, A. J. Holden, D. J. Robbins, and W. J. Stewart, "Magnetism from conductors and enhanced nonlinear phenomena," *IEEE Trans. Microwave Theory Tech*. vol. 47, pp.2075–2084, 1999.

[34] D. R. Smith, J. B. Pendry, and M. C. K. Wiltshire, "Metamaterials and negative refractive index," *Science*. vol.305, p.788, 2004.

[35] J. B. Pendry, D. Schurig, and D. R. Smith, "Controlling electromagnetic fields," *Science*. vol. 312, p.1780, 2006.

[36] E. E. Narimanov and V. G Veselago. "The left hand of brightness: past, present and future of negative index materials." *Nature materials*, vol.5, pp.759–762, 2006.

[37] Viktor G. Veselago, "The electrodynamics of substances with simultaneously negative values of ε and μ," *Sov. Phys. Usp*., vol.10, p.509, 1968.

[38] D. R. Smith, W. J. Padilla, D. C. Vier, S. C. Nemat-Nasser, and S. Schultz, "Composite medium with simultaneously negative permeability and permittivity," *Physical review letters*, vol.84, pp.4184–4187, 2000.

[39] R. A. Shelby, D. R. Smith, and S. Schultz, "Experimental verification of a negative index of refraction," *Science*, vol.292, pp.77–79, 2001.

[40] D. Schurig, J. J. Mock, B. J. Justice, S. A. Cummer, J. B. Pendry, A. F. Starr, and D. R. Smith ,"Metamaterial electromagnetic cloak at microwave frequencies," *Science, vol.*314, pp.977–980, 2006.

[41] N. Fang, H. Lee, C. Sun, and X. Zhang, "Sub-diffraction-limited optical imaging with a silver superlens," *Science*, vol.308, pp.534–537, 2005.

[42] D. Schurig and D R Smith, "Negative index lens aberrations," *Phys. Rev. E*, vol.70, p.065601, 2004.

[43] V. Kravets, F. Schedin, and A. Grigorenko, "Plasmonic blackbody: Almost complete absorption of light in nanostructured metallic coatings," *Phys. Rev. B.*, vol.78, p.205405, 2008.

[44] M. K. Hedayati, F. Faupel, and M. Elbahri, "Review of plasmonic nanocomposite metamaterial absorber," *Materials.*, vol.7, pp.1221–1248, 2014.

[45] Q. Chen, J. Bai, L. Chen, and Y. Fu, "A miniaturized absorptive frequency selective surface," *IEEE Antennas and Wireless Propagation Letters*, vol.14, pp.80–83, 2015.

[46] P. Munaga, *et al*., "A fractal ‐ based compact broadband polarization insensitive metamaterial absorber using lumped resistors," *Microwave and optical technology letters*, vol.58(2), pp.343–347, 2016.

[47] S. Ghosh, *et al.*, "Design, characterisation and fabrication of a broadband polarisation-insensitive multi-layer circuit analogue absorber," *IET Microw., Antennas Propag.*, vol.10, pp.850–855, 2016.

[48] Y. Liu, *et al*., "Ultra-thin broadband metamaterial absorber," *Appl. phys. A*, vol.108(1), pp.19–24, 2012.

[49] S. Ghosh, *et al.,* "Bandwidth-enhanced polarization-insensitive microwave metamaterial absorber and its equivalent circuit model," *J. Appl. Phys.*, vol.115(10), p.104503, 2014.

[50] D. Sood and C. C. Tripathi, "Broadband ultrathin low-profile metamaterial microwave absorber," *Appl.phys. A*, vol.122(4), pp.1–7, 2016.

[51] B. Y. Wang, *et al*., "A novel ultrathin and broadband microwave metamaterial absorber," *J. Appl. Phys.*, vol.116(9), p.94504, 2014.

[52] L. Li and Z. Y. Lv, "Ultra-wideband polarization-insensitive and wide-angle thin absorber based on resistive metasurfaces with three resonant modes," *J. Appl. Phys.*, vol.122, p.055104 (2017).

[53] T. Beeharry, *et al*., "A dual layer broadband radar absorber to minimize electromagnetic interference in radomes," *Scientific Reports*, vol.8, p.382 (2018).

[54] T. Liu and S. S. Kim, "Ultrawide bandwidth electromagnetic wave absorbers composed of double-layer frequency selective surfaces with different patterns," *Scientific Reports*, vol.8, p.13889 (2018).

[55] P. Xiao, X. C. Tu, C. T. Jiang, Z. J. Li, S. Y. Zhou, D. F. Pan, Q. Y. Zhao, X. Q. Jia, L. B. Zhang, L. Kang, J. Chen, and P. H. Wu, "Planar double-slot antenna integrated into a Nb5N6 microbolometer THz detector," Opt. Lett. **45**(10), 2894–2897 (2020).

[56] R. B. Kohlhaas, R. J. B. Dietz, S. Breuer, S. Nellen, L. Liebermeister, M. Schell, and B. Globisch, "Improving the dynamic range of InGaAs-based THz detectors by localized beryllium doping: up to 70 dB at 3 THz," Opt. Lett. **43**(21), 5423–5426 (2018).

[57] A. Jooshesh, L. Smith, M. Masnadi-Shirazi, V. Bahrami-Yekta, T. Tiedje, T. E. Darcie, and R. Gordon, "Nanoplasmonics enhanced terahertz sources," Opt. Express **22**(23), 27992 (2014).

[58] Q.Y. Lu, S. Slivken, N. Bandyopadhyay, Y. Bai, and M. Razeghi, "Widely tunable room temperature semiconductor terahertz source," Appl. Phys. Lett. **105**(20), 201102 (2014).

[59] M. Y. Glyavin, G. G. Denisov, V. E. Zapevalov, M. A. Koshelev, M. Y. Tretyakov, and A. I. Tsvetkov, "High power terahertz sources for spectroscopy and material diagnostics," Phys. Uspekhi **59**(6), 595–604 (2016).

[60] A. W. M. Lee, Q. Qin, S. Kumar, B. S. Williams, S. Benjamin, Q. Hu, and J. L. Reno, "Real-time terahertz imaging over a standoff distance (> 25 meters)," Appl. Phys. Lett. **89**(14), 141125 (2006).

[61] D. Zimdars and I. Duling, "Terahertz imaging revealing hidden defects," Nature Photonics, **3**(11), 630–632 (2009).

[62] D. M. Mittleman, "Twenty years of terahertz imaging [Invited]," Opt. Express **26**(8), 9417–9431 (2018).

[63] F. Alves, D. Grbovic, B. Kearney, N. V. Lavrik, and G. Karunasiri, "Bi-material terahertz sensors using metamaterial structures," Opt. Express **21**(11), 13256–13271 (2013).

[64] B. Saverio and D. N. Paolo, "Sensors: Mapping terahertz waves," Nature Photonics **9**(3), 147–148 (2015).

[65] Y. P. Zhang, T. T. Li, B. B. Zeng, H. Y. Zhang, H. H. Lv, X. Y. Huang, W. L. Zhang, and A. K. Azad, "A graphene based tunable terahertz sensor with double fano resonances," Nanoscale **7**(29), 12682–12688 (2015).

[66] C. Corsi and F. Sizov, THz and security applications: detectors, sources and associated electronics for THz applications. (Springer, 2014).

[67] A. Sokolnikov, THz identification for defense and security purposes: identifying material, substances, and items. (Singapore;:World Scientific, 2013).

[68] A. Maffucci and S. A. Maksimenko, Fundamental and applied nano-electromagnetics II: THz circuits, materials, devices. (Springer, 2019).

[69] R. Knipper, A. Brahm, E. Heinz, T. May, G. Notni, H. Meyer, A. Tunnermann, and J. Popp, "THz absorption in fabric and its impact on body scanning for security application," IEEE Trans. Terahertz Sci. Technol. **5**(6), 999–1004 (2015).

[70] M. Janneh, A. D. Marcellis, E. Palange, A. T. Tenggara, and D. Byun, "Metasurface-based THz dual-band absorber sensor for the measurement of refractive index variations of chemical and biological substances," Proceeding **1**(4), 558 (2017).

[71] J. Luo, Q. Lin, L. L. Wang, S. X. Xia, H. Y. Meng, and X. Zhai, "Ultrasensitive tunable terahertz sensor based on five-band perfect absorber with Dirac semimetal," Opt. Express **27**(15), 20165–20176 (2019).

[72] M. Nourbakhsh, E. Z. Jahromi, and R. Basiri, "Ultra-wideband terahertz metamaterial absorber based on Snowflake Koch Fractal dielectric loaded graphene," Opt. Express **27**(23), 32958–32969 (2019).

[73] Z. M. Liu, L. Guo, and Q. M. Zhang, "A simple and efficient method for designing broadband terahertz absorber based on singular graphene metasurface," Nanomaterials **9**, 1351 (2019).

[74] Y. N. Jiang, H. D. Zhang, J. Wang, C. N. Gao, J. Wang, and W. P. Cao, "Design and performance of a terahertz absorber based on patterned graphene," Opt. Lett. **43**(17), 4296–4299 (2018).

[75] Y. P. Qi, Y. Zhang, C. Q. Liu, T. Zhang, B. H. Zhang, L. Y. Wang, X. Y. Deng, X. X. Wang, and Y. Yu, "A tunable terahertz metamaterial absorber composed of hourglass-shaped graphene arrays," Nanomaterials **10**, 533 (2020).

[76] J. Huang, J. Li, Y. Yang, J. Li, J. H. Li, Y. T. Zhang, and J. Q. Yao, "Active controllable dual broadband terahertz absorber based on hybrid metamaterials with vanadium dioxide," Opt. Express **28**(5), 7018–7027 (2020).

[77] Y. X. Fang, and Z. R. Hu, "Ultra-wideband polarization-insensitive thin microwave absorber composed of triple-layer resistive surfaces," in *14th EuCAP, Copenhagen, Denmark*, 1–4 (2020).

[78] W. J. Chen, R. Chen, Y. Zhao, and Y. G. Ma, "Broadband metamaterial absorber with an in-band metasurface function," Opt. Lett. **44**(5), 1076–1079 (2019).

[79] A. B. Li, Y. B. Li, J. Long, E. Forati, Z. X. Du, and D. Sievenpiper, "Time-moduated nonreciprocal metasurface absorber for surface waves," Opt. Lett. **45**(5), 1212–1215 (2020).

[80] A. G. D' Aloia, M. D' Amore, and M. S. Sarto, "Low-terahertz transparent graphene-based absorber," Nanomaterials **10**, 843 (2020).

[81] P. H. Wu, C. F. Zhang, Y. J. Tang, B. Liu, and L. Lv, "A perfect absorber based on similar fabry-perot four-band in the visible range," Nanomaterials **10**, 488 (2020).

[82] H. Y. Ge, Y. Y. Jiang, Z. H. Xu, F. Y. Lian, Y. Zhang, and S. H. Xia, "Identification of wheat quality using THz spectrum," Opt. Express **22**(10), 12533–12544 (2014).

[83] Y. P. Yang, D. W. Zhai, Z. W. Zhang, and C. L. Zhang, "THz spectroscopic identification of red mineral pigments in ancient Chinese artworks," J. Infrared Milli. Terahz. Waves **38**(10), 1232–1240 (2017).

[84] M. Dutta, A. S. Bhalla, and R. Y. Guo, "THz imaging of skin burn: seeing the unseen–an overview," Advances in Wound Care **5**(8), 338–348 (2016).

[85] B. Mulla and C. Sabah, "Multiband metamaterial absorber design based on plasmonic resonances for solar energy harvesting," Plasmonics **11**(5), 1313–1321 (2016).

[86] A. Bordbar, R. Basiry, and A. Yahaghi, "Design and equivalent circuit model extraction of a broadband graphene metasurface absorber based on a hexagonal spider web structure in the terahertz band," Appl. Opt. **59**(7), 2165–2172 (2020).

[87] H. Y. Shen, F. X. Liu, C. Y. Liu, D. Zeng, B. H. Guo, Z. C. Wei, F. Q. Wang, C. H. Tan, X. G. Huang, and H. Y. Meng, "A polarization-insensitive and wide-angle terahertz absorber with ring-porous patterned graphene metasurface," Nanomaterials **10**, 1410 (2020).

[88] M. Kenney, J. Grant, and D. R. S. Cumming, "Alignment-insensitive bilayer THz metasurface absorbers exceeding 100% bandwidth," Opt. Express **27**(15) 20886–20900 (2019).

[89] H. Li, and J. Yu, "Bifunctional terahertz absorber with a tunable and switchable property between broadband and dual-band," Opt. Express **28**(17), 25225–25237 (2020).

[90] S. Zhu, Y. Y. Cao, Y. Y. Fu, X. C. Li, L. Gao, H. Y. Chen, and Y. D. Xu, "Switchable bifunctional metasurfaces: nearly perfect retroreflection and absorption at the terahertz regime," Opt. Lett. **45**(14), 3989–3992 (2020).

[91] J. Huang, J. N. Li, Y. Yang, J. Li, J. H. Li, Y. T. Zhang, and J. Q. Yao, "Broadband terahertz absorber with a flexible, reconfigurable performance based on hybrid-patterned vanadium dioxide metasurfaces," Opt. Express **28**(12), 17832–17840 (2020).

[92] C. Samanta, N. Arora, and A. K. Naik, "Tuning of geometric nonlinearity in ultrathin nanoelectromechanical systems," Appl. Phys. Lett. **113**(11), 113101 (2018).

[93] C. Zhang, J. Jing, Y. Wu, Y. Fan, W. Yang, S. Wang, Q. Song, and S. Xiao, "Stretchable all-dielectric metasurfaces with polarization-insensitive and full-spectrum response," ACS Nano **14**(2), 1418–1426 (2020).

[94] J. Q. He, M. Zhang, S. W. Shu, Y. Yan, and M. X. Wang, "VO_2 based dynamic tunable absorber and its application in switchable control and real-time color display in the visible region," Opt. Express **28**(25), 37590–37599 (2020).

[95] D. Shrekenhamer, W. C. Chen, and W. J. Padilla, "Liquid crystal tunable metamaterial absorber," Phys. Review Lett. **110**(17), 177403 (2013).

[96] F. Baranzadeh and N. Nozhat, "Tunable metasurface refractive index plasmonic nano-sensor utilizing an ITO thin layer in the near-infrared region," Appl. Optics **58**(10), 2616–2623 (2019).

[97] H. D. Jeong and S. Y. Lee, "Tunable Plasmonic Absorber Using a Nanoslit Array Patterned on a Ge2Sb2Te5 -Inserted Fabry-P ́erot Resonator," J. Lightwave Technol. **36**(24), 5857–5862 (2018).

[98] O. Abed and L. Yousefi, "Tunable metasurfaces using phase change materials and transparent graphene heaters," Opt. Express **28**(23), 33876–33889 (2020).

[99] A. N. Grigorenko, M. Polini, and K. S. Novoselov, "Graphene plasmonics," Nat. Photonics **6**(11), 749–758 (2012).

[100] Q. Bao, H. Hoh, and Y. Zhang, Graphene Photonics, Optoelectronics, and Plasmonics. (CRC Press, 2017).

[101] Y. T. Zhao, B. Wu, B. J. Huang, and Q. Chen, "Switchable broadband terahertz absorber/reflector enabled by hybrid graphene-gold metasurface," Opt. Express **25**(7), 7161–7169 (2017).

[102] X. Huang, W. He, F. Yang, J. Ran, B. Gao, and W. L. Zhang, "Polarization-independent and angle-insensitive broadband absorber with a target-patterned graphene layer in the terahertz regime," Opt. Express **26**(20), 25558–25566 (2018).

[103] H. Xiong, Q. Ji, T. Bashir, and F. Yang, "Dual-controlled broadband terahertz absorber based on graphene and Dirac semimetal," Opt. Express **28**(9), 13884–13894 (2020).

[104] K. D. Xu, J. X. Li, A. X. Zhang, and Q. Chen, "Tunable multi-band terahertz absorber using a single-layer square graphene ring structure with T-shaped graphene strips," *Optics Express*, vol.28, p.11482 (2020).

[105] E. Fitzer, K. H. Kochling, H. P. Boehm, and H. Marsh, "Recommended terminology for the description of carbon as a solid," *Pure Appl. Chem*., vol.67, pp.473–506 (1995).

[106] S. Eigler and A. Hirsch, "Chemistry with graphene and graphene oxide: challenges for synthetic chemists," *Angew. Chem. Int. Ed*., vol.53, pp.7720–7738 (2014).

[107] H. Petroski: The Pencil: A History of Design and Circumstance. (Alfred Knopf, New York, 1989).

[108] S. Nazarpour and S. R. Waite: *Graphene technology: from laboratory to fabrication*. (Weinheim Germany: Wiley-VCH, 2016).

[109] A. H. Castro Neto, F. Guinea, N. M. R. Peres, K. S. Novoselov, and A. K. Geim, "The electronic properties of graphene," *Rev. Mod. Phys.*, vol.81, pp.109–162 (2009).

[110] J. C. Charlier, X. Blasé, and S. Roche, "Electronic and transport properties of nanotubes," *Rev. Mod. Phys*., vol.79, p.677 (2007).

[111] W. Andreoni: The Physics of Fullerene-Based and Fullerene-Related Materials. (Springer, 2000).

[112] P. Phillips, "Mottness," *Annals of Physics*, vol.321, pp.1634–1650 (2006).

[113] S. Y. Jun: Electronic transport of graphene devices. (2012).

[114] C. G. Lee, X. D. Wei, J. W. Kysar, and J. Hone, "Measurement of the elastic properties and intrinsic strength of monolayer graphene," *Science*, vol.321, pp.385–388 (2008).

[115] K. Cao, *et al*., "Elastic straining of free-standing monolayer graphene," *Nature Communications*, vol.11, p.284 (2020).

[116] 2010 Nobel Physics Laureates.

[117] A. A. Balandin, *et al*., "Superior thermal conductivity of single-layer graphene," *Nano Letters*, vol.8, pp.903–907 (2008).

[118] W. W. Cai, *et al*., "Thermal transport in suspended and supported monolayer graphene grown by chemical vapor deposition," *Nano Letters*, vol.10, pp.1645–1651 (2010).

[119] C. Faugeras, B. Faugeras, M. Orlita, M. Potemski, R. R. Nair, and A. K. Geim, "Thermal conductivity of graphene in corbino membrane geometry," *ACS Nano*, vol.4, pp.1889–1892 (2010).

[120] J. U. Lee, D. Yoon, H. Kim, S. W. Lee, and H. Cheong, "Thermal conductivity of suspended pristine graphene measured by Raman spectroscopy," *Phys. Rev. B.*, vol.83, p.081419 (2011).

[121] X. F. Xu, *et al*., "Length-dependent thermal conductivity in suspended single-layer graphene," *Nature Communications*, vol.5, p.3689 (2014).

[122] Y. S. Touloukian: *Thermophysical Properties of Matter*. (Springer US, 1995).

[123] P. Delhaes: *Graphite and Precursors*. (CRC Press, 2000).

[124] S. Biabanifard, M. Biabanifard, S. Asgari, S. Asadi, M. C. E. Yagoub, "Tunable ultra-wideband terahertz absorber based on graphene disks and ribbons," Opt. Commun. **427**, 418–425 (2018).

[125] X. Huang, Z. Hu, and P. Liu, "Graphene based tunable fractal Hilbert curve array broadband radar absorbing screen for radar cross section reduction," *AIP Advances*, vol.4, p.117103 (2014).

[126] Y. Zhang, L. Gomez, F. N. Ishikawa, A. Madaria, K. Ryu, C. Wang, A. Badmaev, and C. Zhou, "Comparison of graphene growth on single-crystalline and polycrystalline Ni by chemical vapor deposition," *J. Phys. Chem. Lett*., vol.1 (20), pp.3101–3107 (2010).

[127] Q. Yu, J. Lian, S. Siriponglert, H. Li, Y. P. Chen, and S. S. Pei, "Graphene segregated on Ni surfaces and transferred to insulators," *Appl. Phys. Lett*., vol.93 (11), p.113103 (2008).

[128] R. Blume, *et al*., "The influence of intercalated oxygen on the properties of graphene on polycrystalline Cu under various environmental conditions," *Phys. Chem. Chem. Phys*., vol.16, pp.25989–26003 (2014).

[129] J. H. Lee, *et al*., "Wafer-scale growth of singlecrystal monolayer graphene on reusable hydrogen-terminated germanium," *Science*, vol.344(6181), pp.286–289 (2014).

[130] C. Mattevi, H. Kima, and M. Chhowalla, "A review of chemical vapour deposition of graphene on copper" *J. Mater. Chem*., vol.21 (10), pp.3324–3334 (2011).

[131] Y. Zhang, L. Zhang, and C. Zhou, "Review of chemical vapor deposition of graphene and related applications," *Acc. Chem. Res.*, vol.46 (10), pp.2329–2339 (2013).

[132] M. Yi and Z. Shen, "A review on mechanical exfoliation for the scalable production of graphene," *J. Mater. Chem. A,* vol.3(22), pp.11700–11715 (2015).

[133] A. Ciesielski and P. Samori, "Graphene via sonication assisted liquidphase exfoliation," *Chem. Soc. Rev.*, vol.43(1), pp.381–398 (2014).

[134] A. A. Green and M. C. Hersam, "Solution phase production of graphene with controlled thickness via density differentiation," *Nano Lett.*, vol.9(12), pp.4031–4036 (2009).

[135] A. A. Green and M. C. Hersam, "Emerging methods for producing monodisperse graphene dispersions," *J. Phys. Chem. Lett.*, vol.1(2), pp.544–549 (2010).

[136] U. Khan, H. Porwal, A. O'Neill, K. Nawaz, P. May, and J. N. Coleman, "Solvent-exfoliated graphene at extremely high concentration," *Langmuir*, vol.27(15), pp.9077–9082 (2011).

[137] K. R. Paton, *et al*., "Scalable production of large quantities of defect-free few-layer graphene by shear exfoliation in liquids," *Nat. Mater*., vol.13(6), pp.624–630 (2014).

[138] T. J. Nacken, C. Damm, H. Xing, A. Rüger, and W. Peukert, "Determination of quantitative structure–property and structure–process relationships for graphene production in water," *Nano Res*., vol.5(71), p.57328 (2015).

[139] C. Damm, T.J. Nacken, and W. Peukert, "Quantitative evaluation of delamination of graphite by wet media milling," *Carbon*, vol.81(1), pp.284–294 (2015).

[140] J. M. Englert, K. C. Knirsch, C. Dotzer, B. Butz, F. Hauke, E. Spiecker, and A. Hirsch, "Functionalization of graphene by electrophilic alkylation of reduced graphite," *Chem. Commun*., vol.48(41), pp.5025–5027 (2012).

[141] P. Vecera, K. Edelthalhammer, F. Hauke, and A. Hirsch, "Reductive arylation of graphene: insights into a reversible carbon allotrope functionalization reaction," *Phys. Status Solidi B*, vol.251(12), pp.2536–2540 (2014).

[142] http://www.graphene.ac.rs/lpe.html

[143] Tomašević-Ilić, *et al.*, "Transparent and conductive films from liquid phase exfoliated graphene," *Opt Quant Electron*, vol.48, p.319 (2016).

[144] M. M. Lucchese, *et al*., "Quantifying ion-induced defects and Raman relaxation length in graphene," *Carbon*, vol.48(5), pp.1592–1597 (2010).

[145] L. G. Can̦ado, *et al*., "Quantifying defects in graphene via Raman spectroscopy at different excitation energies," *Nano Lett*., vol.11(8), pp.3190–3196 (2011).

[146] E. I. Alarcon, M. Griffith, and K. I. Udekwu: Silver nanoparticle applications : in the fabrication and design of medical and biosensing devices. (Cham: Springer, 2015).

[147] G. Cepriá, *et al.*, "Selectivity of silver nanoparticle sensors: Discrimination between silver nanoparticles and Ag," *Sensors and actuators. B, Chemical*, vol.230, pp.25–30 (2016).

[148] B. Haddou, N. V. Rees, and R. G. Compton, "Nanoparticle-electrode impacts: the oxidation of copper nanoparticles has slow kinetics," *Physical chemistry chemical physics : PCCP*, vol.14(39), pp.13612–13617 (2012).

[149] H. J. Hwang, W. H. Chung, and H. S. Kim, "In situ monitoring of flash-light sintering of copper nanoparticle ink for printed electronics," *Nanotechnology*, vol.23(48), pp.485205–485205 (2012).

[150] Q. Shao, *et al*., "High‐performance and tailorable pressure sensor based on ultrathin conductive polymer film." *Small*, vol.10(8), pp.1466–1472 (2014).

[151] T. Wang, *et al.*, "A self‐Healable, highly stretchable, and solution processable conductive polymer composite for ultrasensitive strain and pressure sensing," *Advanced functional materials*, vol.28(7), p.1705551 (2018).

[152] L. Hu, D.S. Hecht, and G. Gruner, "Carbon nanotubes thin films: fabrication, properties, and applications." *Chemical reviews*, vol.110(10), pp.5790-5844 (2010).

[153] A. Kamvshnv and S. Magdassi, "Conductive nanomaterials for printed electronics," *Small*, vol.10(17), pp.3515-3535 (2014).

[154] Huang. X. Huang, K. Pan, and Z. Hu, "Experimental demonstration of printed graphene nano-flakes enabled flexible and conformable wideband radar absorbers," *Scientific Reports*, vol.1038, p.38197 (2016).

[155] T. Carey, *et al*., "Spray-coating thin films on three-dimensional surfaces for a semitransparent capacitive-touch device." *ACS applied materials & interfaces*, vol.10(23), pp.19948–19956 (2018).

[156] D. K. Mahalingam, *et al.*, "Spray-coated graphene oxide hollow fibers for nanofiltration." *Journal of membrane science*, vol.606, p.118006 (2020).

[157] M. Karakoti, *et al.*, "Spray dryer processed graphene oxide/reduced graphene oxide for high performance supercapacitor." *International journal of applied ceramic technology*, 17(4), pp.1899–1908 (2020).

[158] Pan. K. Pan, *et al.*, "Sustainable production of highly conductive multilayer graphene ink for wireless connectivity and IoT applications," *Nature communications*, vol.9, pp.5197–5197 (2018).

[159] T. Vuorinen, *et al.*, "Inkjet-printed graphene/PEDOT:PSS temperature sensors on a skin-conformable polyurethane substrate." *Scientific reports*, vol.6(1), pp.35289–35289 (2016).

[160] 15. T. Carey, *et al.*, "Fully inkjet-printed two-dimensional material field-effect heterojunctions for wearable and textile electronics." *Nature communications*, vol.8(1), pp.1202–1202 (2017).

[161] W. Lin, *et al.*, "Enhanced performance of lithium sulfur battery with a reduced graphene oxide coating separator." *Journal of the Electrochemical Society*, 162(8), pp.A1624–A1629 (2015).

[162] J. Nulman: Film sheet resistance measurement. *U.S. Patent.* Harvard, 5,698,989. (1997).

[163] F. M. Smits, "Measurement of sheet resistivities with the four-point probe," in The Bell System Technical Journal, vol. 37, no. 3, pp. 711-718, May 1958.

[164] D.M. Pozar: Microwave engineering. *John Wiley & Sons.* Harvard. 4th ed. (2011).

[165] D.B. Leeson: Impedance matching. *Microwave Enginneering.* 246 (1999).

[166] X. Huang, X. Zhang, Z. Hu, M. Aqeeli, and A. Alburaikan: Design of broadband and tunable terahertz absorbers based on graphene metasurface: equivalent circuit model approach. *IET Microwaves, Antennas & Propagation.* vol.9(4), pp.307–312 (2015).

[167] B.Z. Xu, C.Q. Gu, Z. Li, and Z.Y. Niu: A novel structure for tunable terahertz absorber based on graphene. *Optics Express.* vol.21(20), pp.23803–23811 (2013).

[168] A. Naeemi, and J.D. Meindl: Compact physics-based circuit models for graphene nanoribbon interconnects. *IEEE Trans. Electron Devices.* 56(9), pp.1822–1833 (2009).

[169] M. Tamagnone, J. Perruisseau-Carrier: Predicting input impedance and efficiency of graphene reconfigurable dipoles using a simple circuit model. *IEEE Antennas Wirel. Propag. Letters.* 13, pp.313–316 (2014).

[170] R.L. Fante, and M.T. Mccormack: Reflection properties of Salisbury screen. *IEEE Transaction on Antennas and Propagation.* vol.36(10), pp.1443–1454 (1988).

[171] R. Panwar, and J.R. Lee: Progress in frequency selective surface-based smart electromagnetic structures: A critical review. *Aerospace Science and Technology.* vol.66, pp.216–234 (2017).

[172] L. Sun, H. Cheng, Y. Zhou, and J. Wang: Broadband metamaterial absorber based on coupling resistive frequency selective surface. *Optics Express.* vol.20(4), p.4675 (2012).

[173] H.T. Chen, "Interference theory of metamaterial perfect absorbers," *Optics Express*. vol.**20**(7), p.7165 (2012).

[174] M. Born and E. Wolf: *Principles of optics* (Pergamon, 1980). 6th ed.

[175] E. Magill and H. A. Wheeler, "Wide-angle impedance matching of a planar array antenna by a dielectric," *IEEE Trans. Antennas Propag*., vol.14, pp.49–53, (1966).

[176] M. Gustafsson, "Use of dielectric sheets to increase the bandwidth of aplanar self-complementary antenna array," in Proceeding of the 2006 IEEE Antennas and Propagation Society International Symposium, Albuquerque, NM, USA, pp.2413–2416, 2006.

[177] X. Begaud, A. C. Lepage, S. Varault, M. Soiron, and A. Barka, " Ultra-wideband and wide-angle microwave metamaterial absorber," *Materials*, vol.11, p.2045, (2018).

[178] R. E. Collin: *Field Theory of Guided Waves.* New York: McGrawHill, 1960.

[179] Nicola Bowler: *Eddy-Current Nondestructive Evaluation*. Springer, New York, NY. 2019.

[180] D. Sievenpiper, L. J. Zhang, and R. F. J. Broas, "High-impedance electromagnetic surfaces with a forbidden frequency band," *IEEE Tran. Microw. Theory Tech.*, vol. 47, no. 11, pp. 2059–2074, Nov. 1999.

[181] M. Paquay, *et al.*, "Thin AMC structure for radar cross section reduction," *IEEE Trans. Antennas Propag*., vol. 55, pp. 3630–3638, Dec. 2007.

[182] Y. Zhang, R. Mittra, B. Wang, and N. Huang, "AMCs for ultra-thin and broadband RAM design," *Electronics Letters*, vol. 45, May 2009.

[183] Y. Fu, Y. Li, and N. Yuan, "Wideband composite AMC surfaces for RCS reduction," *Microwave Opt. Technol. Lett.*, vol. 53, pp. 712–715, 2011.

[184] J.C. Iriarte, J.L. Martinez, I. Maestrojuan, I. Liberal, A. Rebollo, I.Ederra, and R. Gonzalo, "Broadband RCS reduction using AMC technology," *EuCAP*, Rome, Italy, 2011, pp.1322–1323.

[185] J. C. I. Galarregui, *et al*., "Broadband radar cross-section reduction using AMC technology," *IEEE Trans. Antennas Propag*., vol. 61, pp. 6136–6143, 2013.

[186] X. Liu, J. Gao, L. Xu, X. Cao, Y. Zhao, and S. Li, "A coding diffuse metasurface for RCS reduction," *IEEE Antennas Wireless Propag. Lett.*, vol. 16, pp. 724–727, 2017.

[187] Y. Tsai, and R. Hwang, "RCS reduction of a composite AMC structure," *IEEE International Workshop on Electromagnetics*, Taipei, Taiwan, 2011, pp. 210–213.

[188] Y. Zhao, *et al*., "Broadband radar absorbing material based on orthogonal arrangement of CSRR etched artificial magnetic conductor," *Microw. Opt. Technol. Lett*., vol. 56, pp. 158–161, 2014.

[189] A.Y.Modi, C.A.Balanis, C.R.Birtcher, and H.N.Shaman, "Novel design of ultrabroadband radar cross section reduction surfaces using artificial magnetic conductors," *IEEE Trans. Antennas Propag*., vol. 65, pp. 5406–5417, 2017.

[190] H. Zhang, Y. Lu, J. Su, Z. Li, J. Liu, and Y. Yang, "Coding diffusion metasurface for ultra-wideband RCS reduction," *Electronics Letters*, vol. 53, pp. 187–189, Feb. 2017.

[191] W. Chen, C. A. Balanis, and C. R. Birtcher, "Checkerboard EBG surfaces for wideband radar cross section reduction," *IEEE Trans. Antennas Propag*., vol. 63, pp. 2636–2645, June 2015.

[192] C. A. Balanis, *Antenna Theory: Analysis and Design*, 3rd ed. Hoboken, NJ, USA: wiley, 2005.

[193] CST Studio Suite – Electromagnetic Field Simulation Software (https://www.3ds.com/products-services/simulia/products/cst-studio-suite/).

[194] https://www.mathworks.com/products/matlab.html

[195] Controlling CST MWS with MATLAB (https://habr.com/ru/post/325012/).

[196] The Component Object Model: Technical Overview. *Dr Dobbs Journal* (1994).

[197] V. G. Potemkin, Vychisleniya v srede MATLAB (Russian). 2004.

[198] Application Note – Calling CST Studio from MATLAB.

[199] O. Kramer, *Genetic Algorithm Essentials.* (Springer, 2017).

[200] C. Darwin, *On the Origin of Species*. John Murray, London, 1859.

[201] G. Syswerda, "Simulated crossover in genetic algorithms," *Foundations of Genetic Algorithms*, pp.239–255, 1992.

[202] A. Bhati, K. R. Hiremath, and V. Dixit, "Bandwidth enhancement of triple layer microwave absorber using metallic square patch," *Appl. Phys. A Mater. Sci. Process*., vol. 124, pp.798, 2018.

[203] Y. J. Kim, Y. J. Yoo, J. S. Hwang, and Y. P. Lee, "Ultra-broadband microwave metamaterial absorber based on resistive sheets," *J. Opt*., vol. 19, pp. 015103, 2017.

[204] X. Bagaud, A. C. Lepage, S. Varault, M. Soiron, and A. Barka, "Ultra-wideband and wide-angle microwave metamaterial absorber," *Materials*, vol. 11, pp. 2045, 2018.

[205] J. Sun, L. Liu, G. Dong, and J. Zhou, "An extremely broad band metamaterial absorber based on destructive interference," *Opt. Express*, vol. 19, pp. 21155-21162, Oct. 2011.

[206] S. Ghosh, S. Bhattacharyya, and K. V. Srivastava, "Design, characterisation and fabrication of a broadband polarisation-insensitive multi-layer circuit analogue absorber," *IET Microw. Antennas Propag.*, vol. 10, pp. 850-855, 2016.

[207] Y. Fang, and Z. Hu, "Broadband and Wide-angle Microwave Metamaterial Absorber with Effective EM Wave Absorption in the S-, C-, X- and Ku-band," *Accepted by European Conference on Antennas and Propagation*, Düsseldorf, Germany, 2021.

[208] T. Leng, *et al*., "Printed graphene/WS_2 battery-free wireless photosensor on papers," *2D Materials*, vol. **7**, 024004, Jan. 2020.

[209] T. Leng, et al., "Screen-printed graphite nanoplate conductive ink for machine learning enabled wireless radiofrequency-identification sensors," *ACS applied nano materials*, vol. 2, pp. 6197–6208, Oct. 2019.

[210] Y. Fang, Y. Jiang, K. Pan and Z. Hu, "On the design of metamaterial radar absorber applying AMC by controlling surface resistance," *IEEE International Symposium on Antennas and Propagation and USNC-URSI Radio Science Meeting*, Atlanta, GA, USA, 2019, pp. 1327-1328.

[211] A. K. Bhattacharyya: *Phased Array Antennas: Floquet Analysis, Synthesis, BFNs, and Active Array Systems*, Hoboken, NJ, USA: Wiley, 2006.

[212] https://www.polymax.co.uk/media/documents/Datasheet/general-purpose-silicone-rubber-sheeting.pdf

[213] V. P. Gusynin, S. G. Sharapov, and J. P. Carbotte, "Magneto-optical conductivity in graphene," J. Phys.: *Condens. Matter*, vol.**19**, 026222 (2007).

[214] G. W. Hanson, "Dyadic Green's functions and guided surface waves for a surface conductivity model of graphene," *J. Appl. Phys*., vol.103(6), 064302 (2008).

[215] Y. P. Qi, C. Q. Liu, B. B. Hu, X. Y. Deng, and X. X. Wang, "Tunable plasmonic absorber in THz-band range based on graphene 'arrow' shaped metamaterial," *Results in Physics*, vol.15, 102777 (2019).

Appendix: MATLAB code

```
clc;
clear;

cst = actxserver('CSTStudio.Application');
mws = cst.invoke('NewMWS');
mws.invoke('OpenFile','C:\Users\My Documents\GeneA.cst');
solver = mws.invoke('FDSolver');
export = mws.invoke('ASCIIExport');
plot1d = mws.invoke('Plot1D');

filename = strcat('\\...\home$\GA\GeneAresult.txt');

dna_size = 16;
pop_size = 30;
cross_rate = 0.2;
mutate_rate = 0.02;
n_generation = 20;
seed_size = 3;

pop = randi(2,pop_size,dna_size)-1;

for i = 1 : n_generation

   for j = 1 : pop_size
      dna = zeros(dna_size);
      for d = 1 : dna_size
         if pop(j,d) == 0
            dna(d) = 8.7;
         else
            dna(d) = 98;
         end
      end

      mws.invoke('StoreDoubleParameter','rs1',dna(1));
      mws.invoke('StoreDoubleParameter','rs2',dna(2));
      mws.invoke('StoreDoubleParameter','rs3',dna(3));
      mws.invoke('StoreDoubleParameter','rs4',dna(4));
      mws.invoke('StoreDoubleParameter','rs5',dna(5));
      mws.invoke('StoreDoubleParameter','rs6',dna(6));
      mws.invoke('StoreDoubleParameter','rs7',dna(7));
      mws.invoke('StoreDoubleParameter','rs8',dna(8));
      mws.invoke('StoreDoubleParameter','rs9',dna(9));
      mws.invoke('StoreDoubleParameter','rs10',dna(10));
      mws.invoke('StoreDoubleParameter','rs11',dna(11));
      mws.invoke('StoreDoubleParameter','rs12',dna(12));
      mws.invoke('StoreDoubleParameter','rs13',dna(13));
      mws.invoke('StoreDoubleParameter','rs14',dna(14));
      mws.invoke('StoreDoubleParameter','rs15',dna(15));
      mws.invoke('StoreDoubleParameter','rs16',dna(16));

      mws.invoke('Rebuild');
      solver.invoke('Start');
```

```
    mws.invoke('SelectTreeItem','Tables\1D Results\absorption');
    plot1d.invoke('PlotView','magnitude');
    export.invoke('FileName',filename);
    export.invoke('Mode','FixedNumber');
    export.invoke('Step','1001');
    export.invoke('Execute')

    result = h_remove(filename);
    result = importdata(filename);

    flag = 0;
    f_min = 0;
    f_max = 0;

    for k = 1:1001
        if flag == 0
            if result(k,2)>0.9
                flag = 1;
                f_min = result(k,1);
            end
        else
            if result(k,2)<0.9
                flag = 0;
                f_max = result(k,1);
            end
        end
        if f_max - f_min > 0
            break
        end
    end

bandwidth(i,j) = f_max - f_min;

end

[maxvalue,location] = max(bandwidth(i,:));
best_fit_each_G(i,1:dna_size) = pop(location,1:dna_size);
best_fit_each_G(i,dna_size+1) = maxvalue;

for b = 1:seed_size
    pop_mom(b,:) = pop(location,:);
end

fitness = bandwidth(i,:)/10;

idx = randsample(pop_size,pop_size,true,fitness);
for j = seed_size+1 : pop_size
    pop_mom(j,:)=pop(idx(j),:);
end

pop = pop_mom;
pop_dad = pop;
for k = 1:pop_size
    if rand < cross_rate
        n = randi(pop_size);
        cross_points = randi(2,1,dna_size)-1;
        for m =1:dna_size
```

```
            if cross_points(m)
                child(m) = pop(k,m);
            else
                child(m) = pop_dad(n,m);
            end
        end

        for t = 1:dna_size
            if rand < mutate_rate
                if child(t) == 0
                    child(t) = 1;
                else
                    child(t) = 0;
                end
            end
        end
        pop(k,:) = child;
    end
  end
  disp(i)
end

disp(bandwidth)

mws.invoke('save');
```